

Nonlocal and local objects: Andreev bound states, and quantum dots as spectroscopic tools

THIS THESIS HAS BEEN SUBMITTED

BY

ALISA DANILENKO

TO

THE FACULTY OF SCIENCE,
UNIVERSITY OF COPENHAGEN

IN PARTIAL FULFILLMENT OF THE REQUIREMENTS

FOR THE DEGREE OF

DOCTOR OF PHILOSOPHY

IN THE SUBJECT OF

PHYSICS

COPENHAGEN, DENMARK

OCTOBER 2022

Nonlocal and local objects: Andreev bound states, and quantum dots as spectroscopic tools

ABSTRACT

Bringing together superconductor and semiconductor materials allows for the combination of spin-orbit coupling and a high electron g -factor with an induced superconducting pairing, forming a hybrid material. In this thesis, we make use of such hybrids of semiconducting InAs and superconducting Al combined in a two-dimensional heterostructure grown by molecular beam epitaxy. This two-dimensional platform allows us to design an evolving series of advanced devices which enable the detailed study of bound states that emerge when these materials are confined at low temperature, and in the presence of a Zeeman field.

Throughout the thesis, multiple side probes along the length of confined nanowires (NWs) allow for tunneling spectroscopy, enabling the local investigation of the density of states (DOS) at the probe locations. These multiple probes are used to study extended Andreev bound states (ABSs) forming inside the NWs, which appear as subgap resonances which are non-trivially correlated with respect to gate voltage and magnetic field.

Nonlocal conductance was used to determine the charge character of the extended ABSs. The modification of their charge character as a function of electrostatic gate was found to be in agreement with theoretical predictions for the total Bardeen-Cooper-Schrieffer (BCS) charge of the ABS.

Quantum dots (QDs) were utilized as probes of the ABS properties, starting from a regime in which there was strong hybridization between a QD in a tunnel barrier and an ABS confined in the NW. The effect of hybridization was observed both locally, at the location of the QD, and non-locally at a neighboring tunnel probe. This provided a robust method for confirming ABS extension.

Laterally defined QD with tunable couplings to both a normal lead and the NW were implemented; multiple designs for such QDs were explored. In a regime of weak coupling to both normal lead and NW, QD levels could be used as spectrometers of the NW DOS. In an applied magnetic field, the QD energy levels became Zeeman split, allowing for spectroscopy of the NW with both spin and charge resolution.

RESUMÉ

Sammenføringen af superledende og halvledende materialer muliggør kombinationen af spinbane kobling og en høj g -faktor med en induceret superledende parring og fremstiller dermed et hybrid materiale. I denne afhandling laver vi denne slags hybrider af halvledende InAs og superledende Al kombineret i en todimensionel heterostruktur, groet af molekylær stråle epitaxy. Denne todimensionelle platform faciliterer designs af en voksende række komplicerede kredsløb, som muliggøre detaljerede studier af bundne tilstande, der opstår når disse materialer er rumligt begrænsede ved lave temperaturer, samt påvirket af et Zeeman felt.

I denne afhandling anvendes mange sideprober langs en rumligt begrænset nano-ledninger (NL) til tunnel spektroskopi, hvilket muliggør en lokal undersøgelse af tilstandstætheden (TT) ved probelokationerne. De mange prober bruges til at studere aflange bundne Andreev tilstande (BAT), som former inde i (NL) og kommer til udtryk som undergab-ræsonancer, der på ikke-trivel vis er forbundet med port-spændinger og magnetiske felter.

Ikke-lokal ledningsevne blev anvendt til bestemmelse af ladningskarakteren af de aflange BAT. Ændringer af deres ladningskarakter, som funktion af elektrostatiske porte, matchede teoretiske forudsigelser af den totale Bardeen-Cooper-Schrieffer (BCS) ladning af BAT.

Kvanteprikker (KP) blev anvendt som prober af BAT egenskaber, først i et regime med stærk hybridisering mellem en KP i en tunnel barriere og BAT i NL. Effekten af denne hybridisering blev observeret både lokalt, ved KP'en, samt ikke-lokalt ved nabo-tunnelproben. Dette gav en robust metode for bekræftelse af udstrukte BAT.

Lateralt definerede KP'er med justerbare forbindelser, både til en resistive forbindelse og til NL, blev implementeret; mange designs for sådanne KP blev udforsket. I et regime med svag kobling både til den resistive forbindelse samt NL, kunne KP niveauer bruges som spektrometer af NL TT. Under et påtrykt magnetfelt, blev KP energiniveauerne splittet, hvilket muliggjorde spektroskopi af NL med både ladning- og spin-opløsning.

LIST OF PUBLICATIONS

This thesis includes results that are adapted from the following publications and manuscripts:

- **Nonlocal conductance spectroscopy of Andreev bound states in gate-defined InAs/Al nanowires**
A. Pöschl, *A. Danilenko*, D. Sabonis, K. Kristjuhan, T. Lindemann, C. Thomas, M.J. Manfra, C.M. Marcus.
In review. arXiv:2204.02430
- **Nonlocal signatures of hybridization between quantum dot and Andreev bound states**
A. Pöschl, *A. Danilenko*, D. Sabonis, K. Kristjuhan, T. Lindemann, C. Thomas, M.J. Manfra, C.M. Marcus.
Phys. Rev. B **106**, L161301
- **Spin-resolved spectroscopy using a quantum dot defined in InAs 2DEG**
A. Danilenko, A. Pöschl, D. Sabonis, V. Vlachodimitropoulos, C. Thomas, M.J. Manfra, C.M. Marcus.
In preparation.

Manuscripts that are not discussed in this thesis, but included for completeness:

- **Few-mode to mesoscopic junctions in gatemon qubits**
A. Danilenko, D. Sabonis, G. W. Winkler, O. Erlandsson, P. Krogstrup, C. M. Marcus.
In review. arXiv:2209.03688

Contents

I	MOTIVATION AND INTRODUCTION	I
1.1	The 2D electron gas	3
1.2	Superconductivity and proximity effect	4
1.2.1	A brief BCS reminder	4
1.2.2	Andreev reflection	9
1.2.3	Proximity effect	10
1.3	Bound states in proximitized systems	10
1.3.1	Majorana bound states	12
1.4	Quantum dots	17
1.4.1	Coulomb blockade	18
1.4.2	Coupling quantum dots to superconductors	21
2	MATERIALS AND METHODS	24
2.1	Proximitized two-dimensional electron gas	25
2.2	Device fabrication	28
2.2.1	From wafer to chip	28
2.2.2	Electron beam lithography	28
2.2.3	Wet etching	31
2.2.4	Dielectric deposition	34
2.2.5	Metal gate deposition	34
2.2.6	Final imaging	36
2.3	Low temperature measurement	38
2.3.1	Mounting and wire bonding	38
2.3.2	Tunneling spectroscopy	39
2.3.3	Nonlocal conductance	42
2.3.4	Tunnel barrier design	44
3	EXTENDED STATES IN 2DEG STRUCTURES: LOCAL MEASUREMENT	47
3.1	Local spectroscopy	49

3.2	Electrostatically defined bound states	51
3.3	Illusions of extension	56
4	NONLOCAL CONDUCTANCE SPECTROSCOPY OF ANDREEV BOUND STATES	60
4.1	Introduction	61
4.2	Nonlocal conductance measurement	62
4.3	Magnetic field rotations	65
4.4	Nonlocal analysis and BCS charge extraction	69
4.5	Conclusion	78
5	HYBRIDIZATION BETWEEN ANDREEV BOUND STATES AND QUANTUM DOTS	79
5.1	Introduction	80
5.2	Extended states and dot formation	81
5.3	Signatures of hybridization, local and nonlocal	86
5.4	Conclusion	88
6	FORMATION AND CONTROL OF QUANTUM DOTS IN INAs 2DEGs	90
6.1	Device design	91
6.2	Turning on the probes	95
6.3	Forming a dot	96
6.4	Tuning the coupling	102
6.5	Biasing configurations	106
6.6	Conclusions	108
7	SPIN-RESOLVED SPECTROSCOPY USING A QUANTUM DOT DEFINED IN INAs 2DEG	109
7.1	Introduction	110
7.2	Device design	112
7.3	Spectroscopy at low magnetic field	115
7.4	Spin-resolved spectroscopy	122
7.5	Spin and charge polarization of tunneling current	133
7.6	Discussion	139
8	ABS AND FREQUENCY CONTROL IN GATEMON QUBITS	143
8.1	Experimental setup	154
8.2	Simulation parameters	154
8.3	Additional simulations	155
8.4	Additional data	157

9	CONCLUSION AND OUTLOOK	162
	APPENDIX A FABRICATION PROTOCOLS	165
	A.1 Side-probe devices with superconducting leads	165
	A.2 Side-probe devices with semiconducting leads	172
	REFERENCES	193

Listing of figures

1.1	Spin-orbit coupling, schematically illustrated	3
1.2	BCS theory - the formation of Cooper pairs and quasiparticle excitations in a superconductor	5
1.3	Andreev reflection at superconducting - normal metal interface	8
1.4	Illustration of quantum dot formation by lateral electrostatic gating, Coulomb resonance lineshapes, and Coulomb blockade measurements	18
1.5	Schematic singlet-doublet ground state phase diagram of a quantum dot coupled to a superconductor, with schematic transport examples at different coupling strengths	21
2.1	2DEG material stack and transmission electron microscopy images	25
2.2	Illustration of electron beam lithography procedure for alignment mark creation	30
2.3	Illustration of fabrication steps for a typical superconductor-semiconductor hybrid 2DEG chip	32
2.4	Optical micrograph of a typical chip after the last fabrication step	35
2.5	Chip with two wire bonded devices	37
2.6	Schematic of electrical measurement setup for local differential conductance measurements	40
2.7	Schematic of electrical measurement setup for nonlocal differential conductance measurements	43
2.8	Three main ways of forming tunnel barriers utilized in this project	45
3.1	Micrograph of a device based on proximitized 2DEG, used for local and nonlocal spectroscopy measurements	48
3.2	Local differential conductance measurements in device 1 as a function of gate and parallel magnetic field	50
3.3	Zero voltage bias mapping of states probed at two ends of a proximitized NW segment, without clear correlations	52

3.4	Zero voltage bias mapping of extended states probed at two ends of a proximitized NW segment	53
3.5	Extended bound state double ended local conductance measurement	54
3.6	Phase diagram style measurement of the states underneath a proximitized NW segment, as a function of plunger gate voltage and parallel magnetic field	56
3.7	Differential conductance measurements on two sides of a NW segment showing resonances which appear correlated, but are in fact related to different states	57
3.8	Differential conductance maps, taken with respect to gates which tune only one of two tunnel barriers used for the measurement	59
4.1	Measurement of the two local (a, d) and two nonlocal (b, c) conductances as a function of V_{SD} and magnetic field $B_{ }$	64
4.2	Local and nonlocal conductance of ABSs as function of rotating magnetic field around the NW, radius 0.1 T	66
4.3	Local and nonlocal conductance of ABSs as function of rotating magnetic field around the NW, radius 0.2 T	67
4.4	Local and nonlocal conductance of ABSs as function of rotating magnetic field around the NW, radius 0.4 T	68
4.5	False-color scanning electron micrograph of device 3	70
4.6	Measurement of the four conductances as a function of V_{SD} and magnetic field	71
4.7	Local and nonlocal conductance as a function of NW segment plunger gate at three values of parallel magnetic field $B_{ }$	73
4.8	Extracting the	77
5.1	Scanning electron micrograph of device 3, with spectroscopy in depleted regime	82
5.2	Micrograph of wire segment of device 3, with gate maps showing NW and QD states	84
5.3	Correlated evolution of ABSs in magnetic field, measured from both ends	85
5.4	Tunneling spectroscopy showing nonlocal signatures of hybridization between a quantum dot and bound states	87
6.1	Micrograph of a device based on proximitized 2DEG, with helper gates for QD formation (device 1)	92
6.2	Micrograph of a device based on proximitized 2DEG, without helper gates (device 2)	93
6.3	QPC measurement at zero field, with QDs turned off)	94

6.4	One dimensional sweeps showing the confinement of a QD in device 2	97
6.5	Confinement of QD with C and D gates in device 2, showing regular Coulomb features	98
6.6	Coulomb blockade as a function of bias for finite and zero perpendicular magnetic field (device 2)	100
6.7	Confinement of QD with C and D gates in device 1, showing even-odd behavior	101
6.8	Coulomb blockade as a function of bias for finite and zero perpendicular magnetic field (device 1)	102
6.9	Demonstration of various coupling regimes of a QD in device 2	103
6.10	Bias spectroscopy of a QD in two different biasing configurations	107
7.1	Micrograph of device 1 with characteristic QPC and QD differential conductance measurements	114
7.2	Schematic representation of the use of a single level of the QD as a spectrometer at zero applied magnetic field	116
7.3	QPC and QD spectroscopy at low magnetic field, for ABS off and on resonance	118
7.4	Illustration of the extraction of gradients for calculation of the gate lever arm, shown for two Coulomb resonances that were used for QD spectroscopy	120
7.5	Density of states in the hybrid NW measured at zero field with QPC and QD, with ABS off and on resonance	121
7.6	finitetheory	123
7.7	QPC and QD spectroscopy at finite magnetic field, for ABS off and on resonance	126
7.8	Extraction of g -factor from spin resolved tunnelling current into the hard gapped superconductor in magnetic field	128
7.9	Differential conductance through two consecutive levels of the weakly coupled QD evolving in field, on resonance with the ABS	131
7.10	Resolving the spin and charge character of a NW state while varying $B_{ }$. .	135
7.11	Resolving the spin and charge character of a NW state while varying chemical potential at an applied magnetic field of 1.4 T	136
7.12	Resolving the spin and charge character of a NW state in device 4 while varying chemical potential at an applied magnetic field of 0.6 T	138
7.13	Resolving the spin and charge character of a NW state in device 1 while varying chemical potential varying parallel magnetic fields	140

Acknowledgments

THE EXCELLENT THING ABOUT BEING AN EXPERIMENTALIST is that a good lab is never lonely. There is always someone to lend a hand, dispense some expert knowledge, or ask ‘how is it going?’ in search of a distraction from an administrative task. The only bad thing is that my list of people to thank is getting out of hand... but let’s begin!

First of all, I would like to start by thanking **Charlie**. Charlie can look at a data set for ten seconds, and in that time come up with ten questions which are worth discussing. He has an unrivaled attention to detail, devotion to clarity, and constant drive to further improve the unique lab which he has built here. I am very grateful to have him as my mentor.

I am grateful to **Ferdinand** for his wisdom regarding both quantum dots and steam engines, and for the opportunity to teach the lab part of his course, which was extremely beneficial for me, and I hope also for the students, and to **Mark** for the opportunity to teach some theory! I would also like to thank **Amir** and also **Javad** for welcoming me in their labs during my research stay abroad, my visit to the East coast was an adventure and a privilege.

Thank you also to all the wonderful people to help keep this lab running; **Claus, Lars** and **Jesper** for maintaining the building, and **Nader, Martin** and **Smitha** for keeping the fabrication facilities in shape. I am especially grateful to **Karolis** for tool maintenance, for excellent teaching, and for becoming one of my very first QDev friends. I would also like to thank **Henri** for his lab management, **Rasmus** and **Benjamin** for endless troubleshooting, and **Maria, Dorte, Katrin**, and more recently **Lena** and **Ingrid**, all of whose superhuman admin efforts keep this ship sailing.

Thank you to **Candice, Geoff, Sara, Teng, Tyler, Mike** and **Peter** for the beautiful material you’ve created and characterized; without it there would be no thesis.

Thank you to my theory advisers and collaborators from overseas for the insights and discussions; in particular to **Georg**, but also **Bernard, Dima, Farhad**, and **Torsten**. Closer to home, I am grateful for discussions with **Andrea, Max, Jens**, and **Karsten**. Special mention to **Waldemar**, who I would be prepared to accept as an honorary experimentalist.

I am immensely grateful to the 2DEG team; you guys make the lab worth coming to even if the fridge is warm. Thank you to **Abhishek, Felix, Asbjørn**, and **Serwan** for your advice,

encouragement, good humour, both in experiments and in life. Also for your excellent (or at least above average) bonfire making. Thank you to **Magnus, Frederick, Will** and **Vasilis** for bringing new ideas, and being a pleasure to work and discuss with. Thank you to **Daniel** for always being up for a good coffee and a good whiteboard session. I am particularly grateful for my TEAM, **Andreas** and **Deividas**. I was lucky to get to work with you guys; it is a pleasure when good colleagues also become good friends.

I am grateful also for the non-2DEG QDev contingent past and present, who are always up for teaching me new physics, sharing a laugh, or projecting a horror movie in the lounge instead of going home. Thank you to **Anasua, Gunjan, Michaela, Natalie, Monica, Eoin, Fabio, Oscar, Fabrizio, Federico, José, Bertram, Torbjørn, Sole, Lazar, Zhenhai, Harry,** and **Steffen**. Thank you to **Lukas** for the climbing trips, and the philosophical discussions. Thank you in particular to my excellent DnD-ers, **Dags, Albert** and **Karolis**. I apologize again for those terrible margaritas I made.

Outside the lab, I could not have continued my physics education without the love and support of my friends from St Andrews, especially **Adam, Tom,** and **Kate** (who thankfully followed me here, otherwise how would we have coped?). I would like to express my deepest thanks to my parents, who are loving and supportive and creative and brave, and to my brothers, who (among other great qualities) are the only tech support I really trust. Lastly, thank you to my partner **John**; I love you very much.

1

Motivation and Introduction

IN THIS THESIS, the focus will be on building up a picture of the bound quantum states which form in superconductor-semiconductor hybrid heterostructures, and on devising creative ways to study these bound states and extract their properties.

A motivation for exploring such structures in detail lies with the search for a physical manifestation of the Majorana bound state¹, predicted to appear at the ends of a proximitized semiconducting nanowire once certain conditions are met^{2,3} and the system enters a topological phase. In general, however, the hybrid materials which we will discuss are feats of materials engineering^{4,5}, and are a veritable playground to explore, irrespective of topology. This work constitutes a toolkit for studying hybrid systems in detail, utilizing different measurement techniques and device configurations to minimize ambiguity in the physics which arises in this overwhelmingly rich platform.

In this section, we will introduce the theoretical concepts needed for the understanding and interpretation of the results presented in this thesis. The devices we will look at were built up by combining several key ingredients. First we take a semiconductor, specifically an InAs quantum well. Here we can confine our carriers in two dimensions, and obtain properties that we are interested in, such as spin-orbit coupling (SOC) and a sizeable g -factor. Then we add a superconducting layer, inducing a pairing gap via the superconducting proximity effect. This semiconductor-superconductor sandwich allows for the existence of bound states in the system. Finally, we bring in quantum dots, confined in the normal semiconducting region. The dots contain information in their own right, and they can also interact with the superconductor and the bound states in the hybrid system. This is the logical flow of the experimental work which will be presented, and I will attempt to follow the same order in this introductory section.

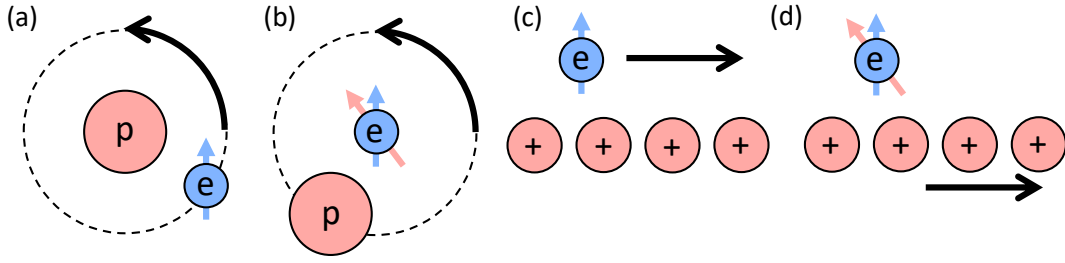


Figure 1.1: (a) An electron, with some spin indicated by the blue arrow, moving in an orbital around a nucleus will in its own rest frame (b) experience the nucleus orbiting around it. The orbiting nucleus generates an effective magnetic field, indicated by the red arrow, which will couple to the electron spin. This is the SO interaction. Similarly (c, d), an electron moving in a lattice experiences a SOC due to the charged ions of the lattice. This figure was adapted from Refs.^{6,7}

1.1 THE 2D ELECTRON GAS

Before we start to bring in elements of superconductivity, let us consider the two-dimensional electron gas (2DEG) by itself. The experiments in this thesis were carried out using InAs 2DEG, of interest due to its sizeable g -factor and the presence of SOC.

In a three-dimensional InAs crystal, electrons can propagate in any direction. However, if InAs is reduced to a layer in a heterostructure, which is confined between two layers of material with a larger band gap, the motion of electrons is confined in a two-dimensional plane. This is provided that the layer thickness of the InAs is on the order of the Fermi wavelength, or below. The structures in this thesis use a quantum well of thickness ~ 7 nm. The 2DEG can be further confined by lateral gating; depleting the carrier density in the well. Confining the electron density to create nanowires leads to quasi-one dimensional confinement. Confining in all spatial directions allows for the formation of a quantum dot, which is a zero-dimensional object. In general, when the length scales of a confined system approach length scales of the order of the characteristic electronic wavelengths, quantized energy levels form, separated by energy of the scale $\Delta E \propto 1/L^2$ (with L the associated dimension of the

system)⁸.

Importantly, charge carriers in InAs are subject to a strong SO interaction. This effect was discovered in atomic physics, and means that the orbital motion of an electron around a charged nucleus interacts with the spin of the electron. Within the rest frame of the nucleus, the electron, which has some spin, orbits the nucleus. But in its own rest frame, the electron is stationary and the nucleus is in orbit around it. The orbiting nucleus generates an effective magnetic field, which couples to the spin of the electron. Similarly, electrons travelling in a crystal lattice experience a SO field, where the ions of the lattice play the roles of the atomic nuclei. This has an important effect on the energy band structure of the material. In semiconductors, like InAs and GaAs, the SO interaction results in spin-dependent, linear shifts in the momentum, lifting the spin degeneracy of the material's energy bands⁹. The effect is illustrated in Fig. 1.1.

1.2 SUPERCONDUCTIVITY AND PROXIMITY EFFECT

1.2.1 A BRIEF BCS REMINDER

Here, we will introduce the core theoretical concepts, giving our thoughts about superconductivity for the rest of the thesis a leg to stand on. For a more detailed and rigorous view, the reader is referred to more specialized sources^{10,11}. A superconductor is distinct from other materials in a way which is very easily summarized: below a (material-specific) critical temperature T_C , a superconductor conducts with zero resistance. Critical temperatures are typically close to absolute zero, ranging from mK to ~ 10 K in elemental superconductors. The superconductor used in the structures investigated in this thesis is Al, with a T_C of 1.2 K¹². For a microscopic description of superconductivity, we turn to Bardeen, Cooper and Schrieffer

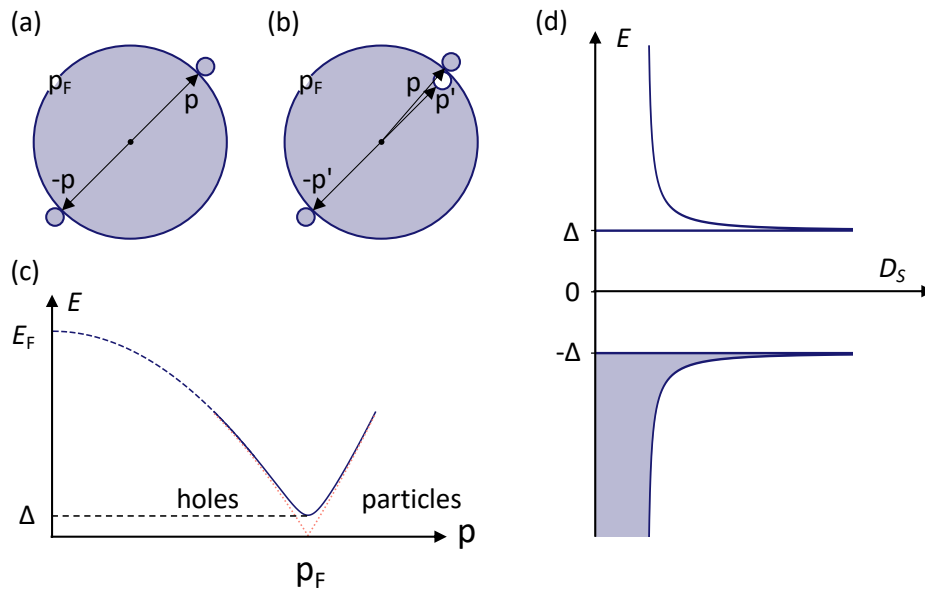


Figure 1.2: (a) Schematic (in momentum space) of the formation of a Cooper pair out of a particle excitation with momentum \mathbf{p} and another particle with momentum $-\mathbf{p}$, shown as shaded circles just above the Fermi surface. This is equivalent to (b) a particle excitation with momentum \mathbf{p} and a removed hole excitation just below the Fermi surface with nearly the same momentum \mathbf{p}' . (c) BCS spectrum of excitations $E(p)$, shown as a solid blue line near the Fermi surface where the quasiparticles are well defined, and as a dashed line at higher energy where they are not well defined. The dotted pink line around p_F shows the spectrum of the normal state $E(p) = \varepsilon(p)$. (d) The density of states D_S of the quasiparticles in a superconductor as a function of energy.

and their hallmark paper in 1957¹³, which describes what is now known as BCS theory. They show that below T_C , the fermionic ground state is not stable against an attraction between two electrons, making it possible for electrons to pair up into ‘Cooper pairs’, with phonons of the ionic lattice mediating the attractive interaction. The formation of the pair is illustrated schematically in Fig. 1.2. We can consider the pair as an object which is made from two electrons with opposite spins and opposite momenta (\mathbf{p} and $-\mathbf{p}$) beyond the Fermi surface, as illustrated in (a). This is equivalent to the picture in (b)¹¹, where the pair is formed out of an electron just above the Fermi surface with momentum \mathbf{p} and an annihilated hole which was formerly in a state with momentum $\mathbf{p}' \approx \mathbf{p}$ below the Fermi surface. Cooper pairs have a total spin of zero and are bosonic, so that they condense at zero energy, forming a coherent ground state which is described by a macroscopic wavefunction. The excitation spectrum therefore has a gap around the Fermi energy E_F of 2Δ , which is the energy required for excitations of the ground state - to break up a Cooper pair. The energy dispersion of these excitations is given by:

$$E(\mathbf{p}) = \sqrt{(\varepsilon(\mathbf{p})^2 + \Delta^2)} \quad (1.1)$$

where $\varepsilon(\mathbf{p}) = \frac{\hbar^2 p^2}{2m} - E_F$ is the energy of a single free electron. The dispersion is plotted in Fig. 1.2 (a). Note that the spectrum of quasiparticles is well defined near the Fermi surface, where it is shown as a solid dark blue line, but is ill defined at higher energies closer to E_F , shown by a dashed blue line. The normal state behavior $\varepsilon(p)$ is plotted as a salmon pink dotted line. A calculation of the density of states (DOS) of the quasiparticle excitation shows that they are

separated from the Cooper pair condensate by the gap Δ :

$$D_S(E) = D_N(\varepsilon) \frac{d\varepsilon}{dE} = \begin{cases} D_N(\varepsilon) \frac{E}{\sqrt{E^2 - \Delta^2}} & (E > \Delta) \\ 0 & (E < \Delta) \end{cases} \quad (1.2)$$

with D_S the superconducting DOS, and D_N the normal state DOS, which is assumed to be constant around E_F . We see that below the gap energy Δ , the quasiparticle DOS is zero. This means that there are no quasiparticles at these energies, only Cooper pairs at zero energy. At energies approaching Δ the DOS diverges, forming coherence peaks. It then decreases again at higher energies, until it resembles the normal state at $E \gg \Delta$. The density seen in Fig. 1.2 (d) is of the standard BCS DOS at zero temperature. The picture changes when finite temperature is considered, since quasiparticle excitation takes place when the temperature is increased from zero, reducing the number of Cooper pairs. This reduces the gap Δ until it closes at the critical temperature T_C . The gap dependence on temperature is as follows¹⁴:

$$\Delta(T) \approx \Delta_0 \sqrt{1 - \frac{T}{T_C}} \quad (1.3)$$

where Δ_0 is the gap at zero temperature. With some simplifying assumptions, the gap size at zero temperature can be related directly to the critical temperature as $\Delta_0 \approx 1.76k_B T_C$. A final quantity from BCS theory which we will bring in here is the superconducting coherence length¹⁰:

$$\xi_0 = \frac{\hbar v_F}{\pi \Delta_0} \quad (1.4)$$

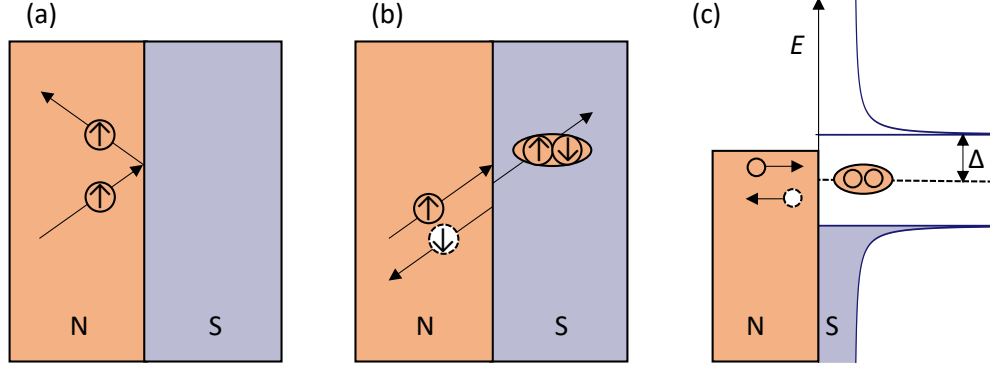


Figure 1.3: Schematic illustrations of reflection at a normal metal - superconductor interface, depicting normal (a) and Andreev (b) reflection processes in real space. Electrons are represented by filled circles, while the white circle with a dashed outline represents a hole. The spins of the particles are indicated with arrows. A Cooper pair, consisting of two electrons, is formed in the superconductor following the Andreev reflection process. The momenta of the particles are represented by black direction arrows. (c) Andreev reflection shown in energy space.

where v_F is the Fermi velocity. This quantity corresponds to the spatial extension of a Cooper pair, and typically range from the order of a few to a few hundred nm¹⁵. This extension will become interesting for us as we consider in the following subsection how superconductivity is able to ‘leak’ out of the superconductor and into a nearby normal material. Note that this characteristic lengthscale changes when we consider adding impurities to the superconductor, as the mean free path l of normal electrons is reduced by their presence. The electrodynamic response changes from the ‘clean’ limit ($l \gg \xi$) to the ‘dirty’ limit ($l \ll \xi$). The changes to the effective coherence length can be approximated as

$$\frac{1}{\xi} = \frac{1}{\xi_0} + \frac{1}{l} \quad (1.5)$$

1.2.2 ANDREEV REFLECTION

For the purpose of the experiments presented in this thesis, we have to concern ourselves not just with superconductors, but with what happens when a superconductor and a normal conductor are placed close to each other. We will therefore now consider a normal - superconductor (N-S) interface. We will start with an electron with an energy $0 < E < \Delta$ coming from a normal region N and impinging on a superconducting surface S, where the N-S interface is fully transparent. Since the energy of the electron is less than the gap, it cannot just create a quasiparticle and enter the superconductor. It can also not undergo a normal reflection in this fully transparent interface scenario, since the momentum transfer required for a normal reflection cannot be provided¹⁶. The process which is allowed is a second order process called Andreev reflection (AR), in which the electron is retro-reflected as a hole which has opposite momentum and spin¹⁷. The hole travels backwards along the trajectory of the impinging electron, as shown in Fig. 1.3 (b). This process gives in total two electrons to the superconductor, with opposite spins. These can then form a Cooper pair and join the condensate. The theory for this process is described in detail by the BTK model¹⁸. This description is not limited to a fully transparent interface; instead the N-S interface is modelled as a δ function with a parameter Z which controls the barrier strength, $V(x) = Z\hbar v_F \delta(x)$. This term accounts for elastic scattering processes. So, when Z is non zero, elastic processes are allowed. This is the case usually in real materials. With increased Z , AR becomes suppressed, and normal reflection processes are allowed, as depicted in Fig. 1.3 (a).

1.2.3 PROXIMITY EFFECT

If we consider the time-reversed version of the reflection process described above, we can picture a Cooper pair being removed from the condensate instead of added, by an impinging hole and a retro-reflected electron. Within the normal region, the electron and hole stay phase coherent for some time, during which they travel some distance; so effectively they remain a Cooper pair for a little while, even though they are now in the normal region. This means that instead of abruptly cutting off at the interface, the density of Cooper pairs decays continuously into the N region. The length scale for this decay is found to be the coherence length ξ ^{19,20}. This means that superconducting properties are not confined strictly within the S region. They can ‘leak’ into a non-superconducting material which is placed in close proximity to the superconductor; hence the name “proximity effect”. There is also a possibility of the reverse effect, known as the “inverse proximity effect”, which leads to a decrease in the density of Cooper pairs in the superconductor, close to the N-S interface. This can cause renormalization of other quantities, such as the g -factor of the superconductor.²¹

1.3 BOUND STATES IN PROXIMITIZED SYSTEMS

Now that we have introduced the basic concepts of superconductivity and Andreev reflection, we turn to the specific case of N-S interface that we are interested in - proximitized semiconducting quantum wells. The quantum states which arise in our systems come about as a result of the unique combination of ingredients that proximitized InAs 2DEGs provide. These are spin-orbit coupling, Zeeman energy, a finite pairing gap courtesy of the superconductor, and the ability to gate the 2DEG, providing confinement and a tuneable density.

We will specifically be interested in Andreev bound states (ABSs). This is an umbrella term, which is used in the literature to refer to a range of quantum states which emerge as subgap states in proximitized systems. Commonly, one pictures Andreev bound states in a Josephson junction. Here, a normal ‘weak link’ separates two superconductors, forming an SNS junction. Electrons propagating in the N region can Andreev reflect at both N-S interfaces, leading to the formation of bound states in the junction resulting from multiple, resonant Andreev reflections. However, considering more broadly than confinement within a weak link, ABSs can emerge as a consequence of a variety of mechanisms, all of which come back to Andreev reflection, and result in a finite DOS at sub-gap energies.

ABSs can result from a quantum dot (QD) being strongly coupled to a superconductor, so that the discrete levels of the dot couple to the superconducting DOS. This problem can be treated theoretically in the single impurity Anderson model if the dot is considered as a spinful impurity in the superconductor, so that the single spin couples to the surrounding electrons²². These states, which specifically result from magnetic impurities, are called Yu-Shiba-Rusinov states^{23–25}.

A one-dimensional or quasi-one-dimensional wire which is proximitized along its entire length by a superconductor can also host ABSs²⁶. In this case, it is possible for the states to have some spatial extent, rather than being very localized objects as in the quantum dot hybridization case described above. The properties of the state and the allowed spatial extension is dependent on properties of the material system such as the amount of disorder, the magnitude and shape of the confining potential, and the strength of the proximity effect in the system. These extended ABSs, which arise in lengths of proximitized nanowire, will be the topic of study within this thesis. In nanowires with a low level of disorder, it is predicted that

a wire hosting such ABSs should undergo a topological phase transition, and that the ABSs should evolve into Majorana bound states, protected by a topological gap.

1.3.1 MAJORANA BOUND STATES

Since the search for Majorana bound states (MBSs) was a major motivation for the current active research into these hybrid systems, we will here go into some detail in reviewing the original theoretical proposals, covering both the mathematical basis, and the proposals for realising the topological phase in real systems.

1.3.1.1 THE KITAEV CHAIN

In 1937, Ettore Majorana found that if he imposed a requirement of a real solution to the relativistic Dirac equation, the result would be a wavefunction which describes a particle that is also its own antiparticle^{27,28}, now referred to as a Majorana fermion. Such a particle has not been observed in nature; at least not as a fundamental particle such as an electron. However, it was discovered that quasiparticle excitations which obey the ‘rules’ set out by Majorana could arise due to particle-hole symmetry, which could be offered by a superconductor under certain conditions²⁹. Such excitations are known as Majorana zero modes (MZMs). Two such MZMs, together, make up a Majorana fermion.

To mathematically describe Majorana fermions, one basically needs a new basis, where we can deal with ‘halves’ of an electron. The easiest way to introduce the concept is through the Kitaev chain, a simple but effective toy model introduced by Alexei Kitaev¹. The Kitaev chain is a one dimensional tight binding model, formed from spinless electrons which are allowed

to interact with their nearest neighbors. The Hamiltonian of the system can be written:

$$H = \sum_j -t(c_j c_{j+1}^\dagger + c_{j+1} c_j^\dagger) - \mu(c_j^\dagger c_j + \frac{1}{2}) + \Delta c_j c_{j+1} + \Delta^* c_{j+1}^\dagger c_j \quad (1.6)$$

with c and c^\dagger the complex operators for annihilation and creation respectively, which obey the fermionic anti-commutation relations³⁰. In the Hamiltonian, t determines the strength of the hopping on the lattice, μ is the chemical potential on site, and Δ is the complex pairing amplitude. The last two terms, which utilize the pairing Δ , show a superconducting pairing between spinless electrons on nearest neighbor sites; this means p -wave pairing, which does not arise naturally in superconductors.

The creation and annihilation operators can be re-written in terms of new fermionic operators, γ_i ³¹, as

$$c_j = \frac{1}{2}(\gamma_1 + i\gamma_2), \quad c_j^\dagger = \frac{1}{2}(\gamma_1 - i\gamma_2) \quad (1.7)$$

so that effectively our fermions are divided in half, as mentioned previously. Inverting this equation, the γ operators, called ‘Majorana operators’, are given by

$$\gamma_1 = (c_j + c_j^\dagger), \quad \gamma_2 = i(c_j - c_j^\dagger) \quad (1.8)$$

These operators are composed of equal part electron and hole, and satisfy the relations

$$\gamma_i = \gamma_i^\dagger, \quad \gamma_i^2 = 1 \quad (1.9)$$

So that the γ_i^\dagger operator indeed creates a particle that is its own antiparticle.

With this Hamiltonian, we can picture a chain with multiple sites, and two operators per

site. For some range of chemical potential μ around 0, the operators on neighboring sites couple, contributing to the total energy of the system. This leaves two operators at the ends of the chain unpaired, and these cannot contribute to the energy. These two operators are the MZMs, and together they form a delocalized fermion which can be occupied or not, without an energy cost to the system. This is the Majorana fermion. This zero-energy occupation possibility leads to a two-fold degenerate ground state of the system at zero energy.

A special property of MZMs, which provided the motivation for enthusiastic attempts to bring them out of mathematical formulation and into the real world, is that while the two MZMs together form a fermion, each individual MZM is in fact an *anyon*³². These anyons acquire a phase factor under exchange, in a process known as braiding - so it is said that they follow braiding statistics³³. In the case of MZMs, the wavefunction changes under exchange of two MZMs, and also if there are more than two MZMs exchanged then the order of the exchanges matters. Because of this, MZMs are known as non-abelian anyons, following non-abelian braiding statistics.

Such anyons are exciting due to their potential applications in quantum computing, or quantum information. Information stored in a system based on MZMs would in theory keep the information protected due to the non-local nature of the MZMs. Information can be encoded in the phases of the MZMs, which can then be manipulated via exchange processes, and read out by fusing the MZMs³⁴. These potentially exciting applications - storing and manipulating quantum information in a novel, protected way - meant that proposals eventually came along for taking the Majorana out of the Kitaev toy model, and into physical systems.

1.3.1.2 INTO THE PHYSICAL WORLD - THE LUTCHYN-OREG MODEL

In 2008, Fu and Kane made a connection between Dirac physics, superconductivity and Majorana physics. The problem with realizing MZMs had been that p -wave superconductivity was required, which has not been clearly demonstrated thus far. Fu and Kane showed that p -wave superconductivity could be effectively created, using proximity effect from a standard s -wave superconductor to act on the helical edge states of a topological insulator²⁹. This breakthrough spurred the thought of using combinations of materials to engineer the desired effects, eventually leading to a now well-known practical proposal: the Lutchyn-Oreg model.

This proposal relies on proximitizing a semiconducting nanowire, which has a Rashba SO interaction term,^{2,3} along its length with a superconductor, in the presence of an external magnetic field which is perpendicular to the Rashba field. The Hamiltonian of the wire itself can be written as follows³⁵:

$$H_w = \frac{1}{2} \int dx \Psi^\dagger(x) \mathcal{H}(x) \Psi(x) \quad (1.10)$$

with

$$\mathcal{H}(x) = \left(-\frac{\hbar^2 \partial_x^2}{2m^*} - \mu - i\alpha \partial_x \sigma_y \right) \tau_z + V_Z \sigma_x \quad (1.11)$$

where m^* is the effective mass in the semiconductor, μ is the chemical potential, α the spin-orbit coupling and $V_Z = \frac{1}{2}g\mu_B B$ is the Zeeman energy produced by magnetic field B . g is the g -factor of the nanowire. $\Psi(x) = (\psi_\uparrow^\dagger, \psi_\downarrow^\dagger, \psi_\downarrow, -\psi_\uparrow)$ are Nambu spinors, the σ_i are the Pauli spin matrices, and the τ_i are the Pauli particle-hole matrices.

The solution to the Hamiltonian yields the dispersion $E_{k,\pm} = \frac{\hbar^2 k^2}{2m^*} - \mu \pm \sqrt{V_Z^2 + \alpha^2 k^2}$. In

the zero magnetic field case ($V_z = 0$), the Rashba SO term removes the spin degeneracy of the 1D parabolic band, so that there are two parabolas, corresponding to spin-up and spin-down projections along the spin-quantization axis, shifted along the momentum axis by $k_{SO} = m^* \alpha / \hbar^2$, and shifted down in energy by $E_{SO} = m^* \alpha^2 / 2\hbar^2$.

If a finite Zeeman field is applied, V_Z mixes the spins, removing the spin degeneracy at $k = 0$. A gap of size $2V_Z$ opens. Projecting a standard s -wave pairing term H_s onto the helical basis ($|\mu| < |V_Z|$) gives intraband (spinless) pairing terms which exhibit a p -wave-like symmetry $\Delta_k = -\Delta_{-k}$, so that the combined minimal Hamiltonian $H = H_w + H_s$ is a realistic implementation of the Kitaev model for one-dimensional, p -wave superconductivity¹.

If the Zeeman field applied surpasses a critical value, satisfying the condition $V_Z^c = \sqrt{\Delta^2 + \mu^2}$, the system goes through a topological phase transition, and Majorana bound states (MBSs) are found at the ends of the proximitized wire.

To attempt to realize this proposal experimentally, one needs a semiconductor with a large Rashba SO coupling, and a sizable proximity coupling to a superconductor. One also needs a large g -factor in the hybrid system, so that the critical field for the topological transition will be reached before the gap of the superconductor is closed by the applied field. The chemical potential μ should also be tunable. This is the system which we have been building up to in this theory introduction, having started with an InAs 2DEG which provides the SO coupling and a large g -factor, as well as a tunable μ , and now having brought in superconductivity and bound states.

1.4 QUANTUM DOTS

Quantum dots are often referred to as ‘artificial atoms’. While they are solid state objects which can be fabricated, they share electronic properties with atoms. For example, they have some characteristic ionization energy, and a discrete excitation spectrum³⁶. In this section, we will introduce the basics behind quantum dots, which will be implemented in our semi-conducting structures later in this thesis.

The energy levels of a QD are discrete, and have a characteristic level spacing δE which depends on the geometry and material details of the dot. The properties of a QD can be explored by connecting it to a source (S) and drain (D) electrode, enabling electron transport spectroscopy. A schematic of a quantum dot is shown in Fig. 1.4 (a). Here, I have depicted a dot formed specifically in an InAs 2DEG, where carrier accumulation is not needed, since the 2DEG is conductive without gating. The gate electrodes, shown in light green, can therefore be depleted to confine a QD in the center, where its location in the schematic is indicated by a light blue oval. Electron transport is possible via the source and drain electrodes, both of which are tunnel coupled to the dots. The gate electrodes which are used to form the dot can also be used to vary the exact number of electrons on the dot, N . When an electron is added, the total charge of dot changes by e . The associated energy change is known as the addition energy, and is a combination of the single-electron charging energy e^2/C and the change in single-particle energy δE . Such charging effects and discrete states have been studied in a variety of quantum dot platforms, defined not only in semiconductors, as we will focus on here, but also in metal grains and molecules³⁷.

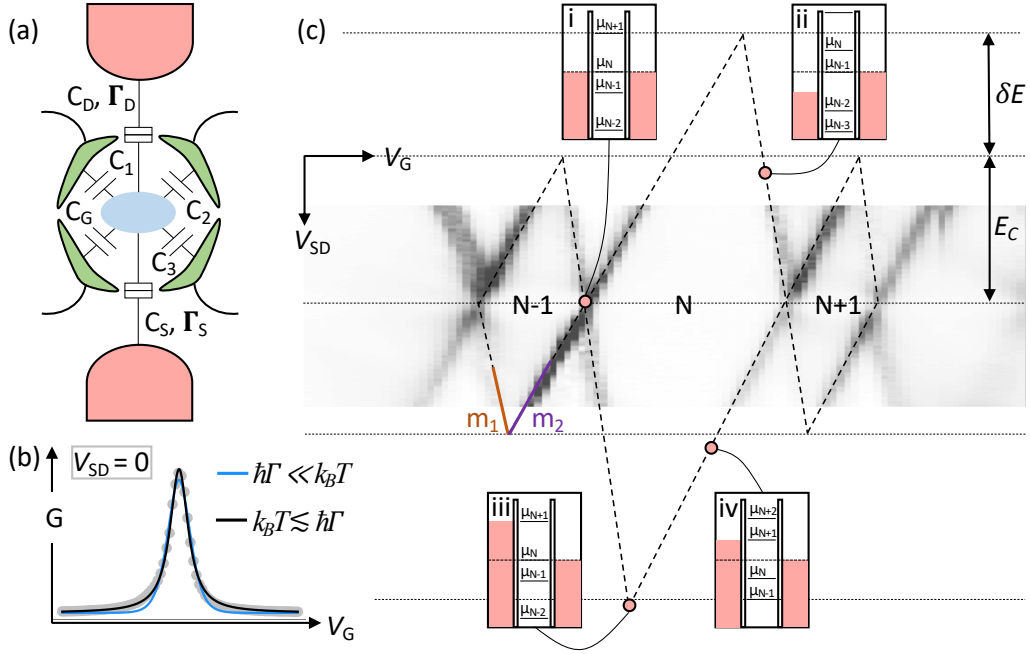


Figure 1.4: (a) Schematic illustration of the lateral formation of a quantum dot in a 2DEG. Gate electrodes (light green) are used to confine the dot, and couple to it capacitively. Transport measurements are possible via the source and drain contacts (pink), which are tunnel coupled to the dot with strengths Γ_S and Γ_D respectively, as well as having some capacitive coupling. (b) Measured conductance (grey dots) as a function of gate voltage V_G sweeping over a Coulomb resonance, fitted with thermally broadened (light blue) and coupling broadened (black) lineshapes. (c) Measured differential conductance as a function of a gate voltage V_G and voltage bias V_{SD} , where the drain is grounded. Coulomb diamonds can be observed, labelled with energy level diagrams showing different resonance conditions (insets). The slopes m_1 and m_2 are indicated; these may be used to calculate the gate lever arm α . The charging energy E_C and level spacing δE are indicated.

1.4.1 COULOMB BLOCKADE

A quantum dot is confined in all three directions, and is therefore considered a zero dimensional object. When the temperature and coupling strengths are small, the Coulomb interaction becomes the dominant energy scale in the problem, and only a single electron can tunnel on or off the dot at a time.

In a transport experiment, one can probe the energy differences between different levels

of the dot rather than the total energies, so it is useful to consider the chemical potential of the dot μ , where $\mu_N = U(N) - U(N - 1)$. Here $U(N)$ is the total ground state energy of a quantum dot with N electrons. μ_N describes the energy needed to add the N^{th} electron to the dot, and the successive chemical potentials form a ‘ladder’, like in the insets shown in Fig. 1.4 (c). The spacing between the potential levels is the addition energy mentioned above,

$$E_{add} = \mu(N + 1) - \mu(N) = e^2/C + \delta E \quad (1.12)$$

The chemical potential ladder can be shifted up and down by changing the voltage on a neighboring gate, with a lever arm $\alpha_i = C_i/C$. For the case of low temperature $k_B T \ll \delta E, E_C$, and $V_{SD} = 0$ V, electron transport is blocked if $\mu(N) < \mu_S, \mu_D < \mu(N + 1)$. This is because there are no electrons in the leads which have enough energy to occupy the next level of the dot, and the dot cannot relax back to $\mu(N - 1)$ because the lead states around $\mu(N)$ are occupied. At this point, the dot is said to be Coulomb blockaded. The blockade can be lifted by changing chemical potential of the dot by gating, so that the next level of the dot is brought on resonance with the leads. The number of electrons on the dot is then allowed to fluctuate between N and $N + 1$, and a current can be measured. Blockade can also be lifted by applying a non-zero V_{SD} . A measurement of the differential conductance signal resulting from varying V_{SD} and V_G , a gate which is capacitively coupled to the dot, is shown in Fig. 1.4. Coulomb peaks, or resonances, are seen at the gate voltages at which the dot is resonant. This leads to a diamond pattern. The lever arms of the electrodes and source and drain contacts can be extracted from the slopes of the diamond ridges, m_1 and m_2 . The resonance conditions are sketched in the insets.

The Coulomb resonances in differential conductance have characteristic lineshapes, which

have a broadening which can be dominated by one of two things: temperature or coupling. The coupling $\Gamma = \Gamma_S + \Gamma_D$ is the combination of the tunnel rate between the dot and the source and the dot and the drain. In the thermally broadened case, $\Gamma \ll k_B T \ll \delta E, E_C$. The lineshape can then be described by

$$G(\Delta V_G) = \frac{e^2}{h} \frac{1}{4k_B T} \frac{\Gamma_S \Gamma_D}{\Gamma_S + \Gamma_D} \cosh^{-2} \left(\frac{\Delta E}{2k_B T} \right) \quad (1.13)$$

here, the maximum of the conductance depends on the coupling asymmetry $\frac{\Gamma_S}{\Gamma_D}$ as well as on temperature as $\sim \frac{1}{k_B T}$. The FWHM is $\sim 3.5k_B T$.

In the case where coupling dominates over temperature, $k_B T \ll \Gamma \ll \delta E, E_C$, the resonances are lifetime broadened instead of thermally broadened. The peak then takes a Lorentzian, or Breit-Wigner form³⁸

$$G(\Delta V_G) = \frac{e^2}{h} \frac{\Gamma_S \Gamma_D}{\Gamma_S + \Gamma_D} \frac{\Gamma}{\Delta E^2 + (\Gamma/2)^2} \quad (1.14)$$

where $\Delta E = -e\alpha_g(\Delta V_g - V_g^0)$ is the level detuning, and V_g^0 is the position of the resonance in gate space. In this case the asymmetry of the tunnel barriers gives the maximum of conductance, while the FWHM simply reflects Γ . Examples of fitting both of these lineshapes to a Coulomb resonance are shown in Fig. 1.4 (b). Such fits can be used to determine a transport regime, and also the ratio of the couplings to the source and drain, but individual coupling strengths cannot be determined in this two-terminal configuration.

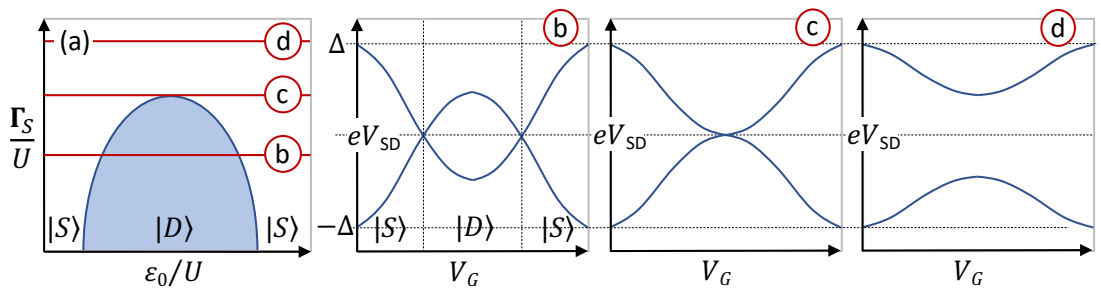


Figure 1.5: (a) Schematic singlet-doublet ground state phase diagram of a quantum dot coupled to a superconductor, as a function of Γ_S and ϵ_0/U . (b-d) Sketches of what measured spectra as a function of gate voltage V_G at increasing Γ_S values, as indicated in (a). In (b) singlet and doublet ground state regions are indicated; in (c) and (d) the coupling to the superconductor is strong enough that the singlet ground state, favored by the superconductor, is stabilized.

1.4.2 COUPLING QUANTUM DOTS TO SUPERCONDUCTORS

When a QD is coupled to a superconducting lead (S) and a normal lead (N), there are two tunnel coupling strengths to consider; Γ_S , between the QD and superconductor, and Γ_N , between the normal lead and the QD. In a case of very weak coupling, where $\Gamma_S \ll \Gamma_N \ll \Delta < \partial E \ll E_C$, the transport is mainly dominated by sequential quasiparticle tunneling. Higher order processes, such as Andreev reflections, are suppressed. Here transport looks like normal Coulomb blockade, but with an energy gap due to the superconducting gap in the S lead. This regime will be explored in detail in Chapter 7.

The situation looks very different if the coupling to the superconducting lead is increased, such that $\Gamma_S \sim \Delta$. In this case, the energy spectrum of the combined QD-superconductor junction is modified. This modification is the result of a competition between superconductivity, which favors the tunneling of electrons pairs with opposite spin and therefore even ground states, and Coulomb blockade, which enforces a one-by-one filling of the dot, allowing both even and odd ground states³⁹⁻⁴⁵.

To analyze this strongly coupled regime, we can consider a single orbital level, which is

spin-degenerate (this is realistic at zero applied magnetic field). When the QD level is singly-occupied, there are two possible ground states; the spin doublet ($S = 1/2, |D\rangle = |\uparrow\rangle, |\downarrow\rangle$), or the spin singlet ($S = 0, |S\rangle$). The competition between the ground states is determined by the energy scales Δ, Γ_S , the charging energy U , and the energy of the QD level with respect to the superconducting electrode ε_0 ^{44,46–54}.

Transport through the system happens via an electron entering from the N lead, exciting the dot to the excited state. The system then relaxes back to the ground state via an emission of a Cooper pair to the condensate, accompanied by the retro-reflection of a hole into the normal lead. This leads a resonance at some $V_{SD} = V$, an Andreev level at the energy $eV = \zeta$, with ζ the energy difference between the excited and ground state. These transport signatures look different for increasing couplings to the superconductor Γ_S , as illustrated in Fig. 1.5. In panel (a), the singlet-doublet ground state phase diagram is shown as a schematic, as a function of Γ_S and ε_0/U . In the rest of the panels, sketches of what measured spectra at different couplings, as indicated on (a), would look like in a measurement as a function of a plunger gate voltage V_G . This means that we are effectively taking cuts through the phase diagram, but sweeping an experimentally accessible parameter instead of ε_0/U . Panel (b) corresponds to weaker Γ_S . On the left and right sides of the plot the QD is deep in a singlet ground state. The doublet excited state approaches the superconducting gap edge, and an Andreev level is observed close to the energy Δ . Approaching the center of the plot, the Andreev resonances approach zero energy, moving together until they cross at the singlet-doublet ground state transition. The characteristic shape of the ABSs during this transition, from singlet to doublet and then back to singlet, is often referred to as a ‘cat eye’. As Γ_S is increased, superconductivity starts to win in the competition against Coulomb blockade. In Fig. 1.5, the ABSs

touch at zero energy but do not cross over; Γ_S is just large enough that the singlet ground state is stabilized across the entire range of V_G . Increasing Γ_S even more [Fig. 1.5 (d)], the singlet ground state is robustly stable, and the ABSs only dip in towards lower energy, without coming close to each other. These considerations of ground state transitions and the effect of coupling a confined object to a superconductor will come in useful throughout the thesis, while considering both QDs and ABSs confined in wires.

2

Materials and Methods

IN THIS SECTION, we will discuss the technicalities of the devices which are presented in this thesis. First we will consider the material platform on which the devices are based, the two-dimensional electron gas (2DEG). Then we will walk through the fabrication procedure, which will get us from a 2" wafer of proximitized 2DEG all the way to nanoscopic devices

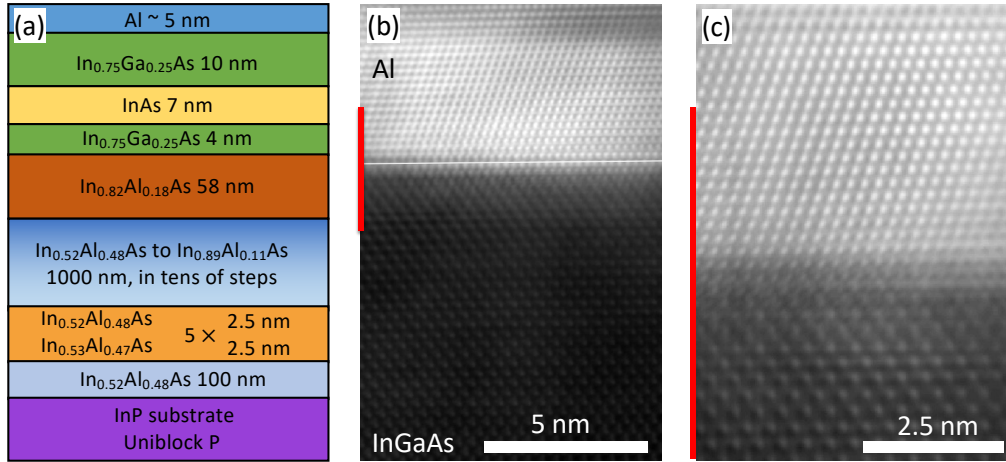


Figure 2.1: Two dimensional electron gas heterostructure, proximitized with Al (a) Schematic of the superconductor-semiconductor heterostructure, with representative layer thicknesses. (b,c) Transmission electron micrographs provided by the Manfra group at Purdue University, showing the interface between the semiconductor and the proximitizing superconducting layer.

which are ready to measure. Lastly, we will discuss how we interface between the electronics in our experimental setup and our devices, and then walk through the electrical configurations for the two main types of measurement used for the experiments in this thesis: local and nonlocal tunneling spectroscopy.

2.1 PROXIMITIZED TWO-DIMENSIONAL ELECTRON GAS

The devices presented in the main body of this thesis were fabricated on wafers of 2DEG proximitized with *in situ* grown Al. These wafers were grown and provided to us by the Manfra group at Purdue University.

Molecular beam epitaxy (MBE), a technique which allows for growth of highly homogeneous layers with a fine control of the layer composition⁵⁵, was used for the growth. InP² wafers were used as substrates, despite the 3% lattice mismatch between InP and InAs⁵⁶. This

is because the substrate option which is more closely matched, GaSb, is known to show trivial edge conduction at mesa edges, complicating transport measurements⁵⁷⁻⁶⁰. The composition and thickness of the MBE grown layers is shown in Fig. 2.1 (a). Starting at the substrate, a superlattice of InAlAs-InGaAs is grown, serving as trap for dislocations. A graded buffer of $\text{In}_{1-x}\text{Al}_x\text{As}$ is then grown to transition from the lattice constant of InP (5.87 Å) to that of InAs (6.06 Å) over the distance of ~ 1 mm. The quantum well itself is grown on top of the buffer layer, and is formed by sandwiching ~ 7 nm of InAs between a top and bottom barrier of material with a larger band gap (in Fig. 2.1 (a) InGaAs is shown, but it is also possible to use for example InAlAs).

Finally, Al is deposited *in situ*. This way of depositing Al leads to a higher quality interface, and was developed for 2DEGs⁵ following the success of a similar method applied to vapour-solid-liquid (VLS)-grown NWs⁴. The Al film is able to proximitize the quantum well in these structures because the well is not buried deep beneath the surface, but is instead separated from the superconductor by a barrier of only ~ 10 nm. The interface between semiconductor and superconductor in a heterostructure grown using this method is shown in transmission electron micrographs (TEMs) provided by the Manfra group in Fig. 2.1 (b,c).

The goal of the growth is to have relaxed lattice strain, and a continuous Al film with minimal thickness variation across the wafer. The relaxed strain can be observed as a hatch-like pattern in dark-field optical microscopy.* We typically see some defects in the Al surface, which appear clearly in optical micrographs. The devices which we fabricate are on the order of a few microns in size, so typically the large visible defects in the Al are not disruptive to a functional device. They are statistically likely not to overlap with the small device, and if

*A tip for the fabber... if you are inspecting your chip before starting fabrication and you cannot see the hatch pattern in dark field, your chip is upside down and you should flip it over before you proceed.

they do the device is simply unmeasurable rather than partially crippled. A surface roughness of the Al can be measured using atomic force microscopy (AFM) to be around 1 nm - a significant variation, considering that the desired thickness of the layer is only ~ 5 nm.

While the parameters shown in Fig. 2.1 (a) are representative of the values used for the growths in general, variations are made to fine-tune the properties for a given wafer. Two of the main properties of the material that are important in our experiments are the mobility μ of the 2DEG and the size of the proximity effect-induced superconducting gap. There is a trade off between these two properties; if the barrier between the InAs and the Al is made thicker, the quantum well is protected against the interface disorder, and higher mobilities are accessible, but the proximity effect is weaker and the induced gap is smaller⁶⁰. In general, mobilities (measured in a dilution refrigerator with a base temperature of ~ 15 mK using a Hall bar) are around $20\,000\text{ cm}^2\text{V}^{-1}\text{s}^{-1}$ - $90\,000\text{ cm}^2\text{V}^{-1}\text{s}^{-1}$. The electron density, calculated from the transverse resistivity of the Hall bar, is $\sim 1 \times 10^{16}\text{ m}^{-2}$ at peak mobility values, corresponding to a Fermi wavelength $l_F = 25$ nm and mean free path $l_e = 0.8\text{ }\mu\text{m}$.

These materials are well suited for our purposes for the experiments in this thesis due to the combination of the high InAs g -factor, the induced superconductivity, and the ability to control the electron density to make two dimensional structures. As we will see, this allows us to be flexible with device design, and expand upon the rich physics available in hybrid superconductor-semiconductor systems in ways which would be difficult using a different platform such as VLS NWs.

2.2 DEVICE FABRICATION

This section is a walk-through of the fabrication process, with explanations of the techniques used and some tips for the future fabber. For our standard recipe, which contains less insight but more exact details in a more concise manner, see Appendix A.

2.2.1 FROM WAFER TO CHIP

We receive the proximitized 2DEG material from the Manfra lab in the form of 2" wafers. Once received, these are inspected in both bright and dark field optical microscopy. The entire wafer is then spin-coated with PMMA and stored in a Nitrogen cabinet until further use. When we wish to fabricate on the material, we cleave sections of it into small chips, ~ 3 by 5 mm. These are made with a high precision, manual scriber. This has a rotational stage for alignment. The chips are cleaved on a cleaving block, by applying a gentle force with tweezers. We then proceed with fabrication on an individual chip, which is cleaned before the first fabrication step for 5 min in 1,3 Dioxolane, followed by squirts of acetone, then isopropanol (IPA), and then a blow-dry with a nitrogen gun.

2.2.2 ELECTRON BEAM LITHOGRAPHY

The workhorse of our nanofabrication process is a technique called electron beam lithography (EBL). This involves spin-coating the chip with a resist, and then patterning the surface by ‘writing’ with a beam of accelerated electrons. Exposure to the electron beam renders the resist either more soluble (a positive tone resist), or less soluble (a negative tone resist). We use polymethyl methacrylate (PMMA)-based resists. These consist of PMMA polymer dissolved in a solvent. Exposure causes scission of the polymer chains, making this a positive tone resist.

We use A4 for most processes in our 2DEG fabrication flow, but a thicker resist stack of two layers EL9 and a single layer A4 is used for the lithography step which defines the bond pads and connecting lines to gates, since some of the gates must crawl up the mesa walls.

Once the pattern has been exposed, the exposed regions of the resist are selectively removed by immersing the chip in a ‘developer’. We use an MIBK:IPA 1:3 solution at room temperature. This leaves only the desired areas of the chip exposed, so that one can then proceed with selective etching, or deposition in the desired region. The fabrication process is based on a series of EBL exposures, each enabling the next step. The lithography tool used for this project was an Elionix ELS-500 100 kV system, and a software called Beamer was used to produce machine files to control the lithography.

The EBL tool has a certain ‘write field’, which is the area it can write in for a fixed stage position. Typically the patterns which we require cover multiple write fields. This means that once the tool is finished writing within one field, it blanks the beam and moves to the next one. In order to avoid discontinuities or overlaps between fields, the EBL system uses a stage position system based on laser interferometry. This allows for write fields to be stitched with nanometer scale precision.

For fine features (~ 100 nm), there is usually a difference between the dimensions defined in the design and the dimensions of the features which come out after the lithography process. This comes from electron scattering processes in the resist, which make the features come out slightly wider than designed. The difference between the designed and actual size is referred to as the bias⁶¹, and this is something which we can characterize and then correct for in Beamer.

The scattering of electrons in the resist can degrade the quality of the final pattern, especially in regions with a high density of features. This is known as the ‘proximity effect’ in

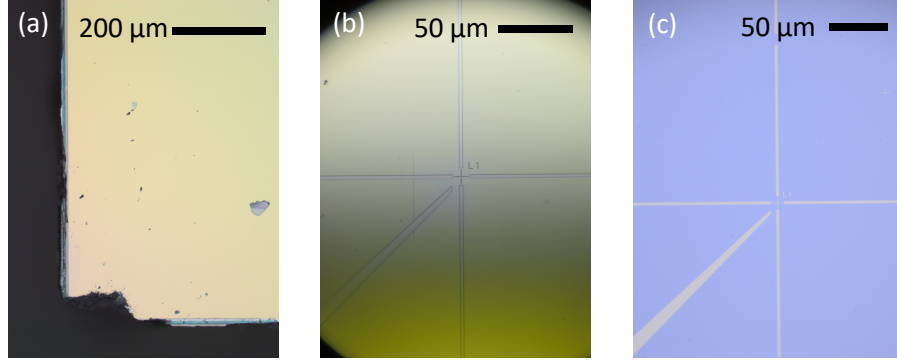


Figure 2.2: Electron beam lithography of alignment marks on superconductor-semiconductor hybrid chip (a) Optical micrograph of a corner of the chip before the start of fabrication. The chip is spin-coated with PMMA. (b) Optical micrograph taken after exposure and development. The PMMA is removed where the alignment mark will be placed. (c) Optical micrograph of Au alignment mark after metal deposition and liftoff steps.

EBL⁶². This can be compensated for using the Dose Correction feature of the EBL system.

An example of the results of EBL in the first fabrication stage of one of our samples is shown in Fig. 2.2. In panel (a) a corner of the chip is shown at the start of fabrication. The chip is already spin-coated with PMMA, but no features are present on it. The EBL system is then used to write a pattern of alignment marks around the edges of the chip. Each mark consists of a small cross in the center and a bigger cross around the outside, along with a letter label (for example 'L' for marks on the left side of the chip) and a number. The bottom left corner is considered the origin, and here the mark has an additional slanted line, which helps to easily discern the orientation of the chip. This bottom left region is shown in Fig. 2.2 (b), which is an optical micrograph taken after the development step. Here the resist which was exposed has been dissolved away, leaving the alignment mark pattern exposed and the rest of the chip covered by resist. Ti/Au is then evaporated onto the surface (see next section), after which the chip is placed in a 'lift-off' solution which dissolves the remaining resist. This leaves Ti/Au only on the regions of the chip which were exposed, so that we are left with a pattern

of Ti/Au alignment marks around the chip. The bottom left alignment mark is shown in Fig. 2.2 (c).

During the remaining fabrication steps, a lithography step is used to define the areas in which the chip will be etched, or material will be deposited. The alignment marks deposited in the first step are used as part of the EBL process, to insure that layers written with separate EBL steps are aligned with each other. The general procedure is summarized in Fig. 2.3. Using a series of EBL steps, we etch out a mesa for each device, defining the general shape of ohmics running away from a central region. There is then an additional etching step in which Al is selectively removed, making the NW which forms the heart of our device, and in some cases superconducting leads. Dielectric is then deposited globally on the chip, and finally Ti/Au electrostatic gates and bond pads are evaporated, providing control over the device and connection to the outside world.

2.2.3 WET ETCHING

Wet etch processes were used to define a mesa profile of the devices and bond pads, and to selectively remove the Al thin film to make the desired device configurations.

The mesa etching step is performed first. This involves lithographically defining the areas to be removed. After development, the chip is cleaned with oxygen plasma in an asher. The resist is then reflowed for 2 min on a hotplate at 120 °C. An Al etch is then performed, to remove the Al thin film, in those regions. We do this using Al etchant D (Transene), prepared at 50 °C in a hot water bath. Two beakers of ultra-pure water are also prepared in the hot bath, one for stopping the etching process and one to use for measuring the temperature of the liquids in the hot bath with a thermometer. A room temperature beaker of ultra-pure

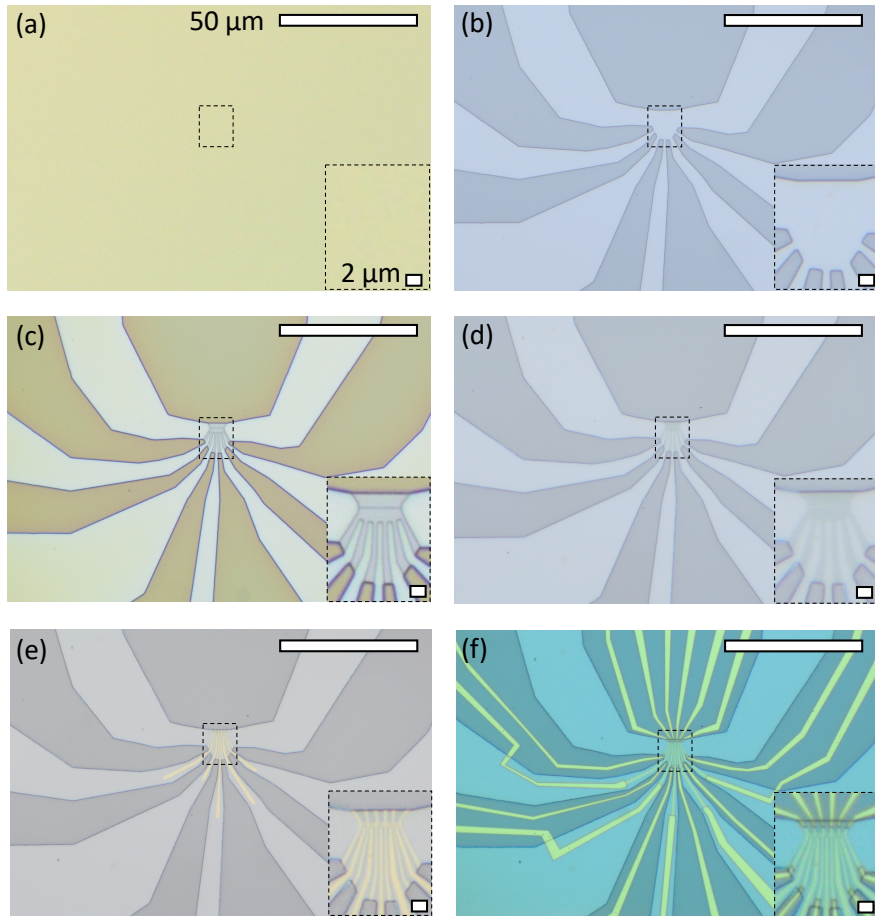


Figure 2.3: Optical micrographs of one device during fabrication workflow. Insets show a close-up of the core device region. (a) Blank chip, coated in PMMA, inspected before the start of fabrication. (b) Image after the mesa etch step. The darker regions are where the Al thin film and ~ 300 nm of mesa have been etched away, the lighter regions are where the 2DEG and proximitizing Al remain. (c) After the Al etching step, in which only Al is etched away in the device region. Image taken directly after etching, with PMMA still present on the chip. The effect of the etch can be seen most clearly in the inset; a thin Al strip expanding into planes at either side and five superconducting leads are formed. (d) After the PMMA is removed and a global layer of HfO_2 is deposited. (e) After the deposition of the inner (fine) gates, which are visible in gold. (f) After the deposition of the outer gates - a thicker layer of Ti/Au. These overlap with the ends of the inner gates and run out to the bondpads (deposited in the same step, not pictured in this figure).

water is also prepared. The Transene beaker and one of the pure water beakers in the bath are placed next to each other in the bottom left corner of the bath, while the ‘test’ water is placed towards the upper left. The level to which the beakers are filled should be equal, and should reach stop at the level of the water in the bath, for optimal thermalization [†].

The etch itself is performed by swirling the chip in the hot transene for 5 s, in the hot pure water for 20 s, and then for 40 s in the room temperature pure water. All swirling should be rigorous. This is the one fabrication step during which having shaky hands can work to your advantage. The chip is then blow dried with a nitrogen gun.

Once the Al is removed, the next step is to etch deep into the mesa, using a solution of $\text{H}_2\text{O} : \text{C}_6\text{H}_8\text{O}_7 : \text{H}_3\text{PO}_4 : \text{H}_2\text{O}_2$ (220 : 55 : 3 : 3) at room temperature. This mixture is placed in a wide, shallow glass beaker, and is stirred with a magnetic stirrer throughout the etching process. The chip is placed on the bottom of the beaker, near the stirrer, and is rotated by 90° every 30 seconds during the 9 minute etch. Afterwards the chip is thoroughly rinsed in ultra pure water for one minute. The remaining resist is stripped off the chip using dioxolane, followed by squirts of acetone and IPA, and a blow-dry. The result of such an etch is shown in Fig. 2.3 (b). The darker colored regions are where the Al and ~ 300 nm of mesa have been etched away.

Next, another Al etch is performed, this time to define the structure of the devices. The pattern is defined with EBL and the Al is etched in the same way as before, with hot Transene D. The result of the etch is shown in Fig. 2.3 (c); the image is taken directly after, with the resist still on the chip. This finer etch step defines the thin Al strips which will form the NWs

[†]Note that the particular placement of the beakers in the bath is optional, this is my personal preference which I have found works well. The water level considerations, on the other hand, are not optional. Try to thermalize properly or you will have a bad time.

at the heart of our devices, as well as superconducting leads which reach in towards the device. The remaining resist is again stripped away with dioxolane, and the chip is rinsed as above.

2.2.4 DIELECTRIC DEPOSITION

A global layer of HfO_2 dielectric is deposited on the chip at this point during the fabrication. This is to prevent electrical contact between the device and the electrostatic gates which we will deposit on top to control it. Atomic layer deposition (ALD) is used to grow the dielectric. The system used currently in the group is the Savannah S100 from Cambridge Nanotechnology. The growth is performed at 90°C , with 150 pulses of TDMAH each of which is followed by a pulse of H_2O . This leads to a growth of ~ 15 nm of HfO_2 . An optical micrograph of one of the devices after dielectric deposition is shown in Fig. 2.3 (d). The devices imaged here have only one layer of metal gates, however for designs which required two layers, another growth of dielectric is performed in the same way between the gate layers.

2.2.5 METAL GATE DEPOSITION

After the dielectric deposition, metal gate electrodes are deposited, giving us electrical control over the device. The gate deposition is performed in two layers, meaning two separate EBL exposures. The first is to define the fine features of the gates, which cover the active region of the device. After development, the metal is evaporated onto the chip using an electron beam evaporation system (AJA international). A sticking layer of 3 nm of Ti is used, followed by 5-10 nm of Au. The evaporation is followed by a liftoff process, which removes the rest of the resist, and with it the metal which adheres to it. Figure 2.3 (e) shows a device after this liftoff process; the resulting features are very fine, and barely resolvable in our optical images.

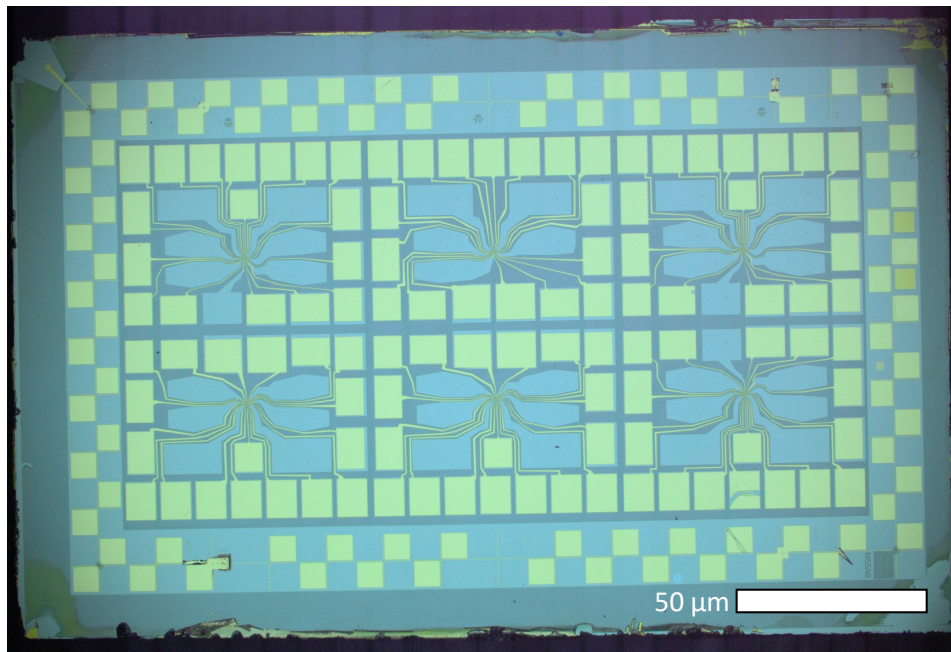


Figure 2.4: Optical micrograph of the entire chip after a complete fabrication round. The chip contains six devices. The Ti/Au gates and bondpads can be seen in gold. The ohmics, which consist of InAs 2DEG topped with Al, appear light blue. The areas between the ohmics and between the bondpads are a darker blue, these are trenches where the mesa has been etched away. Ti/Au squares around the outside of the chip are patterned for use as test bondpads.

The last EBL step is used to write what we refer to as the ‘outer gates’; this defines the parts of the gates which overlap with the edges of the inner gates, and then crawl out toward the bond pads. The bond pads are also metalized in this step. In this case, a thicker layer of metal is evaporated, ~ 350 nm. Some tilt is also applied to the stage while the evaporation takes place. Both of these things are to ensure that the gates are able to crawl up the mesa edges, and make contact between the inner gates and the bond pads. An optical micrograph after the liftoff process for this step is shown in Fig. 2.3 (f).

A final optical overview image of the chip taken after fabrication is complete can be seen in Fig. 2.4. Here, one can see the metalized bond pads which surround each of the six devices on the chip (yellow), as well as Al pads (blue) which are used to contact the ohmics.

2.2.6 FINAL IMAGING

After fabrication is complete, we use scanning electron microscopy (SEM) to inspect the results of the fabrication more closely. There is some evidence that the electron beam of the SEM causes charges to get trapped around defect in the dielectric⁶³, so to avoid the possibility of such charge traps test structures are fabricated on the edges of the chip, simultaneously with the real devices. These test structures are what we image with the SEM.

The purpose of the image is to inspect firstly the Al etch (whether the wires are indeed the desired width or if they are too wide, or too narrow and therefore uneven and possibly broken), and secondly to inspect the gates, checking if they look correctly aligned with the Al strip, and whether they are shorted to each other at any point.

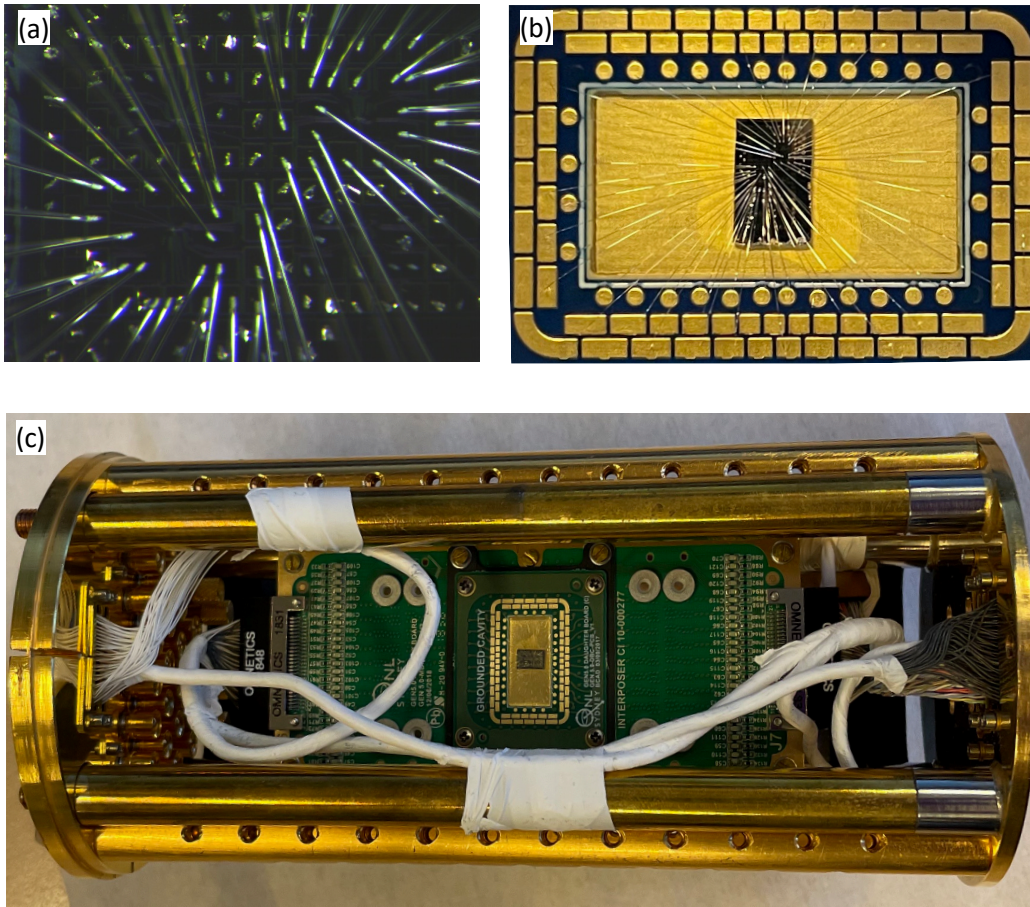


Figure 2.5: Connecting the device to the outside world (a) Two devices bonded with Al wire bonds. The other two devices visible in the micrograph have marks on the bond pads which show that these devices have previously been bonded. (b) The chip is mounted on a 'daughterboard', and the wire bonds can be seen extending from the two devices to the pads on the board. (c) the daughterboard is in turn mounted on a motherboard, housed in the sample puck. Once an outer shield of copper is put on, this puck can be loaded into the dilution refrigerator.

2.3 LOW TEMPERATURE MEASUREMENT

2.3.1 MOUNTING AND WIRE BONDING

Once the devices are fabricated, imaged and deemed satisfactory, the time comes to connect them to the outside world. The chip is glued to a PCB which we refer to as the ‘daughter-board’ using a drop of PMMA and baked on a hotplate to secure. *A tip for the fabber: during baking, it can sometimes happen that the chip pops off the board. It is up to the individual what to do with this information; we have lately tended to hold a gloved hand nearby. Catching the chip in your gloved hand is not ideal, but it is better than losing it or having it impact on a hard surface.*

Once mounting is complete, the chip is wire bonded with Al bond wire, connecting each gate and ohmic to a pad on the daughterboard. The system used is an automatic wedge bonder (F&S Bondtec 5630). In the image of the chip shown in Fig. 2.4, a checkerboard pattern of Au (yellow) and Al on InAs (blue) squares can be seen around the outside of the chip. These squares are not connected to any of the devices, but are used for making test bonds to optimize the bonder parameters for each of the materials being bonded to. It can happen that the parameters need to be adjusted constantly throughout the bonding session, in which case we switch back and forth between making more test bonds, and doing real bonds. †

A photograph of a chip with two devices bonded is shown in Fig. 2.5, close up in (a) and with the daughterboard in (b). The devices measured during this project have around 17 gates and between 5 and 7 ohmics each. Two of the ohmics are used as ground planes, and these are each double bonded to reduce the total resistance to ground. This large number of

†This is extremely annoying and I do not wish it on anyone.

bonds required per device means that we are able to bond only two devices per cooldown, in order for the bonds to fit comfortably.

Once bonded, the daughterboard is mounted on a motherboard which is housed in a puck, as shown in Fig. 2.5 (c). Additional shielding (not shown in the photo) is added, and then the puck is bottom-loaded and cooled in a cryo-free dilution refrigerator (Oxford Instruments Triton 400, with a 1-1-6 T vector magnet). The temperature of the mixing chamber temperature was ~ 15 mK, measured with a RuO₂ thermometer. All electrical lines in the cryostat are equipped with multi-stage cryogenic RF and RC filters, which are built in house. These have a cutoff frequency 80 MHz and 0.7 kHz respectively.

2.3.2 TUNNELING SPECTROSCOPY

Two-terminal tunneling spectroscopy is used throughout this thesis to access the density of states of the system under investigation. In this method, there is a tunnel barrier between the source and the drain electrodes. The energy at which one measures is selected by applying a source-drain bias V_{SD} , and then considering the tunneling current which flows across the barrier. A differential measurement can be taken using a lock-in amplifier. A small sinusoidal component with RMS amplitude dV_{SD} is added to V_{SD} . The resulting tunneling current modulation dI can be measured with the lock-in at the frequency of the applied voltage modulation, giving the differential conductance

$$\frac{dI}{dV_{SD}} \tag{2.1}$$

which is proportional to the density of states in the deep tunneling regime²⁰. This can be imagined more clearly as follows: for a change in energy (given by dV), we measure how

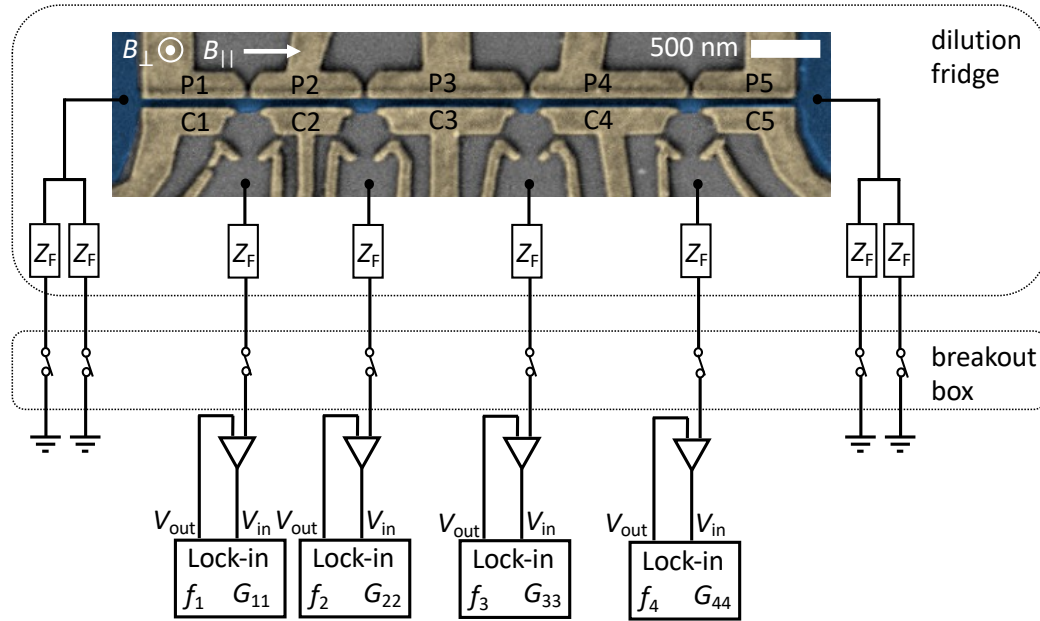


Figure 2.6: Schematic of the electrical setup for local conductance measurement. The sample itself is cooled in a dilution refrigerator. It consists of a NW, formed by depleting the gates labelled P and C, with normal leads at four probe locations. The smaller gates below the C gates can be used to form quantum dots if energized, but we need not consider them in this section. Connections to the measurement electronics are via electrical lines of impedance Z_F . For each of the four probe locations, a current to voltage amplifier is connected, and used to measure the tunneling current across the tunnel barrier formed by depleting with the edges of the C gates. Each current to voltage amplifier is connected to a lockin amplifier, which is used to measure a local conductance signal. The Al strip expands into planes on the left and right side, both of which are double bonded and grounded at the breakout box.

many more fermionic states become available for tunneling (dI). If we consider the density of states in the source to be uniform, then the differential conductance gives us a measure of the density of states in the drain. When doing such a two-terminal measurement, one needs to consider the line impedances for the source and the drain, so that their contributions can be subtracted. Alternatively, one can do a four probe measurement, where the voltage drop over the sample is directly measured. For the tunneling spectroscopy measurements in this thesis we stick to the two-terminal configuration.

A schematic for a measurement configuration for one of the devices measured during this project is shown in Fig. 2.6. This looks a little different from the two-terminal concept described above; this is because we have multiple probe locations along the length of the device. The device consists of a thin Al strip (blue), which proximitizes the 2DEG underneath and screens it from the action of the gates. The Au gates (yellow/gold) are used to deplete the carrier density in the 2DEG until it is confined to the quasi-1D region beneath the Al strip, forming our NW. The gates are also used to separate the NW into segments, with multiple probe locations. The tips of the depleted C gates form tunnel barriers. So we end up with four sources and four tunnel barriers, all of which share a drain (the grounded NW).

We can then apply a source-drain voltage bias on each of the four leads. For each lead, the ac component dV_{SD} , sourced from a lock-in (Stanford Research SR830), and the dc component V_{SD} , sourced from a DAC, are combined via a divider (ac division factor ~ 100000 , dc ~ 10000) and applied to the lead via a current to voltage converter (Basel Precision Instruments SP983c). The resulting current can then be amplified via the Basel, and detected using the respective lock-ins, enabling calculation of differential conductance for each lead. This gives us a measure of the density of states at each of the probe locations.

The line impedance Z_F at lock-in frequencies $< \sim 100$ Hz is dominated by a resistance of $0.88 \text{ k}\Omega$, coming from a $0.180 \text{ k}\Omega$ line resistance and $0.70 \text{ k}\Omega$ filter resistance.

2.3.3 NONLOCAL CONDUCTANCE

Another differential measurement technique which was employed during this project is known as nonlocal conductance. *Before getting into detail; here is a colloquial explanation. ‘Local’ conductance, as described in the previous section, means if you wiggle on the left side of a NW, you also measure on the left. ‘Nonlocal’ conductance involves doing the opposite: if you wiggle on the left, then you measure on the right.*

In more detail, the detection scheme used for nonlocal measurement is shown in Fig. 2.7. Here the measurement is carried out with just two probes, labelled 2 and 3. The other leads are floated at the breakout box, and the Al strip is still grounded at the planes which it extends into on both sides, as in the local measurement. The two connected leads are attached to individual low-noise high-stability current to voltage converting amplifiers as before, with a gain of 10^8 V A^{-1} . The ac and dc voltage inputs for the amplifier are sourced as before from separate lockin amplifiers and a DAC respectively. The thing that makes this nonlocal detection different from the local measurement described in the previous section is that the output of each Basel amplifier is measured using two lockin amplifiers instead of one. For each one of the two leads, the signal is measured a) with a lockin whose detection frequency is the one which is applied as dV_{SD} on the lead in question, and b) with another which detects with the frequency of the ac signal which is applied to the other probe. This detection technique has recently been employed in other experimental works^{64,65}, and will here be the topic of Chapter 4.

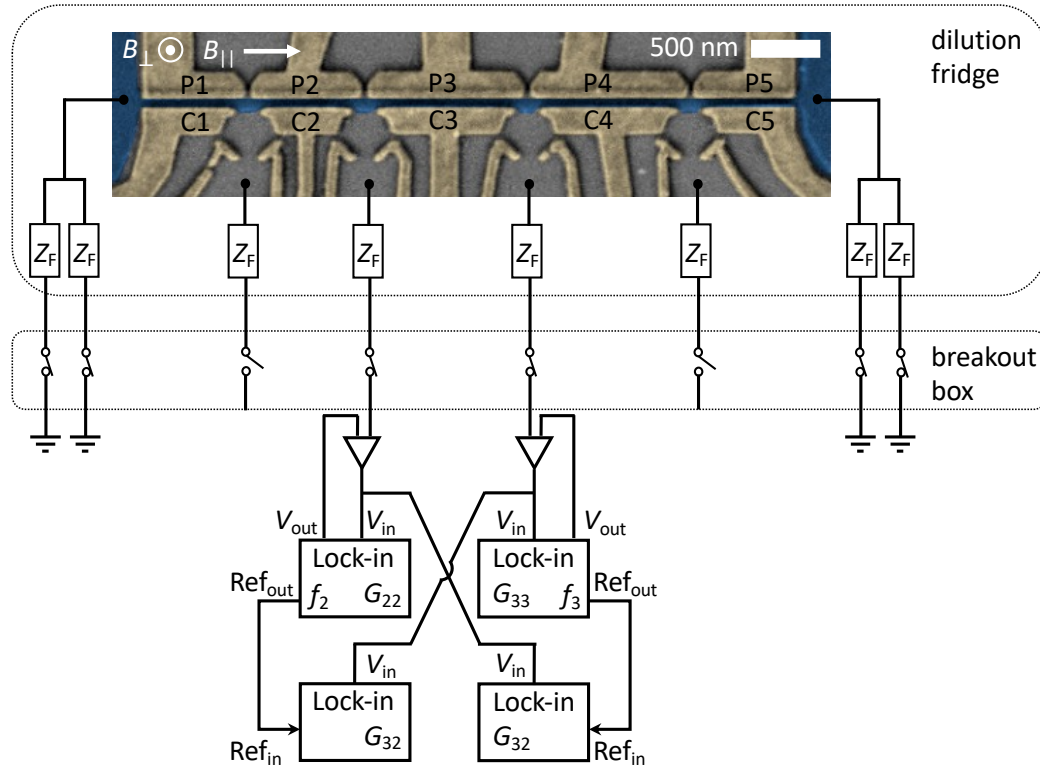


Figure 2.7: Schematic of the electrical setup for nonlocal conductance measurement. The sample itself is cooled in a dilution refrigerator. It consists of a NW, formed by depleting the gates labelled P and C, with normal leads at four probe locations. Connections to the measurement electronics are via electrical lines of impedance Z_F . The Al strip expands into planes on the left and right side, both of which are double bonded and grounded at the breakout box. For nonlocal measurements only two of the four probe locations are used; the unused leads are terminated by an open circuit at the breakout box. Current to voltage amplifiers are connected to the two leads used for the measurement, and used to measure the tunneling current across the tunnel barrier formed by depleting with the edges of the C gates. Four lockin amplifiers are used, in the configuration shown, to measure the four elements of the conductance matrix.

2.3.4 TUNNEL BARRIER DESIGN

In order to perform differential conductance measurements, local or nonlocal, and access information about the density of states of our system, a tunnel barrier must be formed between the source (in our case the lead) and the drain (in our case the NW under investigation). Over the course of the project described in this thesis, several different designs of the tunnel junction region were used. In this section, main design options (shown in Fig. 2.8) will be summarized, the pros and cons of these options, and the thoughts that went into the differences between them.

2.3.4.1 SUPERCONDUCTING LEADS

In Fig. 2.8 (a), one can see one of the barrier regions of a multiprobe device with superconducting leads. In this configuration, the superconducting lead is etched from the epitaxial Al layer, and extends all the way towards the Al strip, so that there is a gap of ~ 50 nm between lead and NW where the 2DEG is not covered by Al. The gate labelled T (for ‘tunnel’) extends over the gap; it is used to deplete the 2DEG in this small unscreened region, so that a tunnel barrier is formed between the source and drain. The lead is superconducting at zero field, but the gap softens at ~ 100 mT applied parallel magnetic field, so that above that value the transport can be considered N-I-S⁶⁶. Making barriers in this way reliably gives us access to spectroscopy in the tunneling regime, but the shape of the potential is such that the junction is likely multi-channel. One should also note that defects like accidental, small quantum dots have a strong tendency to form in these barriers. When attempting to do tunneling spectroscopy measurements one therefore has to go to pains to stay away from these defects in order to properly access the DOS in the NW.

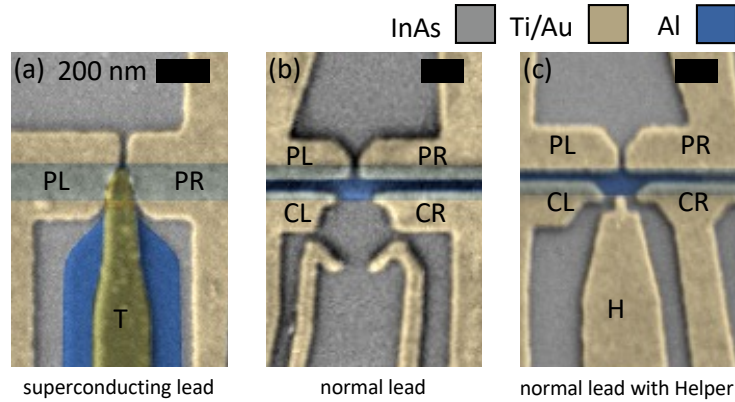


Figure 2.8: Scanning electron micrographs illustrating the three main ways of forming tunnel barriers for differential conductance measurements used during this project. (a) A superconducting lead is separated by a short distance (~ 50 nm) from the Al strip. There are two layers of gates in this design. The first contains the gates PL and PR, the second contains the gate T, which is used to control the tunnel barrier. (b) A semiconducting lead, with a QPC-like tunnel barrier to the NW that is formed by the depletion tips of the C gates. The P and C gates are used to form the NW. The two unlabelled gates at the bottom of the image can be used to form a quantum dot, but need not be energized for differential conductance measurements. (c) A semiconducting lead with a tunnel barrier formed similarly to (b), except with an additional gate labelled H for ‘Helper’. This gate can be operated at a negative or at a slightly positive voltage to adjust the tunnel barrier.

2.3.4.2 SEMICONDUCTING LEADS

A second option for the formation of the tunnel barrier is shown in Fig. 2.8 (b). Here, a normal lead is used instead of a superconducting lead, and the gates which form the quasi-1D channel of the NW are split into two. These are the P gates, which deplete the 2DEG to form the top of the NW, and the C gates, which form the bottom of the NW, but also (crucially) form a tunnel barrier between their two tips. The shape of the tips is designed in an attempt to form a QPC-like barrier. The particular design shown in (b) has two additional gates below the C gates; these can be used to form a quantum dot deliberately in the tunneling region, but that is not part of the current discussion. Making a barrier in this way allows us to try to engineer the shape of the potential to a greater extent than the version shown in (a), so that

we can try to create a saddle-point potential and potentially get down to a single mode tunnel junction. We also find that accidental quantum dots are less commonly found with this type of barrier. However, a downside of this design is that we found that barriers designed in this way to have a high failure rate; the junctions were quite difficult, and sometimes impossible, to tune into a good spectroscopy regime.

2.3.4.3 SEMICONDUCTING LEADS WITH HELPER GATE

In Fig. 2.8 (c), a design is shown which takes advantage of the QPC idea described above, while mitigating the problems mentioned. This is through the addition of another gate, suitably labelled H for 'helper'. This gate has a small tip which reaches in between the QPC tips. This gate can be used to help the formation of the tunnel barrier in whichever way is necessary for the particular junction. If the barrier can already be formed to give good quality spectroscopy by just using the C gates, then the H gate can be kept at 0 V. Otherwise, it can be set to a negative voltage to help pinch off, or at a slightly positive voltage to open up the junction.

*To the scientist there is the joy in pursuing truth which
nearly counteracts the depressing revelations of truth.*

H. P. Lovecraft

3

Extended states in 2DEG structures: local measurement

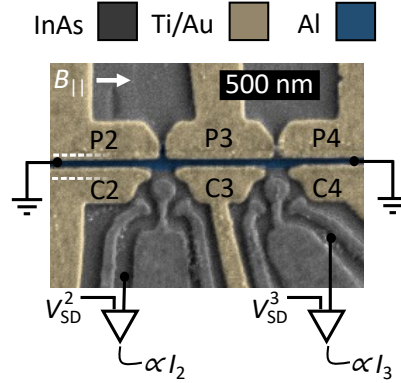


Figure 3.1: False-color electron micrograph of a device which is by design identical to device 1. A proximitized quasi-one-dimensional NW is formed in the InAs quantum well (gray) under the strip of superconducting Al (blue) by lateral electrostatic confinement from the gates labelled P and C (gold). Tunnel barriers to normal leads are formed by the tips of the C gates and allow for measurements of the tunneling currents I_2, I_3 into the NW. The other gates, seen in the image but not colored gold, are not energized in this chapter.

IN THIS CHAPTER, we will cover a spectrum of measurements which were performed using local and nonlocal tunneling spectroscopy, in our proximitized 2DEG structure-based devices. The over-arching theme of the particular devices which will be presented and explored is the possibility of measuring simultaneously on the two ends of a hybrid NW segment. The extra information which is ‘won’ in this way allows us to dispel some of the ambiguities that come usually with tunneling spectroscopy measurements. Is a bound state in fact extended over the length of a pre-defined segment, as desired by the designer of the gate structure, or is it heavily localized in an accidental potential well on one end of the NW? There are various ways to address these questions, some of which are discussed later in this thesis, but measuring on two ends instead of one is a start.

3.1 LOCAL SPECTROSCOPY

First, let me introduce the device design (device 1) on which the measurements in the first half of this chapter were performed. A false-color SEM image of a device which is identical (by design) to this device is shown in Fig. 3.1.

At the heart of the device is a thin Al strip, made by wet etching the epitaxial Al around it (as described in section 2.2). This strip expands into large ground planes at both ends, which are grounded. The chip is then covered by a global layer of HfO_2 dielectric, followed by the deposition of the gates. The gates which are colored gold in Fig. 3.1 are used to deplete the electron density either side of the Al strip, such that a quasi-1D conducting channel of proximitized 2DEG is formed underneath the Al. The gates labelled P can be additionally adjusted to alter the potential landscape of the device, while the gates that are labelled C are used to form QPC-like tunnel barriers, allowing for tunneling from normal leads into the NW. The normal leads are connected to Basel IV converter pre-amplifiers, which facilitate our differential conductance measurements. Note that those are the purposes of the gates by design; in reality both P and C gates need to be tweaked to achieve the desired density in the proximitized region, and to form a usable tunnel barrier. Note also that there are additional gates shown in Fig. 3.1 which are colored dark grey. These provide an additional capability of the device to form laterally defined quantum dots in the probe regions, which will come into play later in the thesis. During the measurements shown in this chapter, these gates were not energized, and need not be considered for now.

Via tunneling spectroscopy measurements (as described in section 2.3.2), we are able to probe the density of states in the NW locally at the locations of the tunnel barriers. Some

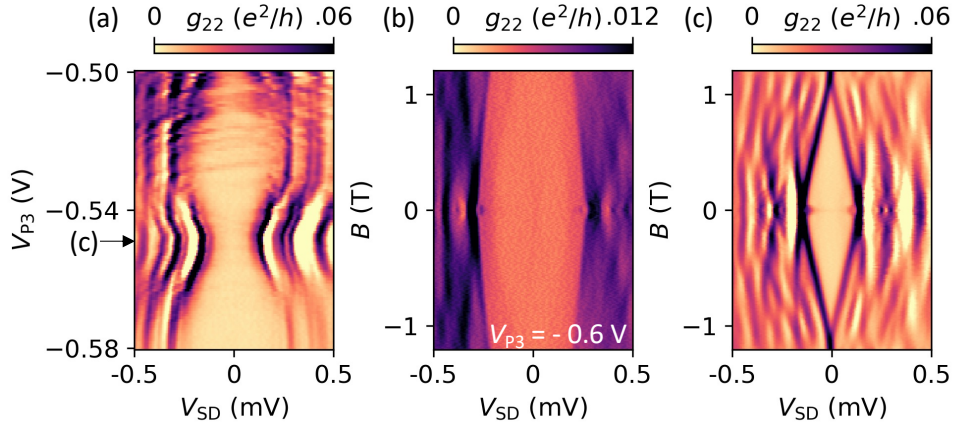


Figure 3.2: Local bias spectroscopy measurements in device 1. (a) Differential conductance as a function of V_{P3} , showing the superconducting gap at zero applied magnetic field and some sub-gap features, including a large resonance around -0.55 V. (b, c) Differential conductance as a function of magnetic field $B_{||}$ parallel to the NW, at $V_{P3} = 0.6$ V and $V_{P3} = 0.55$ V respectively. The gate value for (b) is just below the range of (a), and no sub-gap states are visible. The value for (c) is indicated in (a) with an arrow, and is selected so that the evolution of the bright sub-gap state in field can be observed.

examples of this well-known measurement regime for device 1 are shown in Fig. 3.2, as a function of gate voltage V_{P3} and magnetic field parallel to the NW $B_{||}$ at different fixed gate voltages. These data are measured at the left tunnel barrier shown in Fig. 3.1. In Fig. 3.2 (a), measured at zero applied magnetic field, one can see a superconducting gap $\Delta \sim 290 \mu\text{eV}$, which is modulated by subgap excitations which are tuned by V_{P3} . At more positive voltages these are very close together, and blur the gap, while at more negative voltages (around -0.55 V) one clearer, more slowly evolving (with respect to V_{P3}) resonance is observed. Going more negative still, the gap appears to empty out, with no further subgap states observed. We interpret this as indication that we are indeed using the gate P_3 to deplete the carrier density underneath the NW segment. As we deplete, the remaining carriers are pressed up against the Al, so that only the strongly proximitized density remains, and we see a clean gap. It should be clarified that the 2DEG directly under the NW segment is screened from the

top by the Al, but we are still able to deplete it using the P and C gates because the electric field lines wrap around the sides of the Al strip, so we deplete from the sides. It is not clear whether we ever deplete the 2DEG under the Al fully, as the gates which we use to deplete are also used to tune the tunnel barriers, so eventually we pinch off conductance to the normal lead.

In Fig. 3.2 (b) and (c) one can see the result of applying a magnetic field parallel to the NW, at a gate voltage at which the 2DEG underneath the segment is heavily depleted (b) and at -0.55 V, as marked with the letter (c) in panel (a), where a subgap state comes into the gap and dips down towards zero energy. In (b), the gap closes in field, with some splitting of the gap edge in field visible on the left. In (c), the bound state splits in field. The above gap spectrum in this case is complicated, and the gap edge is not well defined. This bound state was observed on only one probe, and only with local conductance. This limits the information we have about its spatial extent and other properties. We will now delve into the world of double ended measurement, where we have more tools to determine whether a bound state is an extended, nonlocal object inside the NW, or a localized, dot like object situated near the probe region.

3.2 ELECTROSTATICALLY DEFINED BOUND STATES

When we vary the voltage on the P and C gates, the potential layout experienced by the NW changes. Figure 3.3 shows a measurement at zero voltage bias and finite magnetic field applied parallel to the NW, in which the conductance is mapped with respect to all P gates and all C gates on the device. The pattern which is observed is characteristic of our devices; at more positive P gate voltages the resonances which are observed respond more strongly to the P

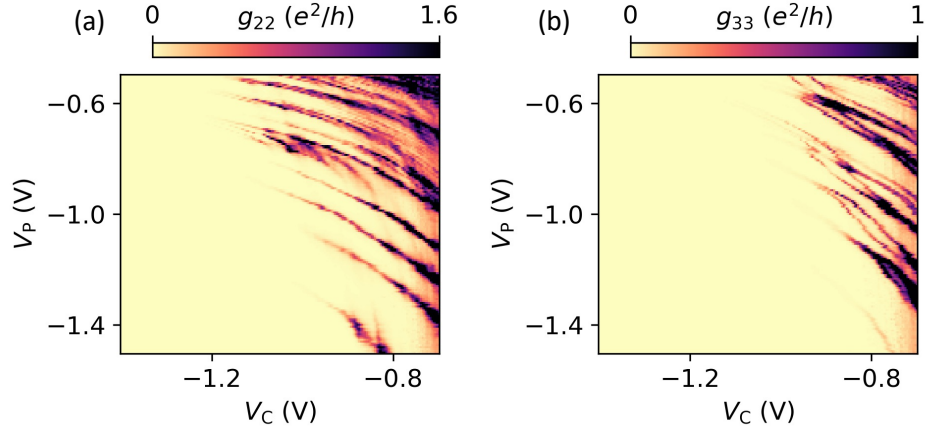


Figure 3.3: Differential conductance measured at $V_{SD}^2 = V_{SD}^3 = 0$ V, at $B_{||} = 1.5$ T, a field where bound states in the NW have already started to come down to zero energy. The conductance is measured with respect to all P gates (V_P) and all C gates (V_C), on the left (a) and right (b) sides of the segment of NW underneath the gate P3.

gates, while at more positive C gate voltages there is a stronger response to the C gates. We propose that this is due to an asymmetry in the spatial distribution of the carrier density, introduced by the asymmetry in gate voltage values. Panels (a) and (b) show simultaneous measurements on the left and right probes of device I, and while the general slopes are similar and follow the pattern described above, there is no particular correlation between specific features measured on the two sides.

The way in which we can attempt to confine bound states which will extend between two probes, showing non-trivially correlated signal on both sides, is to deliberately create a well in the potential along the NW axis. To confine states between our left and right probes, we can create such a potential modulation by setting the voltages on the gates P₃ and C₃ to significantly more positive voltages than their neighbors on the left and right. The distance between the probes here is ~ 600 nm.

Maps taken in such a configuration are shown in Fig. 3.4. V_{P3} and V_{C3} are swept, while

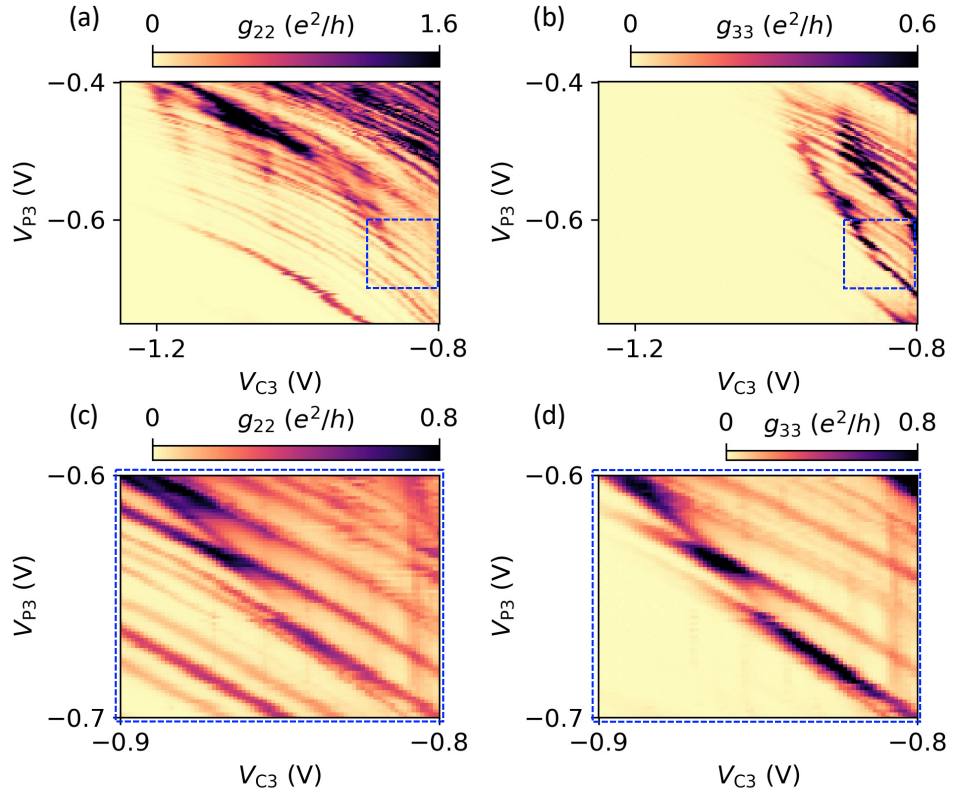


Figure 3.4: Differential conductance measured at $V_{SD}^2 = V_{SD}^3 = 0$ V, at $B_{||} = 1.5$ T. Here the voltages applied to the surrounding gates are significantly more negative than V_{P3} and V_{C3} , and one can observe correlations between the resonances measured on the left (a) and right (b) of the NW segment. These correlations are perhaps more easily resolvable by comparing data taken in a smaller range, with higher resolution (c, d).

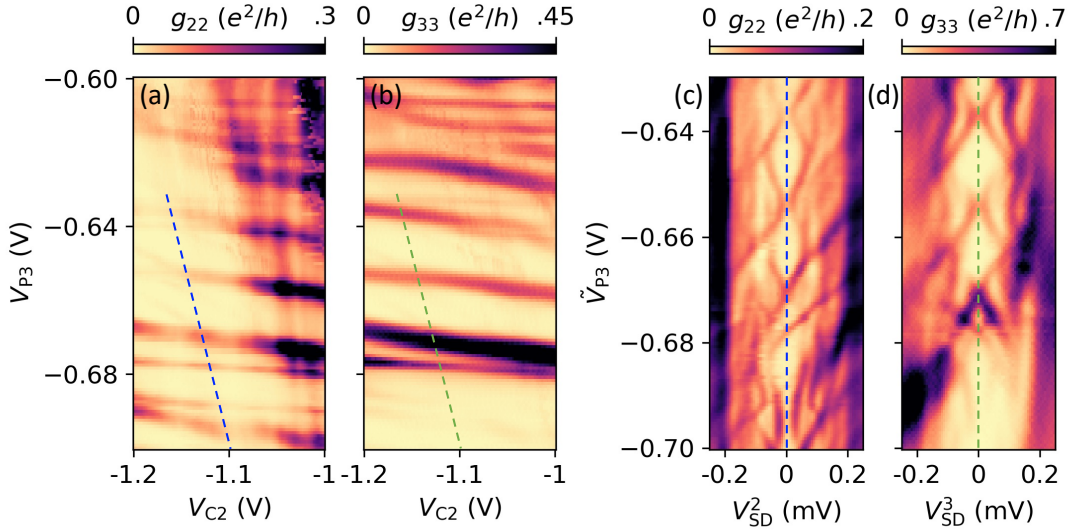


Figure 3.5: (a, b) Differential conductance measured at $V_{SD}^2 = V_{SD}^3 = 0$ V, at $B_{||} = 1.5$ T. The conductance is measured as a function of V_{P3} , which acts as a plunger for the NW segment underneath it, and V_{C2} , which should primarily affect the left tunnel barrier. (c, d) Local spectroscopy measured on both of the tunnel probes, showing what appears to be correlated states as a function of $V_{SD}^{2,3}$ and the compensated parameter as indicated by the blue and green lines in (a) and (b) respectively.

the other P and C gate voltages are fixed at -1.2 V and -1 V, respectively. In the large scale maps on the left and right probes shown in (a) and (b) respectively, there are many resonances which are observed on both sides at the same voltages and with identical voltage dependence. For clarity, maps of part of this gate region with higher resolution are shown in (c), (d). These correlations, which are easily accessed in a wide range of gate space, can be contrasted with the appearance of the resonances in Fig. 3.3 to indicate that creating a potential difference via gating does allow for the creation of bound states in a pre-defined location, and that in these materials 600 nm is a length scale over which correlations can be visible without the need for fine-tuning.

The next step towards checking if the resonances which appear correlated in these maps are indeed due to bound states extending between the probes is by changing the voltage on

a gate which should affect local objects on one probe much more significantly than on the other. In Fig. 3.5 (a, b), this is demonstrated using the gate C_2 . This gate (along with C_3) is used to control the left tunnel barrier, and so should have an effect on the conductance on the left probe. It should also have a very weak lever arm to states which are localized only far away from tunnel barrier 2. Measuring on both probes as a function of V_{P_3} and V_{C_2} , we find resonances which appear at the same gate voltages on both sides, and are strongly tuned by V_{P_3} , but also have an easily distinguishable slope with respect to V_{C_2} . Measuring states with the right probe which have a notable slope with respect to V_{C_2} points towards the states being extended in between the probes. Additionally, some resonances are detected with the left probe which couple very strongly to V_{C_2} so that they are almost vertical. We suppose these to be resonances caused by accidental quantum dots forming in the barrier region on the left.

A compensated parameter \tilde{V}_{P_3} can be defined, so that while V_{P_3} is swept V_{C_2} is adjusted slightly so as to avoid coming on resonance with any such barrier defects, and maintain a constant (to the order of magnitude) high bias conductance. This parameter is marked in Fig. 3.5 by the blue and green solid lines in (a) and (b) respectively (same parameter for both probes, as the measurement is simultaneous). Bias scans along this parameter are shown in panels (c) and (d) for the two probes. While at higher bias the two spectra have some differing features, the low energy states which oscillate around zero energy are the same on both sides.

Another way to look at these states, which we interpret from the above discussion to likely be extended in between the two probes, is thought a ‘phase diagram’-like measurement. This involves sweeping a gate voltage on one axis (in this case V_{P_3}) and the magnetic field $B_{||}$ on the other. Such a measurement is shown in Fig. 3.6, with (a) and (b) showing conductance

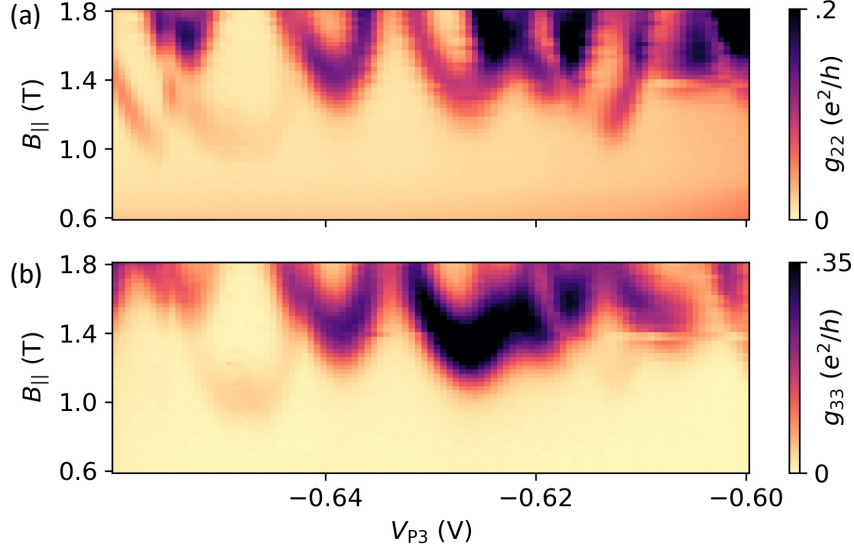


Figure 3.6: Differential conductance measured at $V_{SD}^2 = V_{SD}^3 = 0$ V, at the left (a) and right (b) sides of the NW segment covered by gate P3. Lobes emerge as a function of the compensated gate parameter \tilde{V}_{P3} and $B_{||}$, corresponding to the bound states in the NW reaching zero energy and moving away again as the field ramps up. Clear correlations can be seen between the resonances on both sides.

on the left and right probes respectively. The measurement is taken at zero voltage bias, and the states appear as lobes in the phase diagram, showing a high conductance as they merge at zero energy and then returning to low signal inside the lobe, after the state crosses through zero. In this case, the lobes are clearly correlated, confirming correlation in both gate space and magnetic field in one measurement.

3.3 ILLUSIONS OF EXTENSION

We have considered a measurement flow for tuning up states which extend in a region between two probes, relying on the ability to measure simultaneously on both sides. So far the data presented has passed the extension tests which we have considered. Now, we will take a second to look at a counter-example.

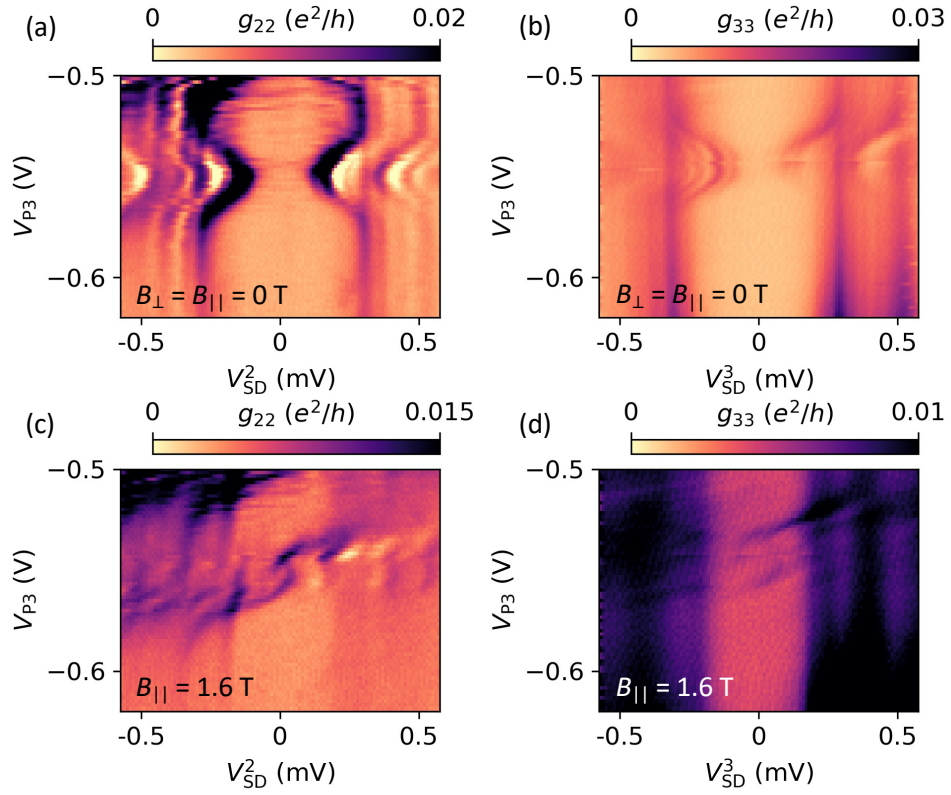


Figure 3.7: Differential conductance measurements on two sides of a NW segment showing resonances which appear at very similar values of V_{p3} , measured at 0 T (a, b) and 1.6 T (c, d). The sub-gap states appear with different signal strength, but are qualitatively similar.

In the same device, with a slightly different gate voltage configuration ($V_{P1-4} = (-1.2 \text{ V}, -1.2 \text{ V}, \text{swept}, -0.82 \text{ V})$, $V_{C1-4} = (-1 \text{ V}, -1.095 \text{ V}, -1.3 \text{ V}, -0.9 \text{ V})$), differential conductance is measured again on both probes and on each one a bound state can be seen coming down into the gap at 0 T applied magnetic field, with an energy minimum at $V_{P3} \sim -0.55 \text{ V}$ (Fig. 3.7 (a, b)). At $B_{\parallel} = 1.6 \text{ T}$ (Fig. 3.7 (c, d)), the bound states have both evolved in field, and now cross twice through zero energy forming what looks to be a singlet to doublet transition⁴⁴. At both zero and finite field the behavior of the states as a function of V_{P3} is similar, and their energy minima (in the zero field case) and zero crossing points (in the finite field case) coincide. There looks to be good correlation between the two sides, which one might interpret as evidence of this being one extended state, measured from two sides. However, if we perform one of the checks described above, we find evidence to the contrary. In Fig. 3.8 (a, b) maps are shown of differential conductance at zero voltage bias, and a magnetic field B_{\parallel} of 1.5 T. We measure as a function of V_{P3} , which (as seen in Fig. 3.7) tunes the bound states which we are interested in, and V_{C4} , which tunes the tunnel barrier on the right side but not the left. In contrast to the matching slopes we saw in Fig. 3.5, here the resonances measured with the two probes respond very differently to the gating. On the right (panel (b)), two resonances are observed, corresponding to the two crossings of the bound state through zero energy, which respond to both gates P3 and C4. On the left, however, the two resonances are totally horizontal, responding only to P3. This test demonstrates that the resonances measured with the two probes originate from two different states, which can be fine-tuned to appear correlated in bias scans by selecting a certain V_{C4} . Similarly, panels (c) and (d) show the same test but utilizing V_{C2} , which tunes only the barrier on the left. In this case the resonances on the left respond to V_{C2} , while the ones on the right couple only

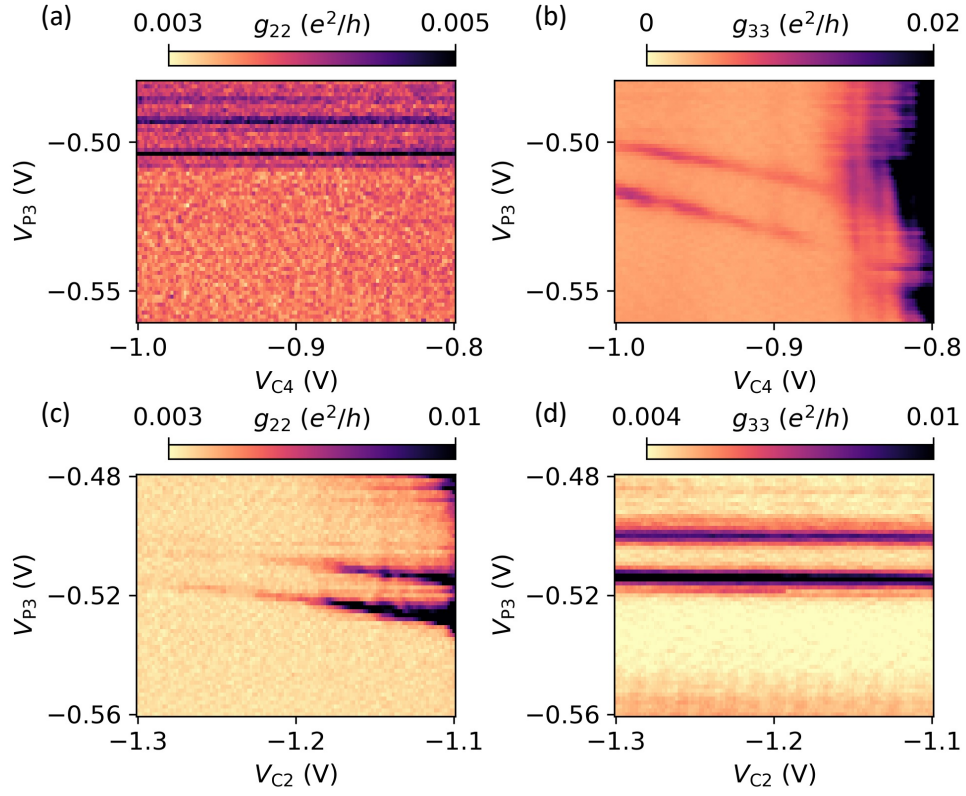


Figure 3.8: (a, b) Differential conductance measurements at zero voltage bias on two sides of the NW segment, at $B_{||} = 1.5$ T, taken with respect to V_{P3} which acts as a NW plunger, and V_{C4} which should primarily affect the right tunnel barrier. Only the resonances measured on the right side of the NW respond to V_{C4} , suggesting that no extended bound states are being observed. (c, d) A similar measurement, this time using V_{C2} instead of V_{C4} .

to V_{P3} .

Cats have no sense of humor, they have terribly inflated egos, and they are very touchy.

Robert A. Heinlein

4

Nonlocal conductance spectroscopy of Andreev bound states

This chapter is a modified and supplemented version of the data and text presented in the following manuscript:

Nonlocal conductance spectroscopy of Andreev bound states in gate-defined InAs/Al nanowires, by Andreas Pöschl, *Alisa Danilenko*, Deividas Sabonis, Kaur Kristjuhan, Tyler Lindemann, Candice Thomas, Michael J. Manfra, and Charles M. Marcus.

4.1 INTRODUCTION

To provide a more complete description of the extended states we have studied in the previous section, we turn to a different (and complementary) kind of transport measurement. We already saw how tunneling spectroscopy, enabled by Andreev reflections, allows us access to the density of states locally at our probe locations. The geometry which we will discuss here was realized recently^{64,65}, and necessarily consists of two leads which are both connected to the same grounded, proximitized NW. This setup allows for the measurement of nonlocal tunneling current, which flows from one normal lead to the other. This current is driven by two processes: transmission, where a particle enters through one lead and leaves through the other, and crossed Andreev reflection, where a particle enters through one lead and then a hole leaves via the other lead, with a Cooper pair being given to the superconducting condensate⁶⁷⁻⁶⁹. We can take a differential measurement of this current, obtaining the nonlocal conductance. Since the transport mechanisms which lead to the nonlocal signal are mediated by bound states in the NW which connect the two leads, nonlocal conductance measurements are useful for probing properties of ABS that are not directly accessible via local spectroscopy. Local spectroscopy provides local information about the DOS, but nonlocal measurements can help to characterize the bulk of the proximitized NW. Importantly,

theoretical studies predict that a characteristic signature in the nonlocal conductance signal indicates a topological phase transition in Rashba NWs^{68,70-74}. The closing of the induced gap measured in nonlocal conductance at finite magnetic fields has been observed⁶⁵, though not a re-opening. The same underlying transport processes have been used to demonstrate Cooper pair splitting in quantum dots coupled to a superconducting lead and two normal leads⁷⁵⁻⁷⁸, and nonlocal spectroscopy of subgap states induced by the quantum dot states has been performed in similar devices^{77,79}.

In this section, we will look at nonlocal conductance measurements performed on the same device which in the previous section we characterized with local spectroscopy (device 1), and observe the effect of magnetic field rotation on the extended subgap states. We will then take a look at a similar device, in which the effect of magnetic field and gate voltage on ABSs will be discussed, and symmetry relations⁶⁴ will be used to access information regarding the BCS charge of the ABSs

4.2 NONLOCAL CONDUCTANCE MEASUREMENT

To complete the snapshot of extended states in device 1, we return to the gate configuration used in section 3.2 and make use of a complementary measurement - that of nonlocal conductance. Here, as well as applying a voltage excitation to a normal lead and measuring the local current into the device, the nonlocal tunneling current flowing from one normal lead to the other is also detected. This current consists of QPs that are transmitted or crossed Andreev reflected, and a differential measurement of it yields the nonlocal conductance.

As we have done for the local conductance measurements, individual current to voltage converters are connected to the two probes, allowing the currents I_2 and I_3 into the two leads

to be measured as a function of the bias voltages V_{SD}^2 and V_{SD}^3 . Then, using standard lockin techniques, the local conductance $g_{22} = \frac{dI_2}{dV_2}$ is measured as before. In addition, the nonlocal conductance $g_{23} = \frac{dI_2}{dV_3}$ is also recorded, detecting the nonlocal current flowing from probe 3 to probe 2. Analogously, g_{33} and g_{32} are also recorded. The setup is described in more detail in section 2.3.3.

A measurement of the four conductances as described above is shown in Fig. 4.1. Both of the nonlocal conductances (g_{23} and g_{32} , shown in panels (b) and (c)) show a signal of $\sim |0.04| e^2/h$. This is around one order of magnitude lower than the signal strength in the local conductance measurements (panels (a) and (d)). Numerical simulations performed for NWs of comparable length scales suggest that this order of magnitude difference is indicative of low to intermediate disorder⁷².

In the g_{23} measurement, the regions of strong nonlocal conductance are bound at higher bias by an envelope which we interpret as the parent gap of the proximitizing Al, which closes in applied parallel field B_{\parallel} . This effect is less clear in the g_{32} measurement, which suffers from a higher noise level.

The ABSs are visible in both local and nonlocal conductances, evolving in field in the same way on both probes. At magnetic fields below the zero energy crossing of the ABSs, the nonlocal signal below the energy of the lowest lying ABS is vanishingly small. These lowest lying ABSs are the ones which we interpret as extending underneath the entire 600 nm segment, from probe to probe, and their energy sets the size of the induced gap Δ_{ind} of the proximitized system. For NWs longer than the coherence length of the parent superconductor, such a suppression in nonlocal signal strength is expected from theory for $eV_{\text{SD}} < \Delta_{\text{ind}}$ ⁶⁸. When the bias voltage is between the parent gap and the induced gap, nonlocal conductance signal is

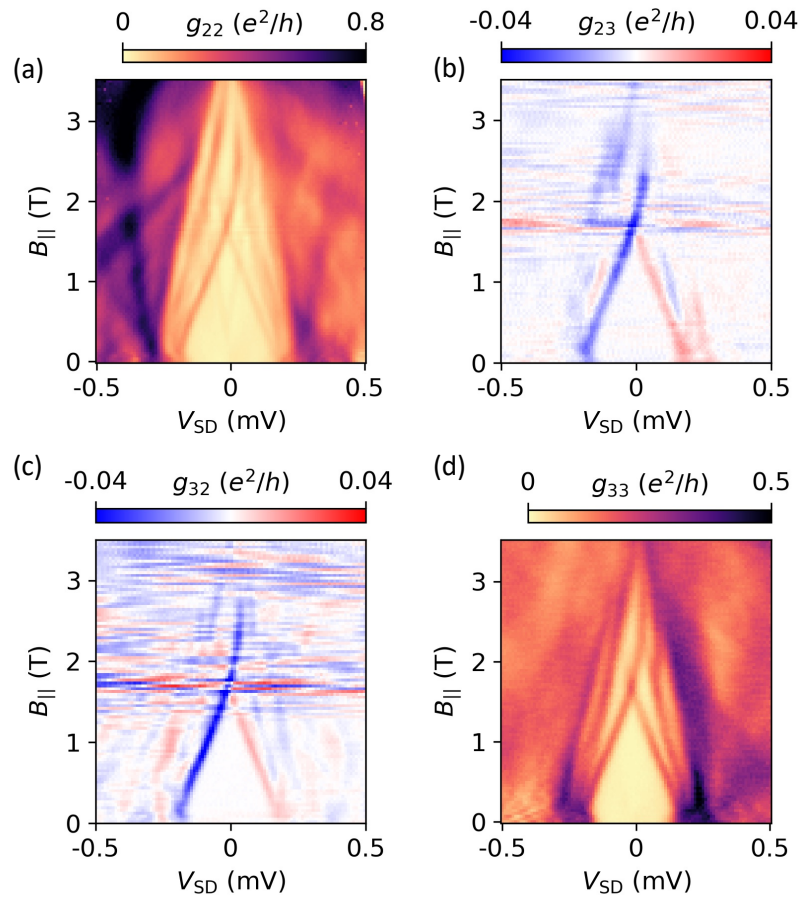


Figure 4.1: Measurement of the two local (a, d) and two nonlocal (b, c) conductances as a function of V_{SD} and magnetic field $B_{||}$ at $V_{P3} = -0.68$ V. The local conductances reveal sub-gap states that cross through zero bias at around 1.6 T. These sub-gap states also appear in the nonlocal conductances.

finite. This can be interpreted as being due to quasiparticle transport through higher excited states in the system.

4.3 MAGNETIC FIELD ROTATIONS

Having set up the system to measure local and nonlocal conductances, and tuned up to a regime with states extending between two probes, we can perform measurements to investigate the effect of the angle of the applied magnetic field. To do this, we apply a radial field with some magnitude r and then rotate the field by changing the angle φ . We define $\varphi = 0^\circ$ as pointing in the plane of the 2DEG, perpendicular to the axis of the NW, and $\varphi = 90^\circ$ as pointing out of the plane of the 2DEG.

Local and nonlocal conductances measured for such field rotations are shown in Figs. 4.2, 4.3, and 4.4 for radial fields of 0.1 T, 0.2 T and 0.4 T respectively. As expected, the parent gap is maximal at $\varphi = 0^\circ$ and $\pm 180^\circ$, where the field is in the plane of the superconducting film, and minimal at 90° where the field points perpendicular to it, threading maximal flux through the area of the thin film. For the two lower field values this leads to a minimization of the gap, while in Fig. 4.4 the gap fully closes and re-opens. The bound states, which appear with the same angle dependence on both probes and in all four conductances, appear to oscillate out of phase with the gap oscillation. Interestingly, it appears that the phase difference is not 90° , but something like 80° . Similar measurements have been theoretically discussed in the context of measuring the direction of the SO field, and the ratio of Rashba to Dresselhaus spin orbit coupling⁸⁰. For this purpose, rotations in the plane of the wire would be more informative. While such measurements have not been taken, this is an avenue which could be pursued using the devices and methods that have been described here.

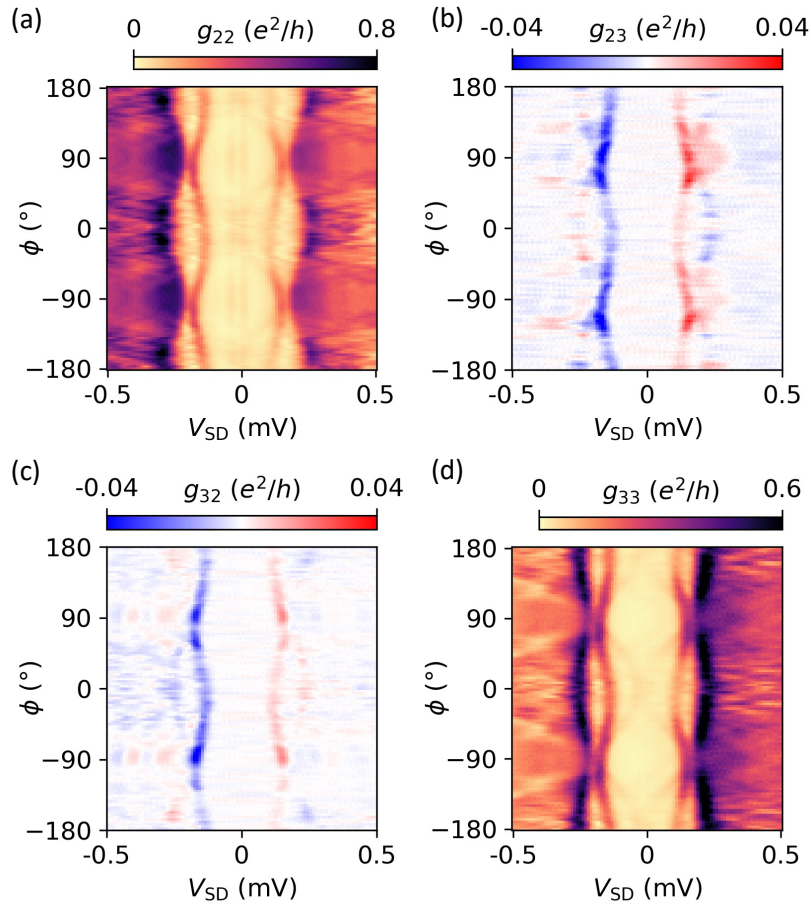


Figure 4.2: Measurement of the four conductances as a function of angle ϕ of magnetic field of radius 0.1 T rotating around the NW axis. Measured with V_{P3} at -0.68 V, so that an extended sub-gap state is observed during the rotation. The gap size is modulated with angle, but the gap remains open throughout the measurement.

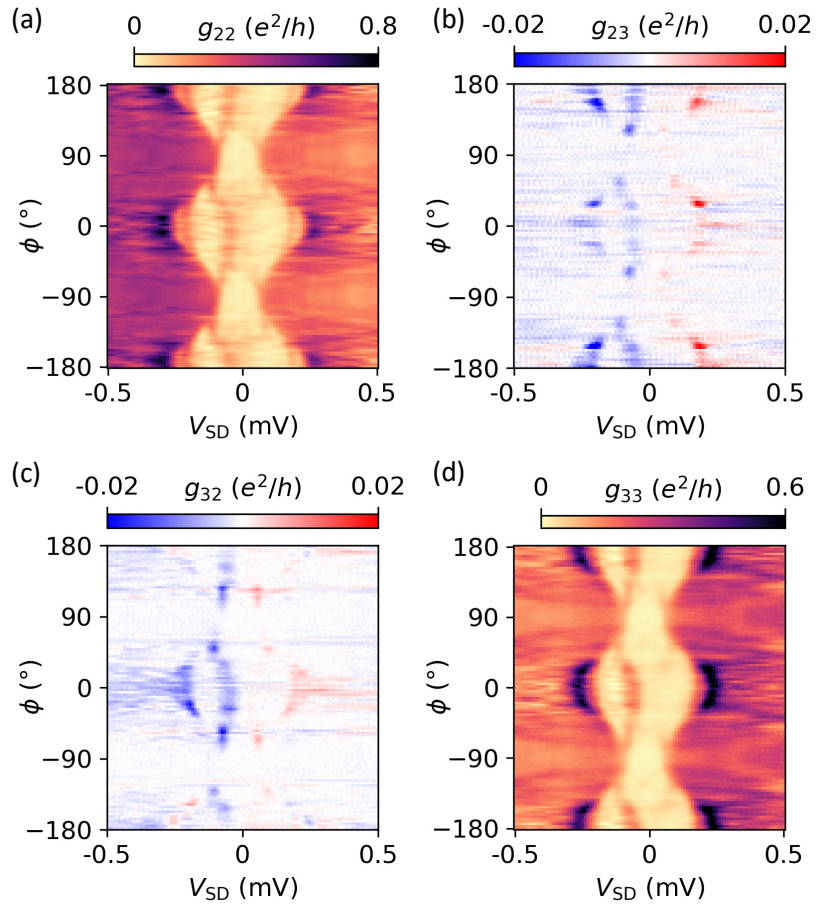


Figure 4.3: Measurement of the four conductances as a function of angle ϕ of magnetic field of radius 0.2 T rotating around the NW axis. Measured with V_{P3} at -0.68 V, so that an extended sub-gap state is observed during the rotation. The gap size is modulated with angle, and the sub-gap state approaches zero energy near 0° and $\pm 180^\circ$.

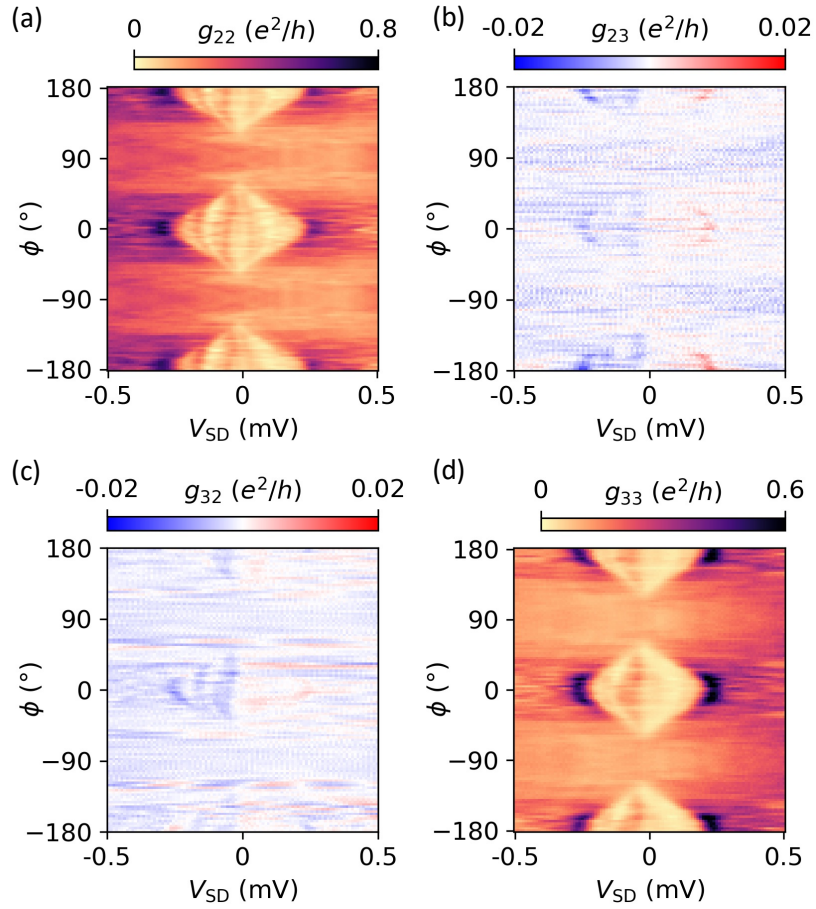


Figure 4.4: Measurement of the four conductances as a function of angle ϕ of magnetic field of radius 0.4 T rotating around the NW axis. Measured with V_{P3} at -0.68 V, so that an extended sub-gap state is observed during the rotation. At this field value, the gap closes and re-opens as a function of ϕ .

4.4 NONLOCAL ANALYSIS AND BCS CHARGE EXTRACTION

In the previous sections, we demonstrated the technique of nonlocal conductance, combined with a range of checks of the extension of ABSs. In this section, another device configuration is presented, and a more theoretical analysis is introduced, allowing the charge character of bound states to be inferred from nonlocal conductance measurements. ABSs are found to oscillate around zero as a function of gate voltage, with modifications of their charge consistent with theoretical expectations for the total Bardeen-Cooper-Schrieffer (BCS) charge of ABSs. **This part of the chapter closely follows the manuscript.**

Device 3 is shown in Fig. 4.5. It consists of a superconducting strip of Al on top of a shallow 2DEG formed in an InAs quantum well. Two superconducting probes made from Al were defined 50 nm away from the superconducting strip. Gates made from Ti/Au are separated by HfO_x gate dielectric from the superconductor and semiconductor underneath. The gates labeled W_L , W_M , and W_R cover different segments of the Al strip and electrostatically confine a quasi one-dimensional NW in the semiconductor. The gate T_L (T_R) depletes the semiconductor between left (right) probe and NW forming a tunnel barrier. The ends of the superconducting strip were connected to electrically grounded planes of superconducting Al. The main differences to the device shown in the previous sections are that the leads are superconducting, and the W gates are continuous over the Al NW, instead of splitting into P and C gates. Additionally, there are no extra gates for quantum dot definition in this configuration.

Connecting individual current-to-voltage converters to the two probes allows for the measurement of the currents I_L and I_R running into the two leads as a function of the source drain

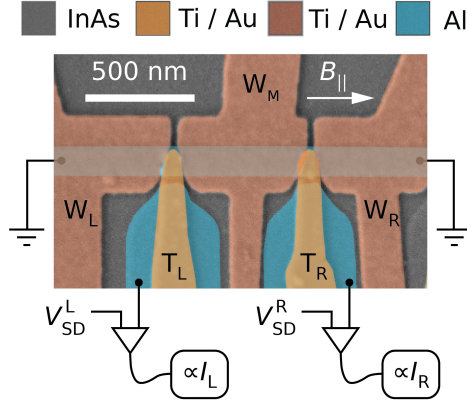


Figure 4.5: False-color scanning electron micrograph of device 3. A proximitized quasi one-dimensional NW is formed in the InAs quantum well (gray) under the strip of superconducting Al (blue) by lateral electrostatic confinement from the gates W_L , W_M , and W_R (red). Leads made from Al are separated from the NW by small regions which are gated by T_L and T_R (orange) to form tunnel barriers, and allow for measurements of the tunneling currents I_L , I_R into the NW.

bias voltages V_{SD}^L and V_{SD}^R . Note that positive current direction is defined as current running from the amplifier towards the device. The lock-in detection technique as described in Ref.⁶⁴ was used to measure the tunneling conductances

$$G_{LL} = dI_L/dV_{SD}^L \quad (4.1)$$

$$G_{LR} = dI_L/dV_{SD}^R \quad (4.2)$$

and G_{RR} , G_{RL} defined analogously.

In order to confine an ABS in the NW, a modulation of the electron density along the elongated NW dimension was created, as previously, using the three gates W_L , W_M , W_R . The gate voltages V_{WL} and V_{WR} were set to -4.50 V. The NW segments underneath the respective gates W_L and W_R have a hard superconducting gap with no subgap states and act as

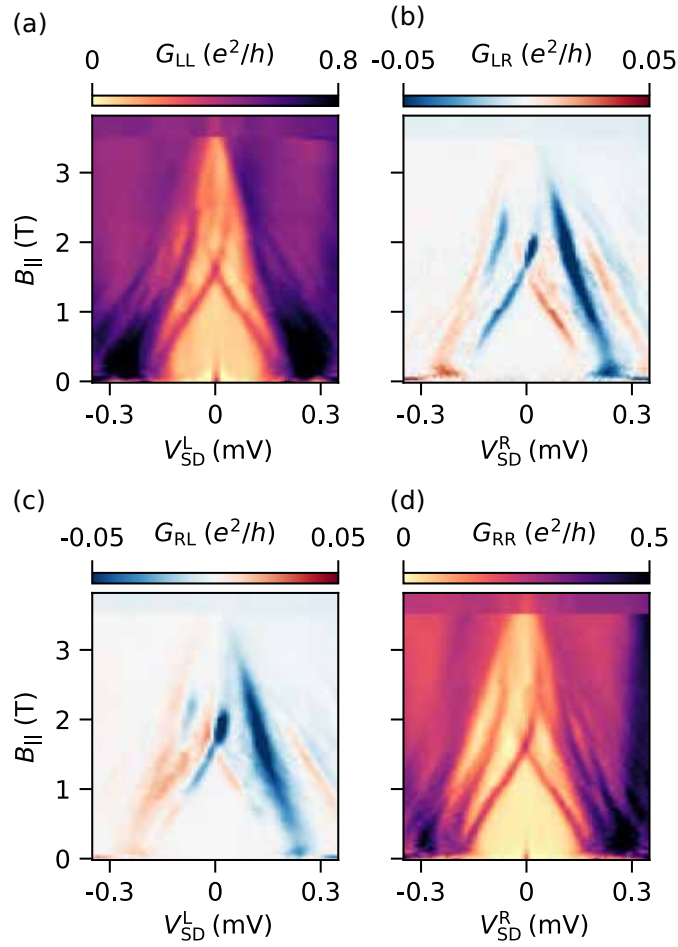


Figure 4.6: Measurement of the four conductances as a function of V_{SD} and magnetic field $B_{||}$ at $V_{WM} = -3.02$ V. Local conductances (a, d) show sub-gap states that cross zero bias at ~ 1.6 T. These sub-gap states are also visible in the nonlocal conductances (b, c).

QP filters between the Al ground planes and the NW segment under the gate W_M ^{81,82}. The gate voltage V_{WM} was set to -3.02 V; significantly more positive than the voltages on the neighboring gates W_L, W_R . A measurement of the four conductances as a function of V_{SD} and magnetic field $B_{||}$ is depicted in Fig. 4.6. Note that the superconducting probes serve as normal leads for magnetic field values $B_{||} > 0.2$ T⁶⁶. Both local tunneling conductances G_{LL}, G_{RR} reveal subgap resonances which emerge at low magnetic fields from the QP continuum at high bias, and cross zero voltage bias at parallel magnetic field $B_{||} = 1.6$ T. The resonances can be attributed to an extended ABS in the $0.6 \mu\text{m}$ long NW segment under the gate W_M due to the appearance in both local tunneling conductances with identical dependence on magnetic field and gate voltage V_{WM} , which will be discussed in the following. Hybridization with an accidental quantum dot resonance localized in one of the tunnel barriers was furthermore employed to ensure that we are measuring an extended ABS⁸³; see next chapter for more details.

Both nonlocal conductances G_{LR} and G_{RL} show sizeable conductance $\approx 5 \cdot 10^{-2} e^2/h$. The absolute value is one order of magnitude smaller than the local conductances, similar to the previous nonlocal measurement discussed. The regions of strong nonlocal conductance in both $G_{LR}, G_{RL} \geq 25 \cdot 10^{-3} e^2/h$ are bound at high bias values by an envelope. This boundary can be interpreted as the gap $\Delta(B_{||})$ of the parent superconductor that proximitizes the semiconductor and closes with applied magnetic field. For magnetic fields below the zero crossing of the ABSs, there is again a region of vanishing nonlocal conductance around zero bias which extends to the $V_{SD}^{L/R}$ values which mark the ABS energy. The ABSs are the lowest lying excited states that extend over the whole NW under the gate W_M . Their energy therefore sets the size of the energy gap Δ_{ind} that is induced in the semiconductor by proximity effect

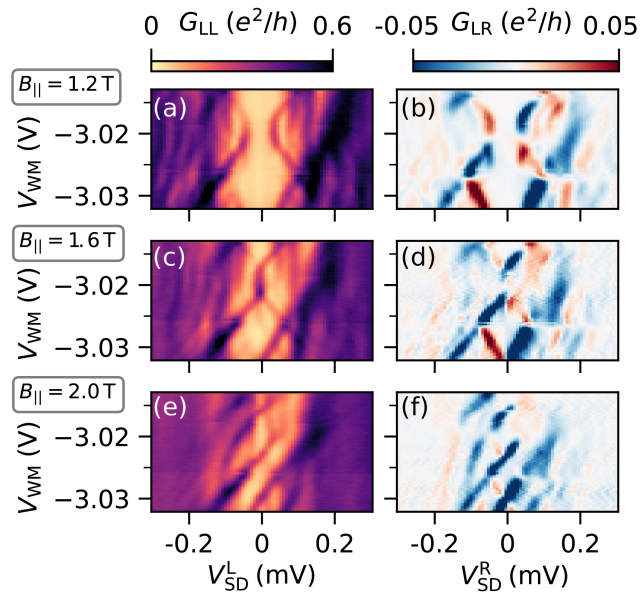


Figure 4.7: Local conductance G_{LL} and nonlocal conductance G_{LR} as a function of V_{WM} at three values of parallel magnetic field $B_{||}$. (a) Subgap states appear as lobes inside the superconducting gap. (b) The lowest excited state appears in the nonlocal conductance; a spectrum of excited states is also visible. (c) At $B_{||} = 1.6$ T the lowest energy states come down to zero energy, where nonlocal conductance is suppressed (d). (e) At $B_{||} = 2$ T the ABSs intersect forming a low energy state which oscillates around zero bias. (f) The nonlocal conductance changes sign at the turning points of the low energy state.

and Zeeman energy. Exponentially suppressed nonlocal conductance is therefore expected for $eV_{SD}^{L/R} < \Delta_{\text{ind}}$ for NWs that are longer than the coherence length of the parent superconductor⁶⁸. In the voltage range $\Delta_{\text{ind}} < eV_{SD} \leq \Delta$ there is finite nonlocal conductance that can be interpreted as QP transport through higher excited states.

At a magnetic field of $B_{\parallel} = 1.2$ T, the ABSs trace out a pair of lobes which do not reach zero bias as a function of gate voltage V_{WM} , as seen in the the local conductance G_{LL} [see Fig. 4.7(a)]. The corresponding nonlocal conductance G_{LR} , plotted in Fig. 4.7(b), has its largest value at a value V_{SD}^{R} that tracks the position of the low energy subgap state in G_{LL} . Following this state, the nonlocal conductance changes sign in two cases. The first case is a value V_{WM} at which the ABS reaches a minimum in energy. The second case are points where two ABSs cross, which leads to the energy of the lowest lying state changing its slope abruptly from positive to negative and vice versa. Note that there is a spectrum of additional excited states visible at higher bias values V_{SD}^{R} . We interpret these states as a result of the NW being sufficiently long such that the spacing between excited states is decreased⁸⁴. The absence of a similarly dense spectrum of excited states in nonlocal conductance measurements of proximitized quantum dots⁷⁹ and shorter NWs⁶⁴ is in agreement with this interpretation. At a magnetic field of $B_{\parallel} = 1.6$ T the lowest lying ABSs merge at zero voltage bias for a small interval of V_{WM} as seen from the local conductance in Fig. 4.7(c). Within this range, the nonlocal conductance through the ABS is smaller compared to V_{WM} values for which the ABSs are at finite bias voltage [see Fig. 4.7(d)]. This can be understood as a result of the rates for crossed Andreev reflection and QP transmission being equal at this point due to particle-hole symmetry^{67,85}. The nonlocal conductance consequently vanishes because it is proportional to the difference of these two rates^{67,69,86}. At a magnetic field $B_{\parallel} = 2$ T the

ABSs intersect each other, creating a low energy state that oscillates around zero bias, as seen in the measurement of G_{LL} in Fig. 4.7(e). G_{LL} shows an asymmetry with respect to V_{SD}^L . Local tunneling conductances are expected to be symmetric with respect to source-drain bias for the case of two-terminal devices, but for the case of three terminal devices a finite asymmetry is expected. In a linear transport theory, the anti-symmetric part of the conductances $G_{ij}^{\text{anti}}(V_{SD}^j) = [G_{ij}(V_{SD}^j) - G_{ij}(-V_{SD}^j)]/2$ with $i, j \in \{L, R\}$ fulfil the relations

$$G_{ij}^{\text{anti}}(V_{SD}^j) = -G_{ji}^{\text{anti}}(V_{SD}^i) \quad (4.3)$$

at subgap voltages $eV_{SD} < \Delta$ as a consequence of particle-hole symmetry and current conservation^{64,70}. We find that these relations are quantitatively fulfilled for the lowest excited state, while they are violated for higher excited states. Consequently, the sum over all conductance matrix elements $G_{\text{sum}} = \sum_{i,j} G_{ij}$ is symmetric up to the source-drain bias voltages of the lowest energy state. A detailed analysis can be found in the supplementary material (SM) of⁸⁷. Possible reasons for deviations from the symmetry relations were given in⁶⁴. In addition, numerical studies have shown that an energy dependence of the tunnel barriers in a nonlinear transport theory can give rise to violations of the symmetry relations⁸⁸.

The quantity

$$Q_j = \text{sign}(V_{SD}^j) \left. \frac{G_{ij}^{\text{sym}}(V_{SD}^j)}{G_{ij}^{\text{anti}}(V_{SD}^j)} \right|_{E=eV_{SD}^j} \quad (4.4)$$

of a subgap state at energy $E = eV_{SD}^j$ can be extracted from the anti-symmetric and symmetric components of the measured nonlocal conductance $G_{ij}(V_{SD}^j)$ ⁶⁴. The symmetric and anti-symmetric components of the nonlocal conductance G_{LR} measured at a magnetic field value

$B_{||} = 2$ T are plotted as a function of source-drain voltage in Figs. 4.8(a, b). The values stemming from the low energy state were extracted along the positions given by the green lines in Figs. 4.8(c, d). The extracted values of the (anti-)symmetric part of G_{LR} (G_{RL}) are shown in Figs. 4.8(c, d) with a solid green (dotted black) line. These values correspond to the conductance values which enter Eq. 4.4. The (anti-)symmetric components $G_{LR}^{\text{sym(anti)}}$ and $G_{RL}^{\text{sym(anti)}}$ are approximately equal. The resulting values for Q_L and Q_R according to Eq. 4.4 are shown in Fig. 4.8(e). Q_L closely follows Q_R .

Theory suggests that Q_j is proportional to the local BCS charge of the bound state at the position j of the conductance probe^{64,70,89}. Here we found that the local charge character on the left and the right are approximately equal $Q_L \approx Q_R$. For device 3 and $B_{||} = 2$ T, there are extended plateaus $Q_j \approx +1$ ($Q_j \approx -1$) indicative of a state which is locally fully electron (hole) like. Regions of constant positive (negative) Q_j coincide with ranges in V_{WM} where the state energy has a positive (negative) slope with respect to V_{WM} . Abrupt changes in Q_j appear at crossing points of states at finite and zero source-drain bias. This is in agreement with the interpretation of Q_j measuring the local charge of the bound state. For lower magnetic field values, at which the ABSs appear as parabolic lobes without zero energy crossings, a continuous change of Q_j from -1 to 1 is found at the point of minimal ABS energy [See SM Fig.S6 in⁸⁷]. For another device, the same behavior of $Q_L \approx Q_R$ is found with either abrupt changes or continuous crossover from positive to negative Q_j .

The total, integrated charge Q of a bound state at energy E is proportional to dE/dV_{WM} ⁷⁰. Integrating the function $Q(V_{WM})$ should therefore recover the energy of the subgap state as

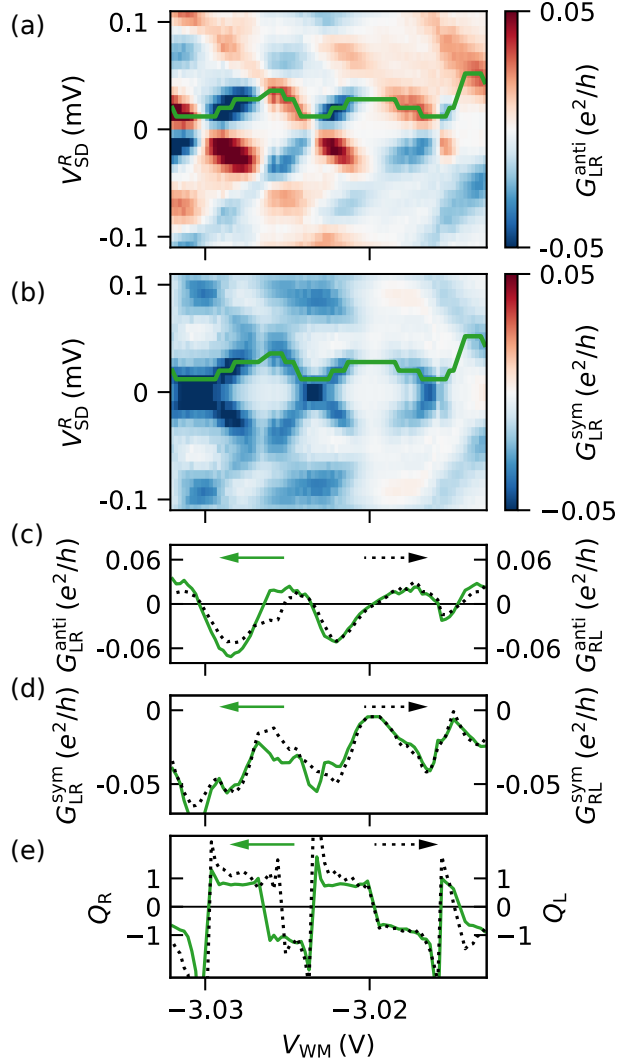


Figure 4.8: (a) Anti-symmetric and (b) symmetric components of the nonlocal conductance G_{LR} measured at $B_{||} = 2$ T. (c) Anti-symmetric and (b) symmetric values of the nonlocal conductances G_{LR} , G_{RL} extracted at the position of the lowest lying state, as marked by the green lines in (a, b). (e) Resulting values extracted for Q_L and Q_R are approximately equal, and appear to oscillate between +1 and -1. Positive (negative) values of Q_i coincide with regions of positive (negative) slope of the state energy as a function of V_{WM} .

a function of V_{WM} . From the experimentally determined Q_j the Energies

$$E_j^{\text{inf}} = a \int Q_j dV_{\text{WM}} + bV_{\text{WM}} + c. \quad (4.5)$$

can be inferred, which is the numerical integrated value of Q_j after re-scaling by a lever arm a and taking into account a linear background b and integration constant c . We find that the resulting curves for $E_{L,R}^{\text{inf}}(V_{\text{WM}})$ match the energy evolution $E(V_{\text{WM}})$ of the low energy subgap state over an extended range of V_{WM} (see SM Fig.S7⁸⁷). This suggests that the experimentally determined Q_j not only reflects the local charge character of the ABS, but serves as measure for the total charge Q of the bound states. Deviations from this behavior are expected for longer devices where the QP charge can vary along the spatial extent of bound states^{70,89}.

4.5 CONCLUSION

In summary, we have performed local and nonlocal conductance spectroscopy of ABSs in a 2DEG based NW as a function of V_{SD} and magnetic field B_{\parallel} and gate voltage V_{WM} . The predicted symmetry relations between the anti-symmetric components of local and nonlocal conductances are fulfilled for the lowest excited state. In addition, we find a dense spectrum of excited states that give rise to nonlocal conductance. For the lowest excited state, the extracted charge character is the same at both NW ends. This is similar to previous studies⁶⁴ despite a longer NW being used here. At high magnetic fields the charge character $Q_{L,R}$ of the low energy state alternates between fully electron and hole like. The oscillations in the charge character $Q_{L,R}$ are found to be in agreement with the energy evolution $E(V_{\text{WM}})$ of the subgap state which suggests that Q_j reflects the total charge of the ABS measured.

The most exciting phrase to hear in science, the one that heralds new discoveries, is not 'Eureka!' (I found it!) but 'That's funny....'

Isaac Asimov

5

Hybridization between Andreev bound states and quantum dots

This chapter is a modified version of the data and text presented in the following manuscript:
Nonlocal signatures of hybridization between quantum dot and Andreev bound states,
by Andreas Pöschl, *Alisa Danilenko*, Deividas Sabonis, Kaur Kristjuhan, Tyler Lindemann,
Candice Thomas, Michael J. Manfra, and Charles M. Marcus

IN THIS CHAPTER, we make use of the imperfections of our tunnel barriers - quantum dots which form accidentally - to probe the nonlocality of the ABSs in the system.

5.1 INTRODUCTION

Progress in material growth has enabled the realization of hybrid materials with distinct low-temperature phases^{4,90-92} not observed in the constituent bulk materials^{29,93-98}. An important example is a superconductor grown epitaxially on a semiconductor having gateable carrier density, large negative g -factor, and strong spin-orbit coupling^{99,100}. A promising material platform that allows for scalable fabrication of advanced devices in this context are InAs two-dimensional electron gases (2DEGs) proximitized by superconducting Al^{5,45,66,101-104}. Devices of suitable geometries allow exploration of various bound states in nanowires (NWs), including Yu-Shiba-Rusinov states, Andreev bound states (ABSs), and Majorana bound states^{45,103,105-110}.

The use of semiconductor-superconductor hybrids facilitates the realization of electrostatically controlled quantum dots (QDs) coupled to superconductors. This was an enabling factor for experiments demonstrating Cooper pair splitting⁷⁶. QDs coupled to ABSs have received considerable attention from theoretical studies, including the use of the QD as a tool for measuring bound state lifetimes¹¹¹ or providing Majorana parity readout^{104,111-115}. In particular, tunnel coupling can lead to energy level hybridization between a QD and a

bound state. This can result in a shift of the bound state energy and an avoided crossing between the subgap resonances stemming from the QD and the ABSs. ABSs at finite energy are pushed towards zero energy when resonantly coupled to the QD. This leads to a characteristic ‘bowtie’ shape in the form of a zero-crossing of the subgap state. For ABSs at zero energy the bound states acquire finite energy when brought on resonance with the QD leading to a ‘diamond’ shaped splitting in energy. The observed pattern of subgap states near the resonance condition depends on the nonlocality and the spin structure of bound states and details of the QD^{116–120}.

In this chapter, we perform tunneling spectroscopy of a NW in the same geometry as was presented in chapter 4, which allows measurements at several side branches along the NW length using electrostatic gates patterned on an InAs/Al hybrid heterostructure. A similar configuration has been investigated theoretically¹²¹, and a related experiment has been carried out in a conventional nanowire with deposited superconductor and normal metallic side contacts¹²². In addition to ABSs due to bound states in the NW, we find conductance resonances due to accidental QDs in the tunnel barriers. We investigate hybridization of QD states with ABSs in the NW, observing signatures of hybridization both locally, that is, at the position of the accidental QD, and nonlocally, measured on another side probe away from the QD.

5.2 EXTENDED STATES AND DOT FORMATION

Figure 5.1(a) shows a micrograph of device 3, based on an InAs 2DEG with 5 nm of epitaxial Al. The device consists of an Al strip of width 100 nm and length 5 μm , connected at both ends to large planes of Al that were electrically grounded. Gates labeled W_{kl} were Ti/Au on

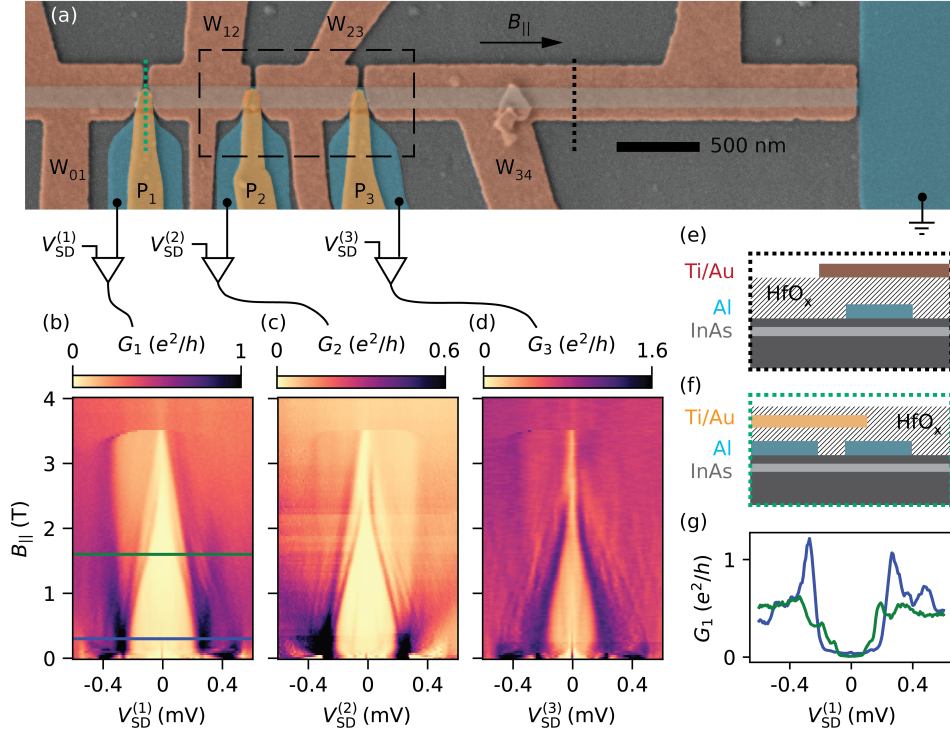


Figure 5.1: (a) False colored scanning electron micrograph of device 3. The device consists of patterned epitaxial Al, forming a long narrow nanowire with several tunnel probes on top of an InAs quantum well. Gates labeled P_j are used to tune the tunnel barrier between the tunnel probe j and the wire ($j \in \{1, 2, 3\}$). Gates labeled W_{kl} with $kl \in \{01, 12, 23, 34\}$ deplete carriers except under the Al. (b-d) Tunneling spectroscopy at three probes with all gate voltages $V_{W_{kl}} = -4.5$ V. (e, f) Schematic cross sections of the device at the positions given by the green and black dotted lines in (a). (g) Line cuts at field values $B_{||} = 0.3$ T and $B_{||} = 1.6$ T indicated by the blue and green line in (b).

top of 30 nm HfO_2 , as shown in Fig. 5.1(e). Gates were used to deplete the semiconductor on either side of the Al wire, creating by depletion a quasi one-dimensional InAs NW self-aligned to the proximitizing Al.

Neighboring gates W_{kl} form a constriction that acts as a tunnel probe. The lead of the probe, away from the tunneling region, is made using the same unetched epitaxial Al. Tunneling across the bare semiconductor region between Al NW and Al lead is controlled by a probe gate, P_j , as shown in Fig. 5.1(f).

The measurement setup is shown schematically in Fig. 5.1(a). With the NW grounded, individual voltage biases $V_{\text{SD}}^{(j)}$ were applied on probe j via current to voltage converters ($j \in \{1, 2, 3\}$). Tunneling currents I_j through the tunnel barriers were measured using lock-in detection yielding differential conductances $G_j = dI_j/dV_{\text{SD}}^{(j)}$. Measurements were carried out in a cryo-free dilution refrigerator with a $6 - 1 - 1$ T vector magnet at ≈ 15 mK mixing-chamber temperature.

Tunneling conductances G_j as a function of magnetic field B_{\parallel} applied parallel to the NW are shown in Figs. 5.1(b-d). For weak tunneling and in the absence of probe resonances, G_j is proportional to the density of states in the NW. The superconducting gap of the Al in the leads of the probes closes at low field, $B_{\parallel} \approx 0.2$ T above which the probes can be regarded as normal metal, as discussed previously^{66,103}. The semiconductor under the Al in the NW was depleted by setting all W_{kl} gates to -4.5 V. Measurements on all three probes showed a superconducting gap closing without any subgap states crossing zero energy. For G_1 this is illustrated by the line cuts in Fig. 5.1(g). A splitting of the continuum of states at high bias due to the Zeeman effect can be seen in G_1 and G_2 . Note that the measurement of G_3 shows finite subgap conductance, which we attribute to probe 3 being tuned to an open regime with high-bias conductance $G_3(V_{\text{SD}}^{(3)} = 0.4 \text{ mV}) \gtrsim 1 e^2/h$.

To investigate the hybridization of a probe QD state with an ABS in the NW, we focus on the $0.6 \mu\text{m}$ long NW segment under gate W_{23} , see dashed box in Fig. 5.1(a), shown in Fig. 5.2(a). To create an ABS in this segment, the voltage on gate W_{23} was set less negative, in the range of -3 V, while voltages on neighboring gates W_{12} and W_{34} were set to -7.0 V. At $B_{\parallel} = 1.6$ T and zero source-drain biases, $V_{\text{SD}}^{(j)} = 0$, conductances G_2 and G_3 were measured as functions of probe-gate voltages V_{p2} and V_{p3} , respectively, and wire-gate voltage

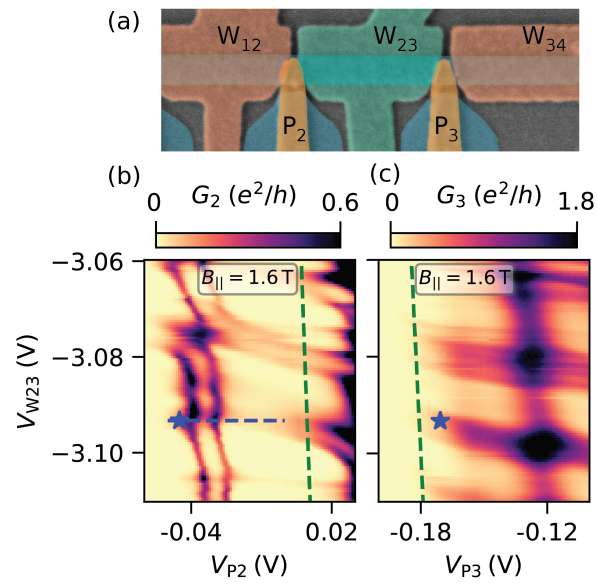


Figure 5.2: (a) Micrograph of the NW segment under investigation. $V_{W_{12}} = V_{W_{34}} = -7.0$ V while the voltage on gate W_{23} (green), is varied. (b), (c) Differential conductance at zero bias measured at the left and the right end of the NW segment. Horizontal conductance resonances appear in both maps at similar gate voltages. Vertical conductance features, strongly dependent on gates V_{P_2} and V_{P_3} which tune the tunnel barriers, are also visible.

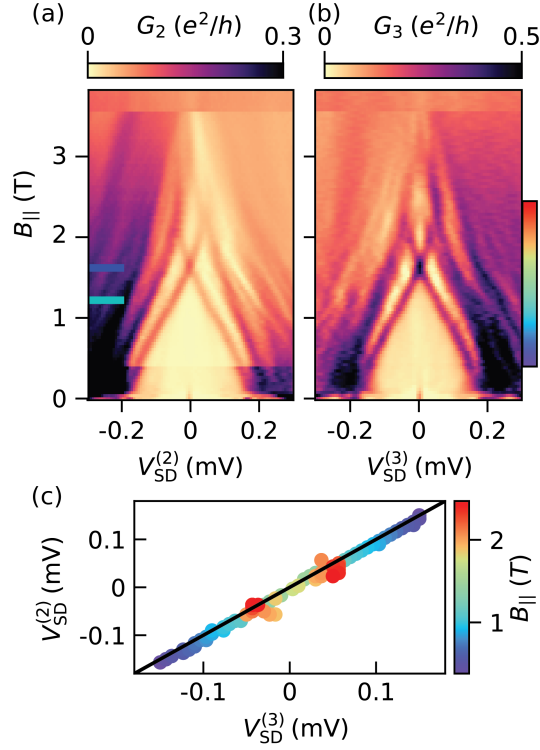


Figure 5.3: (a, b) Tunneling spectroscopy with respect to magnetic field at the two ends of the NW with $V_{W23} = -3.09$ V [marked with \star on Fig. 5.2(b, c)]. Both measurements show subgap states crossing zero bias at $B_{||} = 1.6$ T with a clear overshoot around $B_{||} = 2$ T. (c) Parametric plot of the extracted peak positions from the lowest energy subgap states in (a) and (b). The color of the points indicates the field value in accordance with the rainbow color bar in (b).

V_{W23} . For both tunnel junctions, two sets of conductance resonances can be distinguished in Figs. 5.2(b) and (c) by their characteristic slope. The first set primarily consists of vertical features that are strongly dependent on the gate voltages V_{p2} (V_{p3}), which we attribute to QDs in the tunnel barriers. The second set are predominantly horizontal, depending more strongly on V_{W23} . The latter resonances are visible in both G_2 and G_3 , suggesting that they arise from ABSs that extend over the segment covered by gate W_{23} .

The blue star markers in Figs. 5.2(b, c) at gate voltages $V_{W23} = -3.09$ V, $V_{p2} = -0.045$ V, and $V_{p3} = -0.170$ V mark ABSs that are weakly tunnel coupled to the probes. Tunneling

spectroscopy of these ABSs as a function of magnetic field $B_{||}$ in Figs. 5.3(a, b) reveals a zero-bias crossing of the ABSs at $B_{||} = 1.6$ T followed by an overshoot at $B_{||} = 2$ T. The states appear in both tunneling conductance measurements of G_2 and G_3 . We extracted the peak position in $V_{SD}^{2(3)}$ of the ABS from the measurements of G_2 and G_3 . The parametric plot of the peak positions $V_{SD}^{(2/3)}$ of the ABSs in G_2 and G_3 in Fig. 5.3(c) shows that all points lie close to the identity line, suggesting strong correlations.

The ABSs seen in G_2 and G_3 evolve similarly with gate voltage V_{W23} and magnetic field $B_{||}$, suggesting that they belong to the same extended quantum states. Similar experimental findings have been made previously^{123,124}. The magnetic field dependence of the states is furthermore characteristic for ABSs in short NWs¹¹⁰.

5.3 SIGNATURES OF HYBRIDIZATION, LOCAL AND NONLOCAL

Special points in the measurement in Fig. 5.2(b) are the crossing points of the horizontal resonances with the sharp vertical resonances. At these points, an ABS in the NW is on resonance with the QD in the tunnel barrier under the gate P_2 . Tunneling spectroscopy G_2 using tunnel probe 2 at a field value of $B_{||} = 1.1$ T while sweeping V_{P2} along the values given by the blue dashed line in Fig. 5.2(b) is shown in Fig. 5.4(a). The ABSs at $V_{SD}^{(2)} = \pm 0.05$ mV were unaffected by the change of V_{P2} outside the range between -0.040 and -0.020 V. Within this range, the QD resonance appears as a conductance enhancement at high bias, reflecting the fact that G_2 was being measured through the QD in tunnel barrier 2. As the QD went on resonance with the ABSs, the ABSs with lowest energy merged at zero bias before returning to their previous energies. This resulted in a characteristic ‘bowtie’ shape of the resonances of the ABSs. A simultaneous measurement of G_3 during the sweep of V_{P2} at

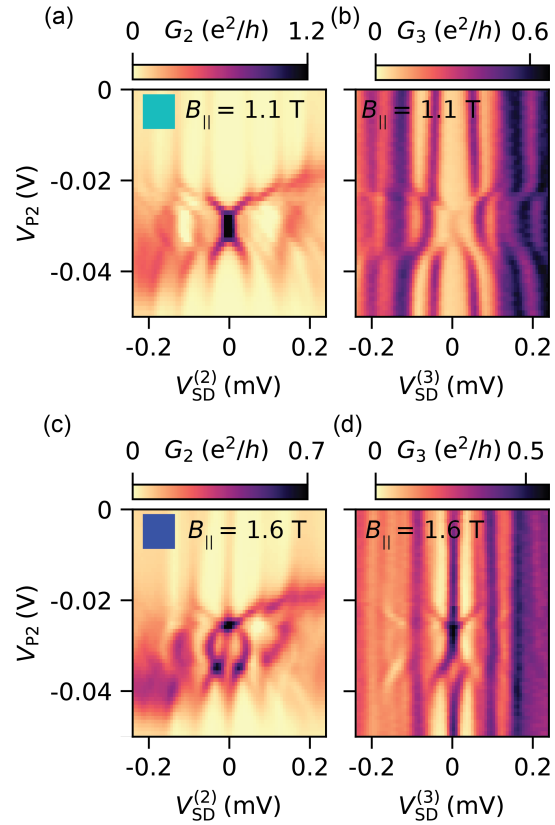


Figure 5.4: (a) Tunneling conductance G_2 at the left side of the NW segment at $V_{W23} = -3.09$ V [marked with \star and blue dashed line on Fig. 5.2(b, c)] as a function of the gate voltage V_{P2} which tunes the tunnel barrier. A QD resonance is visible as an enhancement of conductance at high bias around $V_2 \approx 0.030$ V. The subgap states change their energy at the point of the QD resonance, drawing a characteristic 'bowtie' shape. (b) Tunneling spectroscopy G_3 at the other end of the NW. The ABS show the same change in energy as visible in the measurement of G_2 in (a). (c, d) same as (a, b) at higher parallel magnetic field, $B_{||}$. The ABSs split to form a 'diamond' shaped energy profile at the position of the QD resonance.

the other end of the NW is shown in Fig. 5.4(b). The enhancement of conductance at high bias due to the QD that was present in the measurement of G_2 was absent in the measurement of G_3 . The ABSs, however, showed the same ‘bowtie’ shape around the voltage value $V_{P2} \approx -0.030$ V which corresponds to the resonance condition between the ABSs and the QD in tunnel barrier 2. Note that in the measurement of both G_2 and G_3 not only the lowest energy ABSs undergoes a change at the resonance condition with the QD, but also the higher excited ABSs at $V_{SD}^{(2,3)} = \pm 0.12$ mV and $V_{SD}^{(2,3)} = \pm 0.20$ mV. In addition to the change in ABS energy, a clear change in the conductance peak height is visible when going through the resonance condition.

Around $B_{||} = 1.6$ T, the low-energy ABSs merged to yield a single conductance peak at zero bias. A measurement of G_2 with respect to V_{P2} in Fig. 5.4(c) shows that this peak was unperturbed except for voltage values around $V_{P2} \approx -0.030$ V where the QD was on resonance with the ABSs. At this point, the QD led to a pair of arc-shaped resonances with strong conductance at $V_{SD}^{(2)} \approx \pm 0.05$ mV. Around the same value of gate voltage, the ABS resonances split symmetrically away from zero bias with a kink at $V_{SD}^{(2)} = \pm 0.03$ mV, forming a ‘diamond’ shape. The simultaneous measurement of G_3 in Fig. 5.4(d) reveals similar V_{P2} dependence of the ABS energy. Note that the next excited states were located at $V_{SD}^{(2,3)} = \pm 0.09$ mV and were also affected around $V_{P2} \approx -0.030$ V leading to a ‘bowtie’ shape.

5.4 CONCLUSION

The appearance of ABSs with ‘bowtie’- and ‘diamond’-shaped patterns while on resonance with the QD level is an indication of the QD being sufficiently tunnel coupled to the ABSs such that the two energy levels significantly hybridize, consistent with theoretical and previ-

ous experimental results^{116–119,125}. The measurement of the energy shift at both ends of the 0.6 μm NW, while a local gate voltage at only one end is changed, is a nonlocal signature of the delocalized ABSs. If tunneling spectroscopy is measured at both ends of a NW, hybridization of bound states with a local QD can be used as a quantum mechanical tool to test whether a quantum state extends through the whole NW, similar to the analysis of cross-conductance and correlated appearance at both ends^{64,123}. This is in contrast to experiments where spectroscopy is performed at one end of a NW. In such a case, a QD in the absence of a bound states in the NW can mimic signatures of extended states inside the NW in tunneling spectroscopy^{44,125–129}.

In comparison to previous experiments, the present set-up offers additional information about the spatial extent of the bound state, as one can perform tunneling spectroscopy at at both ends of the NW segment. This also allows for the observation of the change in energy of the ABS at one position while it is being hybridized with a QD 0.6 μm away by the means of changing a local gate. This nonlocal signature is a demonstration of the ABS being an extended quantum state. Note that we do not observe anticrossings of the bound state with the QD resonances in bias spectroscopy which is consistent with the states being attributed to ABSs as opposed to partially overlapping Majorana zero modes¹¹⁷.

This experiment was repeated with a second device, which had a slightly different design. The side probes did not have Al leads, and were made up of bare semiconductor. These measurements showed similar results when an ABS in a NW was brought onto resonance with a QD localized at one probe while observing the impact of the hybridization on the bound state at the other probe. The results from this second device, as well as expanded data for the first, are available in the Supplementary Information of the relevant publication⁸³.

Science, my lad, is made up of mistakes, but they are mistakes which it is useful to make, because they lead little by little to the truth.

Jules Verne

6

Formation and control of quantum dots in InAs 2DEGs

IN THIS CHAPTER, we will cover the formation of quantum dots (QDs) in our superconductor-semiconductor hybrid structures, and discuss how we can control their properties by design and electrostatic tuning. The chapter is intended as a guide to forming QDs in these 2DEG structures, in our configuration where they are side-coupled to a gate-defined NW, and then controlling the coupling both between the QD and the NW, and between the QDs and the leads used to probe the system. We will elaborate on why changing the coupling is interesting, and what purpose we have in mind for the different possible coupling regimes.

6.1 DEVICE DESIGN

The idea behind the devices which are presented here was the following; we were previously able to study ABSs in segments of varying length using multiprobe devices, so we know we can make a NW in which we confine ABSs, and probe them from one or two sides via tunnelling spectroscopy using a normal (or gapless superconducting) lead [chapters 3, 4]. We also found that we were unable to avoid forming accidental QD resonances in our probe locations, however it turned out that we could use these accidental resonances by allowing them to hybridize with the NW states [chapter 5]. So accidental QDs found in our tunnel regions could be used to confirm the extended or ‘nonlocal’ nature of the states in our systems, but we had very little control over the nature of these QDs. The idea born out of this was to have deliberately defined lateral QDs confined in the probe locations. The requirements that we decided for this type of device were as follows:

- A NW with segments of differing length, as before, the chemical potentials of which are individually tuneable.

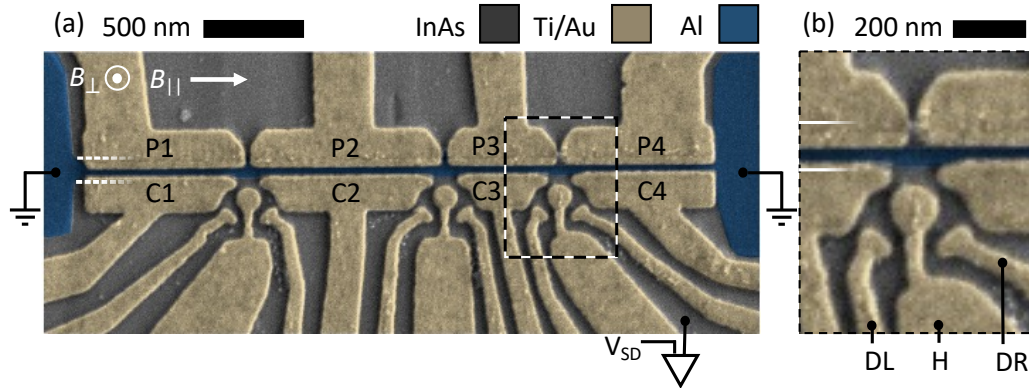


Figure 6.1: (a) Scanning electron micrograph of a device which is identical by design to device 1. The device consists of a thin strip patterned from epitaxial Al atop an InAs quantum well. The Al strip is marked at the left edge by a dashed white line, and extends into large grounded planes at both ends. The gates labelled P and C deplete the carriers in the 2DEG either side of the Al, such that a quasi-1D proximitized NW is formed. These gates can additionally be used to tune the chemical potential in the NW, segment by segment. The gates labelled C also form tunnel barriers to normal leads at three locations along the NW, where voltage pre-amplifiers are connected. A voltage bias V_{SD} is applied via the amplifiers, as shown at the third probe location. Relevant field directions are marked in white; parallel to the NW ($B_{||}$) and perpendicular to the plane of the 2DEG (B_{\perp}). (b) A magnified view of the third probe location. The gates DL and DR allow for a laterally confined QD to be formed at the probe location, and can be used to tune the coupling between the QD and the normal lead. The gate H provides additional control over the QD.

- Multiple probe locations along the length of the NW.
- Gate defined QDs in each probe location, with a controllable coupling between the QD and the NW, and also between the QD and the normal lead. (This item was one of our original design objectives, to make a multi-purpose device. We found different variations of our design to lend themselves more naturally to different coupling regimes. This will be highlighted in the following device descriptions.)

The devices which were investigated for this section of the thesis are shown in Fig. 6.1 and 6.2, and are labelled devices 1 and 2 respectively. They are similar in many ways to the multi-probe geometries described in the previous chapters. At the heart of both device 1 and 2 is an thin strip wet-etched from the epitaxial Al, forming a NW ~ 4 microns in length,

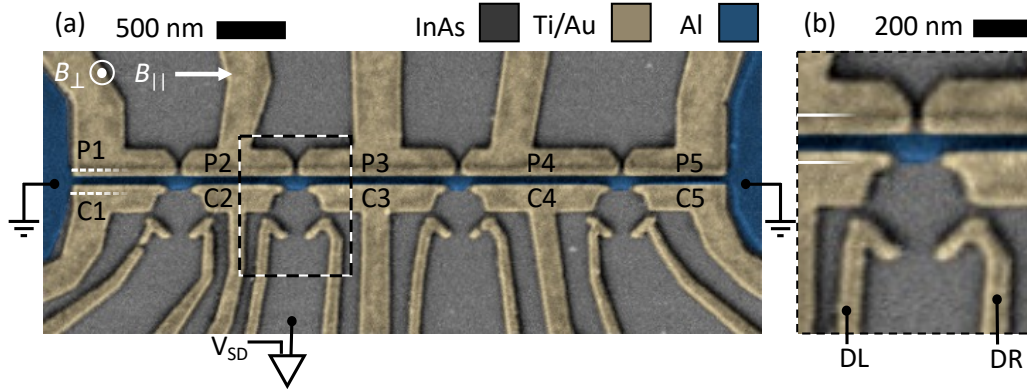


Figure 6.2: (a) Scanning electron micrograph of a device which is identical by design to device 2. The device consists of a thin strip patterned from epitaxial Al atop an InAs quantum well. The gates labelled P and C deplete the carriers in the 2DEG either side of the Al, such that a quasi-1D proximitized NW is formed. These gates can additionally be used to tune the chemical potential in the NW, segment by segment. The gates labelled C also form tunnel barriers to normal leads at three locations along the NW, where voltage pre-amplifiers are connected. Relevant field directions are marked in white; parallel to the NW ($B_{||}$) and perpendicular to the plane of the 2DEG (B_{\perp}). (b) A more magnified view of the second probe location. The gates DL and DR allow for a laterally confined QD to be formed at the probe location, and can be used to tune the coupling between the QD and the normal lead.

and expanding into large ground planes at either end. Above this, Ti/Au gates are deposited, separated from the Al by ~ 15 nm of HfO_2 .

The gates which are labelled P and C are used to fully deplete the carrier density in the 2DEG below, except where it is screened by the Al strip, forming a quasi-1D conductance channel - our NW. These gates can then be additionally adjusted to change the chemical potential in the different segments of the NW. The gates labelled C are also used to form tunnel barriers probes, close-ups of which are shown in Fig. 6.1 (b) and 6.2 (b). By design, the idea is that the C gate voltages are optimized to form tunnel barriers, while the P gate voltages are used to tune the chemical potentials in the segments, but in reality it is necessary to use both P and C to tune the segment into the desired regime (be that a hard gap or a certain density of sub-gap states), so some compensation is needed to achieve the desired tunnel barrier and the desired NW conditions at the same time.

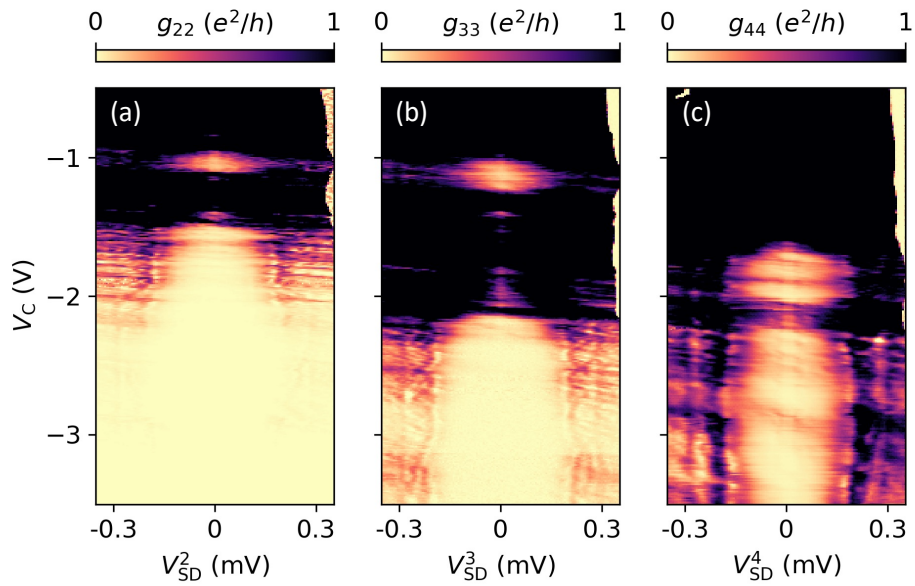


Figure 6.3: Tunneling spectroscopy measurements as a function of all C gate voltages swept together, at zero magnetic field. The depletion with the C gates creates QPC-like tunnel barriers in the probe locations of device 2, allowing for tunneling spectroscopy to be measured at each probe location. As the tunnel barriers form, the superconducting gap becomes visible in spectroscopy for probes 2, 3 and 4 in (a), (b), and (c) respectively. The D gates are not energized, so that the dots are not formed. The conductance is saturated at $1 e^2/h$ here, so that fainter features may be seen.

The gates used to form QDs in the probe locations are what set devices 1 and 2 apart from each other. device 2 (Fig. 6.2) has just two additional gates in each probe location, labelled DL and DR. When these are depleted, a QD is confined. These gates can then be set to a more or less negative gate voltage depending on the desired coupling between the normal lead and the QD. Once the QD is formed, the C gates can also be adjusted to tune the coupling between the QD and the hybrid NW. device 1 (Fig. 6.1) similarly has gates DL and DR to confine the QD, although they are closer to the C gates, leaving a smaller area for the QD to be formed in. The other crucial difference is that device 1 has an additional gate in each probe location, labelled H. This gate sits directly on top of the putative location of the QD. This allows for a high degree of control over the dot, as the H gate has a strong lever arm to it. This gate can also be used to make additional adjustments to the coupling between lead and QD or QD and NW. One should beware, however, since it simultaneously has a strong effect on the QD itself and on both tunnel barriers.

6.2 TURNING ON THE PROBES

At 0 V applied to all gates, the 2DEG is undepleted and therefore conducting. Before starting to form QDs, a typical first step in the investigation of these devices is the formation of tunnel barriers into the NW at one or multiple probe locations. The P and C gates are energised to deplete the carrier density at either side of the Al strip, so that the NW is formed, and then the C gates are adjusted so that each lead is connected via a tunnel barrier to the NW. The D gates remain at 0 V. An example is shown in Fig. 6.3 for device 2, where three simultaneous differential conductance measurements are taken as the the barriers are pinched off using the C gates, using standard lockin techniques as elaborated in section 2.3.2. This configuration

can be used for tunneling spectroscopy studies of the NW, or (as we are using it here) as a precursor to the formation of a QD side-coupled to the NW. Setting the C gates to the tunneling regime creates the top barrier, which will determine the tunnelling rate between the QD and the hybrid NW. Notice that in Fig. 6.3, the conductance through tunnel barrier 2 is pinched off at more positive gate voltages than the other two barriers. This is due to microscopic variations between the junctions, and is common in our devices.

6.3 FORMING A DOT

Once the barrier into the NW is set somewhere in the tunneling regime, it is possible to start forming QDs in the probe region by energizing the DL, DR gates. Applying a magnetic field $B_{\perp} > \sim 0.15$ T is sufficient to drive the hybrid NW normal, so that the superconducting gap is closed, resulting in a continuous DOS at the Fermi energy, which simplifies the tuning of a QD. The initial formation of the QDs can therefore be done at some finite perpendicular field, fixing the voltage bias to zero and depleting with the D gates until Coulomb oscillations are seen in the differential conductance. Such a measurement is shown for probe location 2 of device 2 in Fig. 6.4 (a), with a more resolved measurement of the lower part of the gate voltage range in (b).

Here it is worth contrasting devices 1 and 2, because the structure of the Coulomb peaks differs for these two device configurations. We can start by examining Fig. 6.5, which shows measurements from one of the QDs formed in device 2. These measurements are taken in a finite 0.15 T perpendicular magnetic field at zero voltage bias on the lead.

In general, it is useful to measure maps such as the ones in (a) and (b), which allow one to observe the effect of the C and D gates. Here all C gates and all D gates on the device are

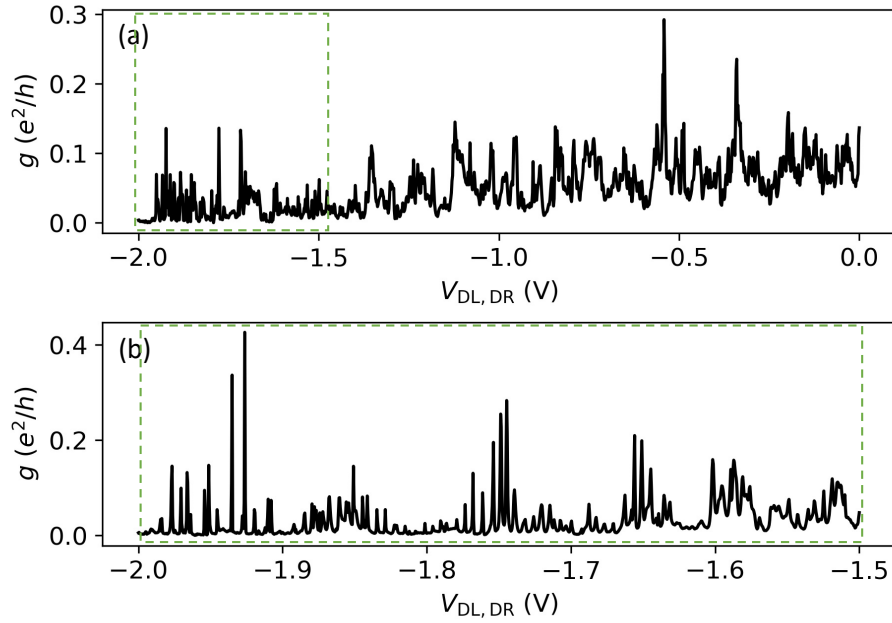


Figure 6.4: (a) Differential conductance measured at zero applied voltage bias on the normal lead, showing the onset of Coulomb blockade for the QD in probe location 2 of device 2 as it is formed by confining with the gates DL and DR. The measurements are taken with B_{\perp} at 0.15 T. Here the P gates are depleted to $V_{P1, P2, P3, P4, P5} = (-6.2, -6.2, -3.8, -6.4, -6.2)$ V and the C gates are depleted to $V_{C1, C2, C3, C4, C5} = (-5.2, -4.2, -5, -5.6, -6)$ V. (b) A smaller range of DL, DR space showing a large number of periodic Coulomb peaks swept through as the QD is confined.

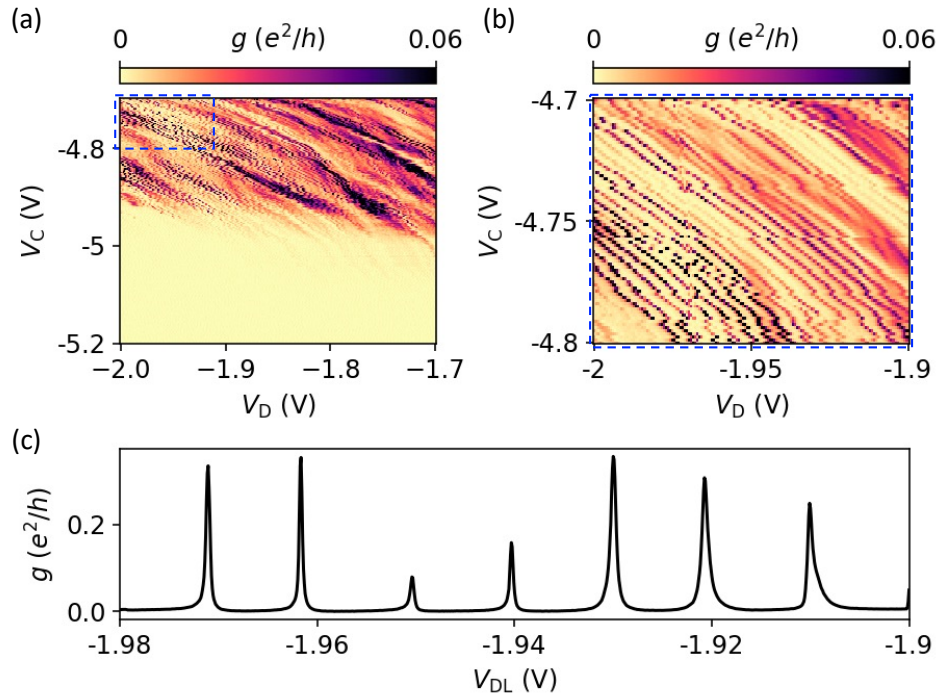


Figure 6.5: (a) Differential conductance measured at zero bias, showing a QD in device 2 confined with C and D gates. Here all C gates and all D gates are swept simultaneously, and the measurements shown are taken on probe location 2. (b) Higher resolution scan of the section of (a) indicated by the dashed blue line, showing many regular Coulomb blockade peaks. The resonances couples to both the C and the D gates, indicating that the dot is formed in the desired location on the device. (c) Coulomb peaks in differential conductance measured at zero applied voltage bias as a function of V_{DL} .

swept simultaneously (labelled V_C and V_D), and while the data shown is for only one of the normal leads, measurements were carried out with all leads simultaneously. This is a coarse but efficient way to move towards tuning up multiple QDs at once. The benefit of mapping the effects of the C and D gates is that the C gates, as mentioned before, tune the barrier at the top of the dot, controlling tunneling into the hybrid NW, while the D gates form the bottom barrier, confining the QD from below and controlling tunneling from the normal lead in to the dot. So these maps allow one to observe different stages in the confinement of the QD from all sides. Figure 6.5 (a) serves as more of an overview, as a very large number of Coulomb resonances are swept over within the measured range, and they are barely resolvable. This is useful to see that the QD is formed, and can be used to assist one in tuning into a specific coupling regime (more on this later in the chapter). Figure 6.5 (b) is a higher resolution measurement of a region of (a). Here, individual Coulomb peaks are clearly resolvable. One can note that the resonances respond to both C and D gates, indicating that the QD is formed within the desired region. The resonances are numerous and very regularly ordered. A one dimensional measurement taken in the same region of gate space by sweeping just one of the D gates, DL, shows regular and well resolved Coulomb peaks [Fig. 6.5 (c)].

Taking a more detailed look at the QD that has been formed in this configuration requires us to depart from zero voltage bias. Coulomb diamonds as a function of voltage bias and $V_{DL,DR}$ for a QD in device 2 are shown in Fig. 6.6 (a) for finite perpendicular magnetic field (0.2 T), where the superconducting gap in the NW is closed. There is a difference in the coupling to the source and drain Γ between the different resonances, as can be observed by their varying width, but the CB structure is overall very regular, with a charging energy of $\sim 600\mu\text{eV}$. One should note that in these structures, the charging energy is variable based

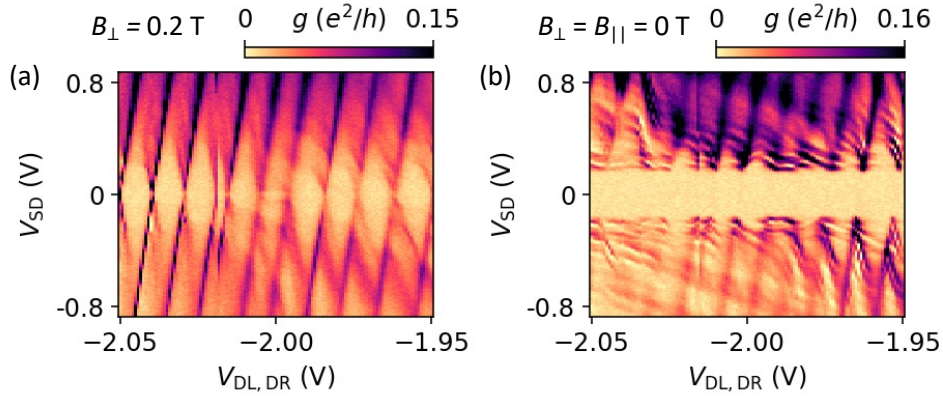


Figure 6.6: (a) Differential conductance measurement showing Coulomb blockade as a function of voltage bias and $V_{DL,DR}$ for probe location 2 on device 2 at $B_{\perp} = 0.2$ T, a magnetic field at which the superconducting gap is closed and the hybrid NW, which acts as the drain, is normal. (b) The same measurement but at zero magnetic field, so that the drain is superconducting and a gap is visible in spectroscopy.

on gate regime, since the gate voltage values have a significant effect on the size and shape of the dot. At zero applied magnetic field [Fig. 6.6 (b)] the hybrid NW, which serves as the drain, has a superconducting gap, and this results in a gap in transport around zero bias voltage, with the Coulomb diamond tips appearing above the gap, as is standard in N-Dot-S measurements with weak coupling¹³⁰. Additional features of the above gap spectrum appear in the zero field measurement, and hybridize with the QD resonances. These are thought to be effects of a non-trivial density of states in the semiconducting leads.

These regular CB features observed in device 2 can be contrasted with the QDs which form in device 1 when the D gates are energized. Measurements taken at finite perpendicular magnetic field and zero voltage bias are shown in Fig. 6.7, which can be directly compared to Fig. 6.5. The CB resonances in this case are clearly grouped, often into pairs, implying a clearer even-odd structure to the dot. This means that for experiments which require easy access to the spin structure of the dot, the design of device 1 offers an advantage. Note here

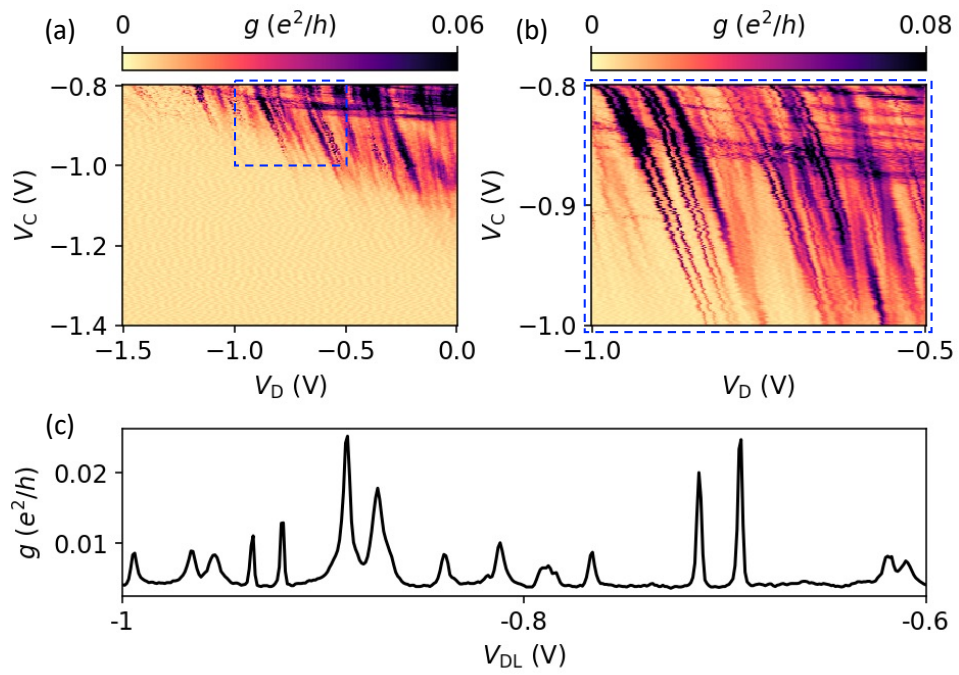


Figure 6.7: (a) Differential conductance measured at zero bias, showing a QD in device 1 (probe location 3) confined with C and D gates. The H gate is not energised. (b) Higher resolution scan of part of (a), showing Coulomb blockade peaks which appear in pairs, suggestive of an even odd structure. (c) Coulomb peaks in differential conductance measured at zero applied voltage bias as a function of V_{DL} .

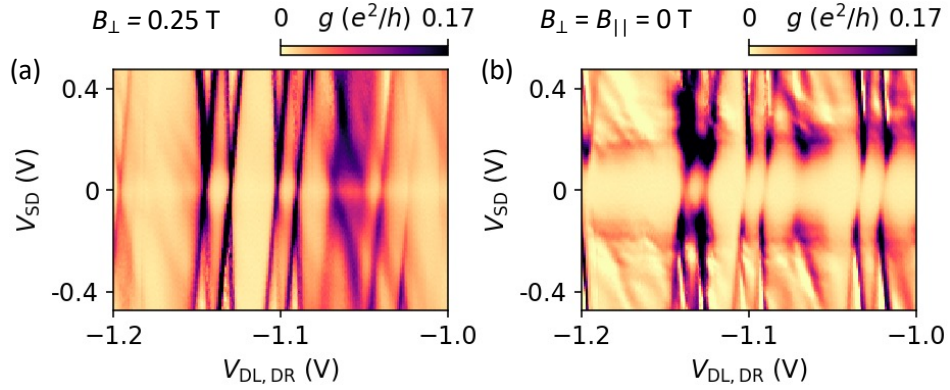


Figure 6.8: (a) Differential conductance measurement showing Coulomb blockade as a function of voltage bias and $V_{DL,DR}$ for device 1 at $B_{\perp} = 0.2$ T, a magnetic field at which the superconducting gap is closed and the hybrid NW, which acts as the drain, has a continuous DOS. (b) The same measurement but at zero magnetic field, so that the drain is superconducting and a gap is visible in co-tunneling spectroscopy.

that the H gate is not energized (set to 0 V) during these measurements; our interpretation is that just the presence of the circular gate on top of the QD formation location helps to screen the barrier area from some disorder, as well as localizing the QD and making it more symmetric. Coulomb diamond measurements as a function of V_{SD} and $V_{DL,DR}$ for device 1 are presented in Fig. 6.8. Here the pairing of the resonances is clearly visible, both at finite (a) and zero (b) magnetic field. The charging energy is $\sim 760 \mu\text{eV}$, but in contrast to the QD formed in the previous device, the level spacing δE is significant, so that the resonances are grouped into even odd pairs.

6.4 TUNING THE COUPLING

One of the advantages of the gate layout in which our QDs are defined is the separate tunability of the couplings Γ_N (normal lead - dot) and Γ_S (QD - hybrid NW), with the D gates and C gates respectively. The data shown in this section is for device 2 only, but similar logic

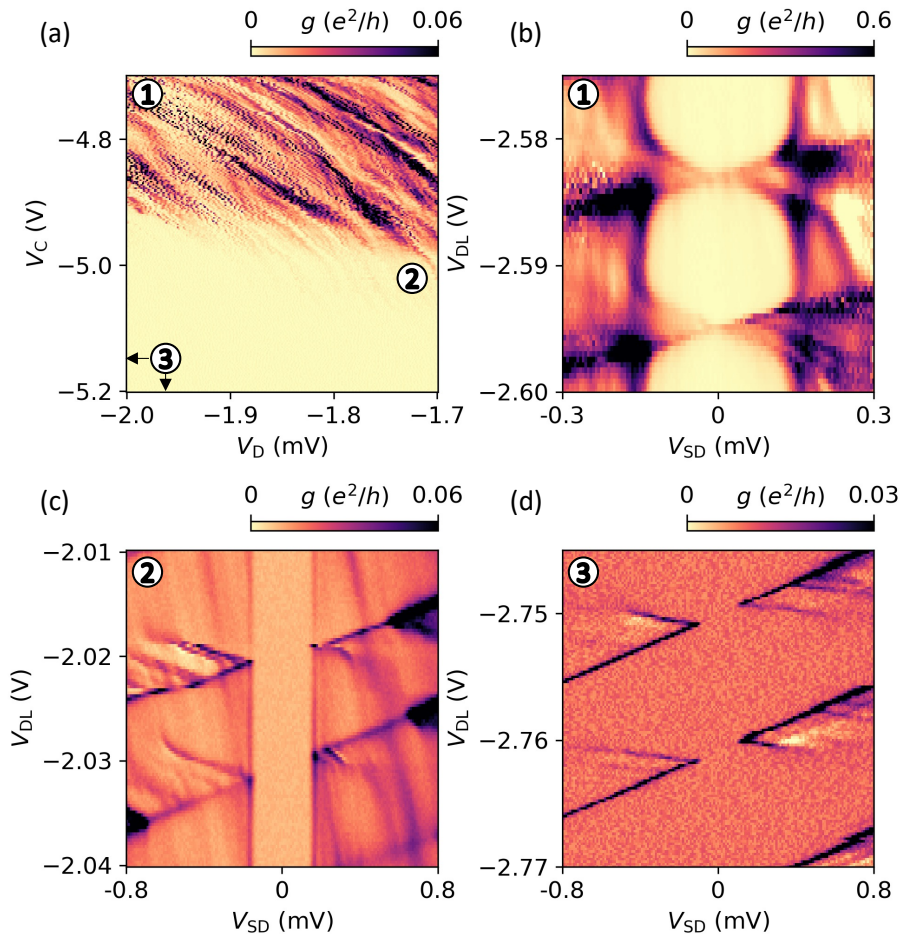


Figure 6.9: (a) Differential conductance measured at zero bias as a function of V_C and V_D (B_{\perp} at 0.15 T), which control the tunnel barrier between the QD and NW and the lead and the QD, respectively. Regions in which different coupling regimes are demonstrated are labelled with numbers. (b) (B_{\perp} at 0.05 T) QD resonances in a relatively strongly coupled regime (1) in which the QD levels hybridize with the NW DOS. (c) (B_{\perp} at 0.05 T) resonances measured in a regime of intermediate coupling (2), where hybridization is reduced but co-tunneling processes persist. (d) (B_{\perp} at 0.08 T) resonances measured in a weak coupling regime (3), where co-tunneling processes are suppressed and sequential tunneling dominates, and the gap is seen only as an offset between the Coulomb diamond tips.

applies when one wishes to change the couplings in devices with a slightly different design like device 1.

Applying a finite perpendicular magnetic field, so that the gap in the NW is closed and Coulomb resonances can be detected at zero bias, we can use differential conductance map of V_C versus V_D , now not just to see Coulomb resonances but to select what region of gate space to measure in to achieve a certain tunnel coupling. Such a map is shown in Fig. 6.9 (a), with numbers indicating the region of gate space in which the subsequently discussed various coupling regimes are demonstrated.

It should be emphasised that the control which we can exert over the couplings in these device configurations is very non-monotonic. By making the C gates more positive one opens the upper tunnel barrier, and thus increases the coupling between QD and NW, while conversely them more negative one pinches off and decreases the coupling. But one can see from (a) that there is a nontrivial variation in the brightness of the Coulomb peaks, as well as additional resonances which respond to both the C and D gates. Both tunnel barriers themselves have a mesoscopic behavior, so that the tunnel coupling fluctuates somewhat with gating. Random disorder-based resonances in both junctions have a significant effect on the main QD couplings. However, by selecting general regions based on the original logic, it is still possible to tune into the desired coupling regime. At the gate voltage region indicated by the number 1 in Fig. 6.9 (a), the C gates are fairly positive, above -4.8 V. This is fully sufficient to form the hybrid NW and to confine a well defined dot, already in a regime where regular Coulomb resonances are visible, but the conductance values measured reach above $0.6 e^2/h$, a significant tunnel coupling. Measuring the QD resonances in this region as a function of V_{SD} [Fig. 6.9 (b)] at $B_{\perp} = 0.05$ T, where the gap is open, we observe that the

QD resonances hybridize with the NW, forming bound states which penetrate into the superconducting gap. There is also a significant co-tunneling contribution. We term this the more strongly coupled regime, within the scope of these devices. Measuring in this coupling regime at higher magnetic field, it is possible to do experiments similar to those discussed in Chapter 5, where a QD is able to hybridize with the NW states, showing a characteristic signature. We found that this regime of coupling was readily accessed in device 2, as shown in the Fig. 6.9, but we were unable to tune device 1 into a similar regime. It was possible to see some hybridization signatures, but the C gate voltages had to be very positive, so that the quality of the spectroscopy suffered significantly.

In device 2, when the D gates were set to be more negative and the C gates more positive (again, see number 1 in Fig. 6.9 (a)), it is possible that the location of the QD physically shifted away from the negative D gates and toward the upper tunnel barrier location, helping to increase the coupling to the superconductor. We theorise that the presence of the H gate, which (as previously mentioned) produced a better localized and more symmetric dot, which actually hindered the coupling to the superconductor. This is due to it keeping the QD localized in one place, below the circular part of the gate, even with no voltage V_H applied.

The region indicated by number 2 is what we term the intermediate coupling region. In Fig. 6.9 (a), one can see that the zero bias transport magnitude is significantly reduced. Measuring as a function of bias at $B_{\perp} = 0.05$ T, the transport looks very different from the previously discussed regime. The QD resonances no longer induce any sub-gap states, instead their tips stop at the gap edge. The conductance is about an order of magnitude lower. However, the gap is still clearly visible in co-tunneling spectroscopy, and some hybridization is still visible at high bias between the QD and the above-gap states in the leads.

The final coupling regime which we will discuss is marked by the number 3 in Fig. 6.9. The exact region used is not visible in panel (a); both the C and D gates are set slightly more negative than the range of this panel, with V_C at -5.5 V and V_{DR} at -2.55 V. Here the coupling is very weak, and there is almost no conductance visible at zero bias, finite field. Measuring bias spectroscopy at $B_{\perp} = 0.05$ T, one can no longer see any trace of the gap in co-tunneling spectroscopy, and there are no hybridization signatures. The superconductor now acts as a very decoupled drain contact, so that the only evidence of it is the separation and shift in between the Coulomb diamond tips, which corresponds to the drain contact having a gap in its spectrum above the Fermi level. This shifting of the tips is the basis for the use of a singular QD level as a spectrometer of the density of states; if we can detect the gap then it follows that we can extract the size of the gap, and that we can also observe other spectral features using the same logic. More on this follows in the next chapter.

6.5 BIASING CONFIGURATIONS

For the majority of this thesis, the biasing setup is as demonstrated in Fig. 2.6. The superconducting NW is grounded, and a variable voltage bias is applied to the normal leads. We also tried out a second biasing configuration, one in which both AC and DC components of V_{SD} were connected via a voltage divider to the superconducting NW, and the normal lead was grounded. The other leads were floated during this measurement. A direct comparison of the two different biasing configurations, and both zero and finite perpendicular fields (corresponding to the hybrid NW being superconducting and normal respectively), is shown in Fig. 6.10. (a) and (b) are measured using our standard method of biasing on the lead, while (c) and (d) are biased on the Al. The main transport features remain the same

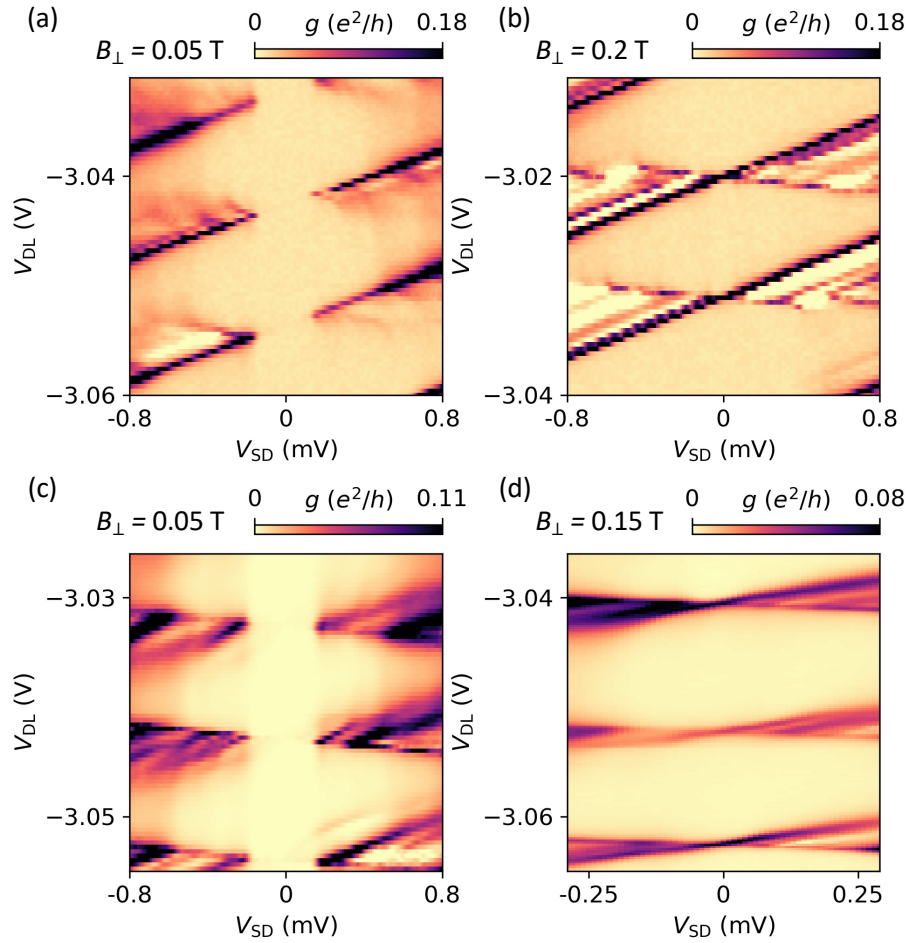


Figure 6.10: (a,b) Differential conductance measurement of QD levels with the voltage bias applied to the normal lead and the hybrid NW grounded; the standard measurement configuration for this thesis. Coulomb diamonds shown at zero and finite perpendicular magnetic field, respectively. (c,d) Differential conductance measurement of QD levels with the voltage bias applied to the hybrid NW, and the normal lead grounded. Shown at zero and finite perpendicular magnetic field, respectively.

for both methods; Coulomb blockade is still observed in an intermediate coupling regime, where the conductance is below $0.2 e^2/h$ and some co-tunneling transport is visible. The gap is observable in both configurations at low field, as expected. Beyond that, the Al biasing configuration shows a more symmetric Coulomb diamond structure, but does not appear to offer any advantage in terms of spectroscopy quality.

6.6 CONCLUSIONS

In this section, we have examined how QDs can be formed in InAs 2DEG heterostructures, and how these QDs can be measured in a N - QD - S configuration. The device designs presented in this chapter can be used to reliably produce QDs with $E_C \sim 600 \mu\text{eV}$. We have found that placing a circular normal metal gate directly above the location where the QD should form allows for a more localized and symmetric QDs, which demonstrate clear even-odd behavior. In contrast, omitting the circular gate and leaving a slightly larger area for QD formation allows for large regions of very regular Coulomb blockade, and a higher tunability of the couplings to the leads. Both designs allow for tuning of the couplings Γ_S and Γ_N in a way which is non-monotonic, but is still reliably usable. These designs can be adjusted for a range of uses in hybrid structures; one of these will be explored in depth in the next chapter.

*If people think nature is their friend, then they sure don't
need an enemy.*

Kurt Vonnegut

7

Spin-resolved spectroscopy using a quantum dot defined in InAs 2DEG

This chapter is a modified and supplemented version of the data and text presented in the following manuscript:

Spin-resolved spectroscopy using a quantum dot defined in InAs 2DEG, by *Alisa Danilenko*, Andreas Pöschl, Deividas Sabonis, Vasileios Vlachodimitropoulos, Candice Thomas, Michael J. Manfra, and Charles M. Marcus.

IN THIS SECTION, we will discuss the use of our side-coupled quantum dots (QDs) as probes of the density of states in the hybrid nanowire (NW). The QDs are operated in a strongly decoupled regime, such that they do not hybridize with the NW states. When a magnetic field is applied (parallel to the NW axis), the QD levels are split by the Zeeman effect, allowing for spin-resolved spectroscopy. We take advantage of this by measuring the spin-splitting of the superconducting gap, extracting a g -factor of ~ 1.7 , consistent with regular tunnelling spectroscopy measurements of the system. We further investigate a localized bound state in the NW, using sequential tunnelling spectroscopy through the spin-split QD levels to extract the magnitude and relative sign of the state g -factor. Finally, we define metrics of spin and charge polarization of the current into the state in the NW as measured via the QD spectrometer, and examine these quantities as a function of applied magnetic field parallel to the NW, and gate voltage.

7.1 INTRODUCTION

When indium arsenide (InAs), a semiconductor, is coupled to aluminum (Al), a superconductor, the two materials inherit properties from each other, effectively creating a new material system. The proximity effect induces a superconducting pairing in the InAs via Andreev

reflection from the Al, opening a gap in the spectrum of the otherwise semiconducting system. A large g -factor and the presence of spin orbit coupling (SOC) in the hybrid system are inherited from the InAs^{100,131}.

One platform in which structures of this kind can be realized, and complex device geometries can be fabricated in a scalable manner, is a two-dimensional electron gas (2DEG) proximitized by a superconducting layer^{5,101}. If these hybrid systems are restricted to one dimension by gating, they become a hunting ground for a range of quantum states including Yu-Shiba-Rusinov (YSR), Andreev bound states (ABS), and Majorana bound states (MBS)^{45,66,102–105,132,133}. These quantum states possess properties such as spin and electron-hole polarization, which respond to experimental parameters. There have been several proposals for the use of QDs (QDs) to probe NW state properties to elucidate their parity, spin texture, and localization^{116,117,119}. Corresponding experimental efforts have already enabled investigation of the spatial extent of bound states using strongly coupled QDs which hybridize with the bound states^{83,118}. Previous experiments used a weakly coupled QD to read out the size of the superconducting gap in a proximitized region¹³⁰, and to probe the above-gap resonances in the density of states (DOS) of a similarly proximitized system¹³⁴ as well as transport through sub-gap resonances¹³⁵. The use of QDs as spin filters has been exploited in the context of spin qubits¹³⁶, and their charge filtering properties have been utilized to probe the quasiparticle charge and energy relaxation in hybrid structures¹³⁷. However, QDs have not yet been used to address the spin and charge degrees of freedom of discrete sub-gap states in hybrid NWs.

In this manuscript, we introduce a device geometry based on InAs 2DEG which allows for laterally defined QDs that are side-coupled to a quasi-1D hybrid NW at multiple probe locations. The QDs are defined by electrostatic gating. The gate configuration allows the

QDs to be strongly decoupled from the NW. This means that they do not interact with the DOS in the NW, and can be used as non-perturbative probes. When a magnetic field is applied to the system, the QD energy levels are split by the Zeeman effect, such that they can be used as spin-selective probes. We take advantage of this, using the QD levels to measure the spin-splitting of the superconducting gap¹³⁸, extracting a g -factor of ~ 1.7 , consistent with regular tunneling spectroscopy measurements of the system. We further investigate a bound state in the NW, using sequential tunneling spectroscopy through the spin-split QD levels to extract the magnitude and relative sign of the state g -factor. Finally, we define metrics of spin and charge polarization of the current into the bound state as measured via the QD spectrometer, and examine these quantities as a function of applied parallel magnetic field and chemical potential. If the gates which form the QDs are not energized our gate geometry allows for regular tunnelling spectroscopy through a quantum point contact (QPC)-like potential barrier, allowing for a second, independent measurement mode of the sub-gap energy (without filtering properties), which is self-consistent with the QD spectroscopy.

The organization of the chapter is as follows: first, the device design is introduced (7.2). Next, the use of QD levels as spectrometers is explained at low magnetic fields (7.3) and then in the presence of a high magnetic field (7.4). Finally, the spin and particle-hole polarization of tunneling current through the QD - bound state system is investigated (7.5), and the results are discussed in the context of the current literature (7.6).

7.2 DEVICE DESIGN

A scanning electron micrograph of a device which is identical by design to device 1 is shown in Fig. 7.1. The device is fabricated on InAs 2DEG topped with 5 nm of epitaxially matched

Al. Following a mesa-etch, an additional wet etch is used to define an Al stripe of ~ 100 nm in width and $\sim 4 \mu\text{m}$ in length, which extends into large ground planes at both ends. A layer of 15 nm HfO_x is deposited globally and functions as gate dielectric. Ti/Au gates are then evaporated in two lithographic steps, one thin layer for fine features and a thick outer layer that crawls over the mesa and makes contact with the thin layer. The gates labelled P and C are used to deplete the carriers in the 2DEG self-aligned with the strip of Al, so that a quasi-1D proximitized channel is defined. The gates separate the NW into segments so that different segments can be tuned to have different chemical potentials by changing the applied gate voltage, allowing some control over the spatial distribution of bound states in the system. Additionally, the gates labelled C are used to define tunnel barriers at three locations along the NW. The planes of 2DEG, separated by the depletion of the C gates from the NW, are used as normal conducting leads.

The results highlighted in this paper will focus on measurements in the section of the device shown by the dashed box in Fig. 7.1(a). A close up image of this region, with the QD coupled to the NW from the side, is shown in Fig. 7.1(b). By depleting with the gates C_3 and C_4 (leaving gates DL, H and DR at 0 V), a QPC-like potential barrier is formed, through which differential conductance can be measured using standard lock-in techniques. Differential conductance measurements as a function of magnetic field parallel to the NW (B_{\parallel}) are shown in Figs. 7.1 (c) and (d) for two different values of V_{P_3} . With $V_{P_3} = -0.580$ V the induced superconducting gap is seen closing in field with no sub-gap resonances, while at a slightly more positive gate voltage of -0.537 V there is a sub-gap state which splits in field and undergoes an anti-crossing at 1 T. Zero bias gate-gate maps were taken at finite field to determine how strongly this state couples to different gates. Results showed that that the

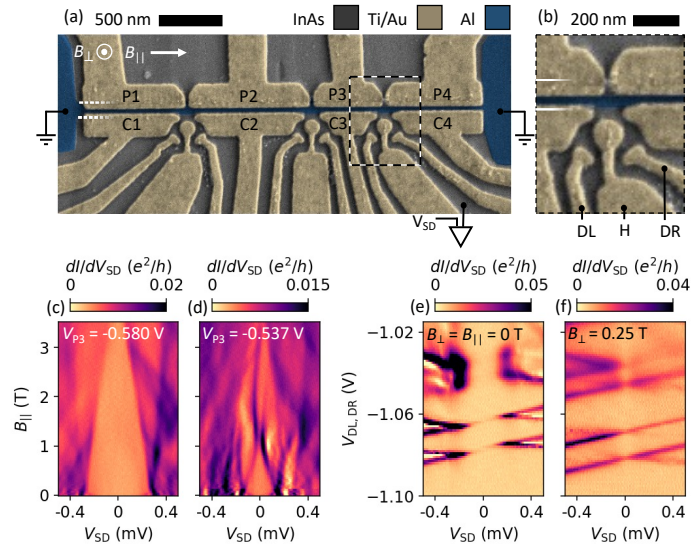


Figure 7.1: (a) Scanning electron micrograph of a device which is identical by design to device 1. The device consists of a thin strip patterned from epitaxial Al on top of an InAs quantum well. The gates labelled P and C deplete the carriers in the 2DEG either side of the Al, such that a proximitized NW is formed. These gates can additionally be used to tune the chemical potential in the NW, segment by segment. The gates labelled C also form tunnel barriers to normal leads at three locations along the NW, where voltage pre-amplifiers are connected. Relevant field directions are marked in white; parallel to the NW (B_{\parallel}) and perpendicular to the plane of the 2DEG (B_{\perp}). (b) A magnified view of the third probe location (dashed box in (a)). The gates DL and DR allow for a laterally confined QD to be formed at the probe location, and can be used to tune the coupling between the QD and the normal lead. The gate H allows for additional control over the QD. (c), (d) Tunneling spectroscopy measured at the third probe location as a function of B_{\parallel} , for two different values of V_{P3} . In (c) the closing of the superconducting gap as a function of magnetic field is observed without sub-gap features, while in (d) a bound state in the gap splits and an anti-crossing is observed. During these measurements the voltages on the QD-related gates (DL, H, DR) are set to 0 V, so there is no QD in the probe location, just a tunnel barrier formed by the gates C3 and C4. (e), (f) Coulomb blockade measurements of the QD formed by energizing DL and DR, at zero and finite B_{\perp} respectively.

state of interest is mostly localized in the NW segment underneath the P_3 gate.

When the left and right D gates are energized with negative voltages, electron density is confined, forming a QD. The voltage configuration of these gates can be used to tune the coupling between the QD and the normal lead. The C gates can be further adjusted to tune the coupling of the QD to the NW. The H gate, with a circular part situated directly on top of the region where we expect the QD to form, can be used for further control over the QD. Using a combination of these gates it is possible to tune over a range of coupling strengths, but towards the strong coupling limit this effect is somewhat non-monotonic. Differential conductance measurements with the QD formed in the probe location are shown in Fig. 7.1 for zero applied field (e) and $B_{\perp} = 0.25$ T (f), with the latter field large enough to turn the Al of the NW normal and close the induced superconducting gap.

7.3 SPECTROSCOPY AT LOW MAGNETIC FIELD

To use a QD as a spectrometer of the DOS in the NW, it is necessary to operate in a strongly decoupled regime, where both the coupling between the QD and the superconductor (Γ_S) and between the normal lead and the QD (Γ_N) are much less than $k_B T$, such that co-tunneling processes are suppressed and sequential electron tunnelling dominates^{130,139}. In this case, and provided that $\Gamma_S < \Gamma_N$, the sequential dc current flowing into the NW is proportional to the DOS at an energy E selected by the chemical potential of a single dot level. The energy window for the measurement is selected by the dc voltage bias on the normal lead, and the level spacing of the QD must be larger than the selected energy window for spectroscopy to be performed. The concept is illustrated in Fig. 7.2 for the case of a single sub-gap state. Panels (a) and (c) show sketches of the electrochemical potentials involved in standard spectroscopy

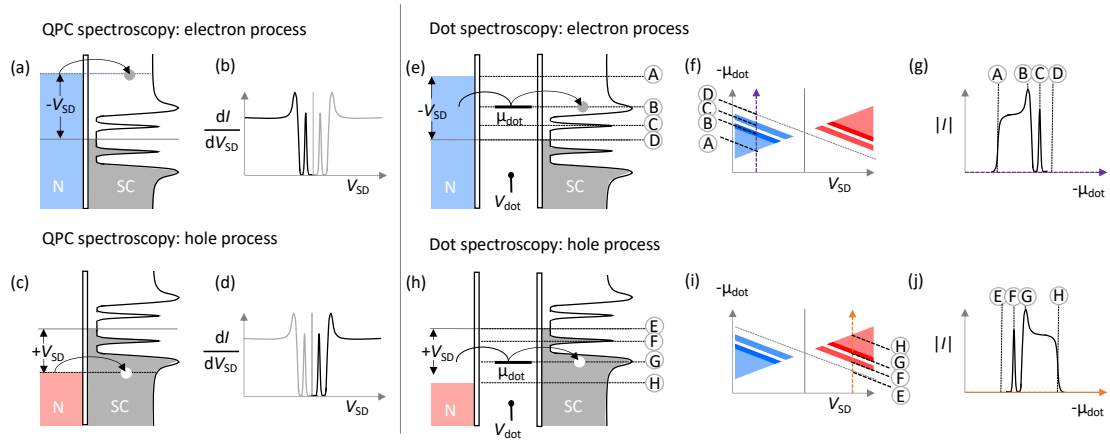


Figure 7.2: A schematic representation of the use of a single level of the QD as a spectrometer to measure the DOS in the proximitized NW, shown with one sub-gap ABS feature at zero applied magnetic field. (a, c) Sketches of the electrochemical potentials involved in standard tunneling spectroscopy, at negative and positive voltage bias respectively. A bias voltage is applied to the normal lead and differential conductance is measured through a tunnel barrier between the lead and the NW, giving a signal which is directly proportional to the DOS as a function of the bias voltage (b, d). (e), (h) A single QD level is included in the electrochemical potential diagram, for fixed negative and positive voltage bias on the lead. The energy of the QD level can be tuned using a gate voltage in the experiment, and the points labelled A, B, C and D in (e) and E, F, G, and H in (h) represent resonance condition points at which the level is on resonance with the normal lead, the superconducting coherence peak, the ABS in the NW, and zero bias. A sketch of the Coulomb diamond features expected in bias spectroscopy for these configurations are shown in (f) and (i). Slices through the Coulomb diamond are sketched at finite negative (g) and finite positive (j) bias, with special points marked to illustrate the action of the spectrometer.

through a tunnel barrier, for negative and positive voltage bias respectively. In this case, a measurement of the DOS can be performed by varying the bias voltage applied to the normal lead, and recording the differential conductance. Fig. 7.2(b, d) shows an example sketch of the differential conductance that would be measured in such a setup, for the case of one state being present in the NW at finite bias. In contrast to this method, when using the QD as a spectrometer the bias on the normal lead can be kept at a constant value [Fig. 7.2(e, h)] and a single level of the QD can instead be swept experimentally by adjusting a gate, preferably one which has a strong lever arm to the QD. A sketch of the current which would be measured through such a system, again for the case of one state at finite bias inside a superconducting gap, is shown as a function of the potential of the QD level and the bias on the normal lead [Fig.7.2(f, i)]. The role of the bias on the normal lead is to determine the energy window for the spectroscopy measurement. Panel (g) Shows a sketch of the current along the fixed bias line denoted by the purple arrow in panel (f). Points of source-drain bias V_{SD} , the QD potential μ_{dot} , and the DOS in the NW are denoted by A, B, C, D going from high to low μ_{dot} . Before reaching point A, the QD energy level is above the energy of the normal lead, so there is no tunnelling through the system and the measured current is zero. At point A, the QD level is resonant with the lead. Tunnelling becomes possible and a finite current proportional to the above-gap DOS switches on. At point B the QD level is resonant with the coherence peak of the induced superconducting gap, so a corresponding peak is observed in the measured current, and similarly at point C the peak corresponding to the finite bias state in the NW is observed. At point D, the QD level moves below the Fermi energy, so the measured current of electrons into the device vanishes once again. To measure the other half of the DOS, one needs to fix the bias at an equal magnitude but opposite sign [Fig. 7.2 (h)].

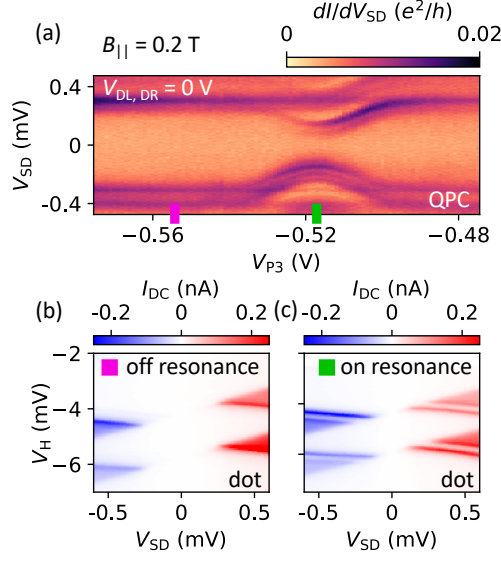


Figure 7.3: (a) Tunneling spectroscopy at $B_{||} = 0.2$ T as a function of the NW plunger gate voltage V_{P3} . A sub-gap state can be seen around -0.52 V. (b) Current measured through the weakly coupled QD when the gate voltage V_{P3} is set far away from the sub-gap resonance, indicated by a magenta square. (c) Current through the same two QD levels with V_{P3} set to the location of the sub-gap state energy minimum, indicated by a green square.

In this case, the current will flow in the opposite direction, which can be considered as an electron current with opposite sign, or a hole current into the device. The corresponding current along the fixed bias line denoted by the orange arrow in (i) is sketched in (j).

Experimentally, we observe a small splitting of all features in tunneling spectroscopy in a window of ~ 50 mT around zero $B_{||}$. This splitting can be seen close to zero field in Fig. 7.1(c, d). The cause of this is not clear, but we suspect it may be due to spin-orbit effects in the normal 2DEG leads. Because of this, for clarity, we demonstrate the low field action of the QD spectrometer at a small parallel magnetic field of 0.2 T (away from the split features) instead of at zero field. Although there is some Zeeman splitting at this field value, the splitting of the QD levels is still small compared to the width of the DOS features measured, and the splitting of the superconducting gap and any sub-gap features is almost negligible. Using

the QPC with the D and H gates set to 0 V, tunnelling spectroscopy on Probe 3 is measured [Fig. 7.3 (a)] while sweeping the gate voltage V_{P3} , which changes the density in the NW segment underneath it. A local state in the NW can be seen coming out of the continuum and into the gap, with a minimum at around -0.52 V. At V_{P3} values above and below the state resonance, there is a hard induced superconducting gap without sub-gap states. To demonstrate the action of the QD spectrometer at low applied magnetic field, a weakly coupled QD is formed by depleting with the D and H gates. We show Coulomb diamonds measured at two values of V_{P3} : one at which there is no state inside the induced superconducting gap (-0.53 V, shown in Fig. 7.3(b)) and one at which the state in the NW reaches an energy minimum (-0.5 V, shown in Fig. 7.3(c)). These gate voltages are marked with colored boxes (magenta and green, respectively), which correspond to the colored markers in Fig. 7.3(a). The voltage values are not in one-to-one correspondence with the green and magenta boxes because the gates used to confine the QD have some capacitive coupling to the state in the NW, so turning on the QD spectrometer shifts the state slightly in V_{P3} space. For both cases, the Coulomb diamond structure looks as expected from our description of the sequential tunnelling path through the lead-QD-NW system. The absolute value of the dc current is non-zero only when an energy level of the QD falls in between the applied bias voltage V_{SD} and the Fermi level, so that the window in which spectroscopy is possible (which we refer to as the 'bias window') increases with increased magnitude of V_{SD} . The current disappears again around zero bias, causing the tips of the diamonds to be shifted away from each other, because the drain (the hybrid NW) is gapped in this energy range. The measured current is positive when V_{SD} is below 0 V, so in this configuration electrons flow into the device, and negative when V_{SD} is above 0 V, corresponding to electrons flowing out of the device (or

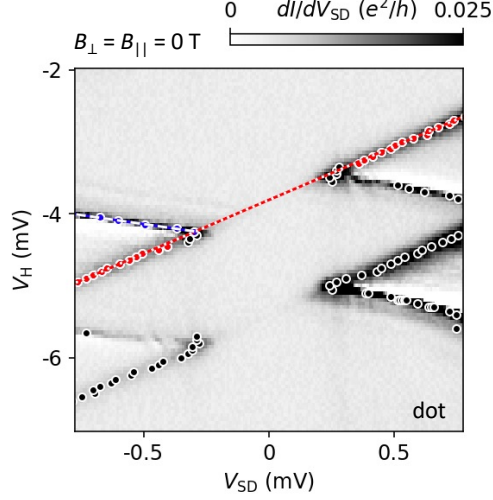


Figure 7.4: Illustration of the extraction of gradients for calculation of the gate lever arm, shown for two Coulomb resonances that were used for QD spectroscopy. All scatter points plotted correspond to peaks identified at the Coulomb diamond edges found using the `scipy find peaks` function. The black points are not used in the lever arm calculation, while the red and blue points are used in straight line fits to extract the slopes m_1 and m_2 respectively.

conversely holes flowing in). This demonstrates the action of the single QD levels as charge filters¹³⁷.

An additional feature is seen in Fig. 7.3(b) when compared to Fig. 7.3(c); this corresponds to the ABS resonance. The NW DOS information can be accessed more quantitatively by considering a 1D line cut through a Coulomb diamond at fixed bias, changing the energy of the QD by gating. The gate voltage scale is converted to energy using the gate lever arm, which is extracted from high-resolution differential conductance measurements of the Coulomb resonances by finding the slopes of both edges of the Coulomb diamonds, as shown in Fig. 7.4. The slopes m_1 (red points) and m_2 (blue points) are combined to give the lever arm, $\alpha = 1/(m_1 - m_2)$. For this set of resonances, $\alpha = 0.502$. The current measured is proportional to the DOS. Such 1D measurements showing the NW DOS at zero field are shown in Fig. 7.5(a) and (b) for the case of being on resonance and off resonance with the ABS in the

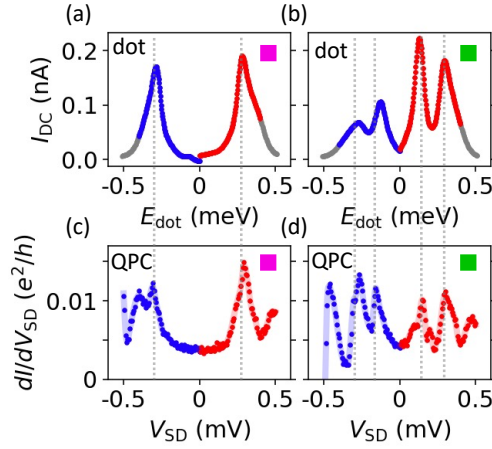


Figure 7.5: Line cuts through a Coulomb diamond at $V_{SD} = -0.4$ mV (blue) and $V_{SD} = +0.4$ mV (red) V_{SD} , showing the dc current, proportional to the density of states in the NW, as a function of the energy E_{dot} . The x -axis was converted from V_H to E_{dot} using the gate lever arm α . Shown at zero applied magnetic field for (a) a hard gap and (b) for one ABS in the NW. (c) and (d) also show spectroscopy of the NW DOS in a hard gap region and for one ABS respectively, but measured via tunnelling spectroscopy, by varying V_{SD} and measuring differential conductance. For these differential conductance measurements, the gates which form the QD are set to 0 V, so there are no QD levels to consider in the measurement.

gap, respectively, at the same V_{P3} values as Fig. 7.3(b) and (c) as indicated by the color coding. The QD spectroscopy can be compared directly to QPC spectroscopy at corresponding V_{P3} values (Fig. 7.5 (c),(d)). In the case with no ABS, both the QD and the QPC measurements show superconducting coherence peaks at $\sim \pm 290 \mu\text{eV}$. The QPC measurement further shows additional features at higher voltage bias, while the QD spectroscopy measurement is cut off by the value chosen for the fixed bias of the lead (0.4 mV). When V_{P3} is adjusted so that an ABS comes down into the gap, the bound state energies can be read off using the QD spectrometer to be $\sim \pm 100 \mu\text{eV}$ in agreement with the QPC measurement.

7.4 SPIN-RESOLVED SPECTROSCOPY

The DOS inside the NW can be measured using a single QD level at low field, but this does not provide any information that could not be obtained by tunnelling spectroscopy, which is readily accessible in these devices. The advantage of measuring through a QD level becomes apparent when one applies a finite magnetic field parallel to the NW, of a magnitude strong enough that the Zeeman splitting of the QD levels is greater than the desired energy window for the measurement. In this regime, the current which flows through a spin-polarized QD level is itself spin polarized, so that measurements through levels of different spin polarization give spin-resolved DOS information. It is important to note that to interpret such measurements, one must keep in mind that there are multiple g -factors to be considered; that of the QD levels (g_{dot}) and those of the system which is being probed via the QD level, in this case the hybrid NW system.

A schematic illustration of the use of spin-split QD levels as spin-selective spectrometers is given in Fig. 7.6. Here, only a superconducting gap is considered, without the added complication of any sub-gap features. When a field is applied, Cooper pairs keep their momentum pairing, but the opposite spin components of the pair have different energy¹³⁸. Since the $1e$ excited states remain separated in energy by Δ from the paired state, the coherence peaks appear at different energies for different spins, and the edges of the gap therefore split with some g -factor g_{SC} . For bulk Al $g = 2$, but we can expect some modification of that in the hybrid system²¹. The sketch of the tunneling process through a barrier is shown in Fig. 7.6(a), where one can see an electron tunneling from a normal lead at negative voltage bias (not spin polarized) into the NW DOS (spin polarized). Since the normal lead and tunnel barrier are

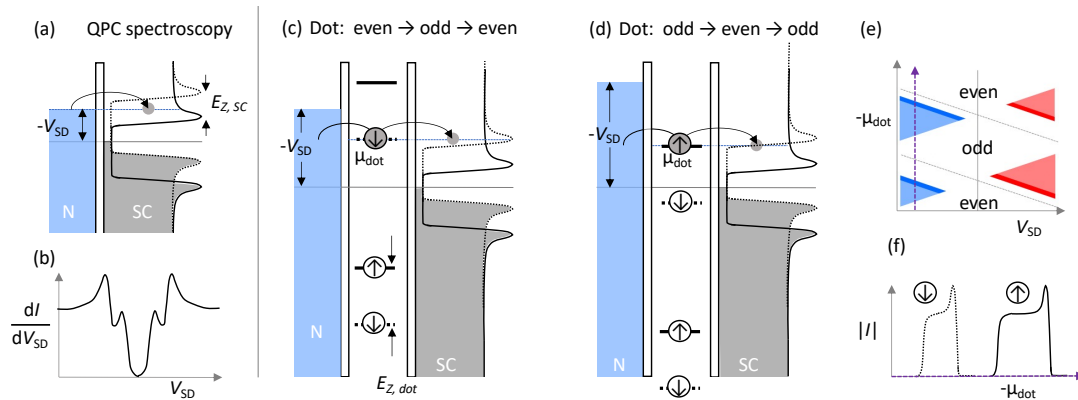


Figure 7.6: A schematic representation of the use of two consecutive levels of the QD for spin resolved spectroscopy at finite field. (a) Sketch of the electrochemical potentials involved in standard tunneling spectroscopy when the AI DOS is spin-split by $E_{Z,SC}$ due to the Zeeman effect. (b) The resulting differential conductance signal, sketched as a function of bias voltage. Spin-up and spin-down parts of the NW DOS are observed together. (c, d) Schematic of spin filtered tunneling current through a QD with levels which are split by the magnetic field, for even and odd filled ground states respectively. This results in a spin-down polarized current in the case of an even ground state, and a spin-up in the case of an odd ground state. (e) Sketch of the Coulomb diamond features for two consecutive levels expected as a function of V_{SD} for this configuration, with an asymmetry arising from the spin-splitting of the DOS and the spin polarized transport. (f) A slice through the two Coulomb diamonds at finite negative bias, showing separate spectroscopy of the spin-down and spin-up components of the NW DOS.

indifferent to spin, both spin-up and spin-down electrons can tunnel into the NW at a given V_{SD} , and the resulting differential conductance signal is the total DOS (spin-up and spin-down components added together [Fig. 7.6 (b)]). The peaks which correspond to the spin-up and spin-down coherence peaks are still visible in the signal, but the two components are combined. To separate them, the tunneling current has to be spin filtered. This can be done by utilizing the QD as a spin selective barrier, tunneling through a single QD level which is spin-polarized, as in Fig. 7.6(c, d).

As a magnetic field is applied, the levels of the QD will split with $g = g_{dot}$, so the energy required to add a spin-up electron reduced in field, while the energy to add a spin-down electron to the same orbital increases. For the case of an even number of electrons N on the QD, the most energetically favorable way to add another electron to the system is to load a spin-up electron into the next available level, so a spin-up current will predominantly flow. However, at low fields, the spin-down excited state is also accessible, so some transport through the first excited state will also be observed when both of the spin-split level components are within the voltage bias window. When the Zeeman splitting becomes larger than the selected bias window, the excited state is no longer available for transport, and the QD acts as a spin filter with no additional channels for the opposite spin. For the case shown in Fig. 7.6 (c), the excited state is already outside the bias window. Conversely, for the case of an odd number $N + 1$ electrons on the QD [(d)], the lower (spin-up) energy level is already filled by the $(N + 1)^{th}$ electron, so the most energetically favorable transport option is to load a spin-down electron. The next excited state is much higher up in energy, so in the bias ranges which are used in this experiment the odd-even transition transport does not show any excited states. In this configuration, transport through two consecutive levels of the QD appears different at finite

applied magnetic field; the even-odd transition filters spin-up electrons, but also shows transport through an excited state at lower fields, while the odd-even transition filters spin-down electrons. Figure 7.6 (e) shows a sketch of the current one can expect to measure through two such consecutive transitions, at a field where the Zeeman splitting of the QD is greater than the voltage bias range, $E_{Z,\text{dot}} > eV_{\text{SD}}$, so that no excited state transport is visible. A variation is expected in the size of the diamond tips, because the gap edge measured by one level (spin-down) is lower in energy than the edge measured by the other (spin-up). This can be visualized more directly by taking a 1D cut at finite bias through the two levels, as shown in (f). The rightmost edge of each resonance corresponds to the bias edge, where the QD level comes on resonance with the normal lead and sequential tunneling turns on. This feature is always at a fixed energy, as it is simply determined by the bias chosen for the measurement. This switching on is followed by a current that is proportional to the DOS; first a plateau above the gap energy, and then a peak in current which corresponds to the coherence peak. Note that the distance between the bias edge and the coherence peak is different for the spin-up and spin-down resonances; this is because the spin-up and spin-down components of the DOS are resolved separately with the two different QD levels. The spin-up and spin-down components of the DOS are split, and the difference between the energy of their peaks is given by $E_{Z,\text{SC}}/\alpha$.

Experimentally, we find that in device 1 the QD level even-odd pairs which are suitable for spectroscopy exhibit a g -factor of ~ -8.5 . This means that at an applied parallel field of 0.6 T, the corresponding Zeeman splitting is $E_{Z,\text{dot}} \sim 295 \mu\text{eV}$, so that features below that energy can already be spin-resolved by the QD spectrometer, but excited states of the QD still appear at higher biases. Measurements taken at this field value are shown in Fig. 7.7. A

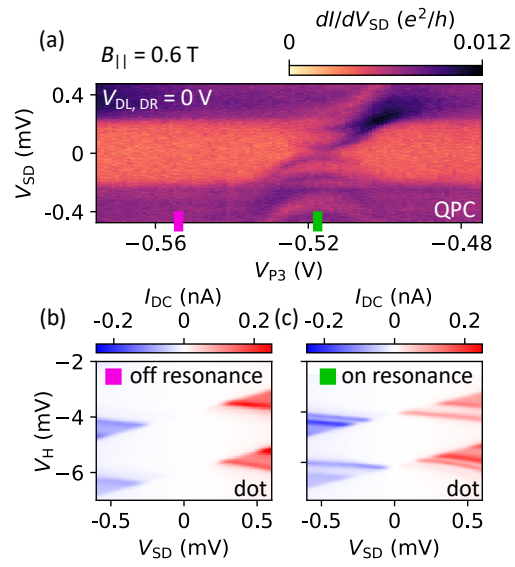


Figure 7.7: (a) QPC tunneling spectroscopy at $B_{||} = 0.6$ T, measured as a function of the V_{P3} . The sub-gap state seen around -0.52 V is visibly spin split at this field value - four resonances are seen inside the gap instead of the two observed at low field. (b) Current measured with the QD formed, through two consecutive levels of the QD when V_{P3} is set far away from the sub-gap resonance (magenta) (c) Current through the same two levels of the QD with V_{P3} set to the location of the sub-gap state energy minimum (green).

tunnelling spectroscopy scan over NW potential (tuned by V_{P3}) in Fig. 7.7 (a) shows a gap, reduced from the lower field value as expected, but with no visually resolvable splitting. The same sub-gap state as seen in Fig. 7.3 is also visible here, now split so that one component has moved towards zero energy while another has almost retreated into the continuum. Sequential tunneling current measured through the same two consecutive QD levels as in Fig. 7.3 is shown in Fig. 7.7(b, c) for V_{P3} values that bring the sub-gap state away from and onto resonance, respectively. An enhancement in current magnitude is seen in the bottom corner of the top left diamond tip in Fig. 7.7 (b) (and equivalently in the top left corner of the bottom right diamond tip). These are signatures of the excited spin-down state, appearing at higher bias as expected. On resonance with the sub-gap state [Fig. 7.7 (c)] the top right and bottom left diamond tips are notably larger than the other two. We interpret that this is due to their transport of spin-down electrons and corresponding spectroscopy of the spin-down part of the NW DOS, in this case measuring directly the part of the sub-gap state which moves towards zero energy. Additional resonances appear in the spin-up filtering diamond tips (top left and bottom right) due to spin-down transport via the spin-down excited state.

Measuring the dc current through the QD as a function of bias to see Coulomb diamonds is useful for confirming the behavior of excited states of the QD and extracting lever arms. However, to use a QD level as a tool for spin resolved spectroscopy and gain more insight to the DOS in the NW, it is sufficient to measure at a fixed voltage bias on the normal lead. To examine directly the splitting of the superconducting gap in the absence of sub-gap states (off resonance) in field using the QD levels, the bias is fixed at +0.4 mV, so that spectroscopic measurements can be taken via the two consecutive QD levels with a constant bias window. This can be thought of as taking a slice through Fig. 7.7(b) at $V_{SD} = +0.4$ mV, and then

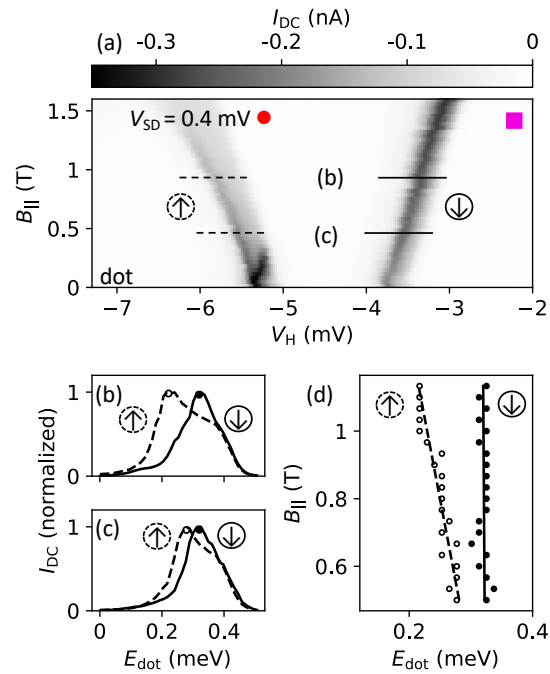


Figure 7.8: Spin resolved tunnelling current into the hard gapped superconductor (a) Current through two consecutive levels of the weakly coupled QD at finite V_{SD} measured as a function of $B_{||}$. The levels move in opposite directions as the field is increased, indicating their opposite spin character. 1D slices through the left (solid line) and right (dashed line) resonances for 0.5 T (c) and 1 T (b), with the horizontal axis converted from gate voltage to energy. (d) Energy values of the coherence peaks of the spin-up and spin-down components of the DOS (extracted from the left and right resonances respectively) plotted as a function of $B_{||}$ with linear fits.

ramping the parallel magnetic field up from 0 T. This measurement is shown in Fig. 7.8(a). Here, the result is a combined effect of two separate g -factors; the QD energy levels shifting in magnetic field, and the superconducting DOS evolving in field. The two consecutive QD states (transport through spin-up and spin-down ground states, respectively) move apart in field, and the previously discussed excited state can be seen as a high magnitude signal at low field in the left (spin-up) QD level. It splits rapidly in the opposite direction to the movement of the ground state. This motion of the QD levels does not provide any information about the NW DOS, and must be compensated for in the analysis. This compensation is possible because, as emphasized before, the bias edge of each resonance, where the current switches on because the QD level is on resonance with the normal lead, always corresponds to the same energy. So the position of the bias window in V_H space shifts in field, but the bias window remains the same. At each field value, the bias edge point is used as an anchor, so that when we convert the V_H axis from gate voltage to energy each one of the two resonances has a 0.4 meV point, with respect to which a zero energy can be defined. Due to broadening of the QD levels, caused by finite temperature and finite coupling, the current does not go to zero instantaneously at the bias edge point and so the point itself is not perfectly defined. In this analysis, the placement of the bias edge for each resonance was determined by taking the V_H at which the current reached half of its peak value. This way, the method is standardized for each resonance, so relative energy values should be consistent with each other. The result of performing this analysis for each line of the measurement is that for each field value, one acquires two traces that are proportional to the DOS in the NW between 0 and 0.4 meV, one for the spin-up and one for the spin-down component of the NW DOS. This is shown explicitly in Fig. 7.8 (b) and (c) for the field values of 1 T and 0.5 T respectively, with the

normalized current traces for spin-up and spin-down plotted together in each case. At 0.5 T there is a small splitting between the spin-up and spin-down coherence peaks, while at 1 T the splitting is more significant. In Fig. 7.8(d) the peak energies extracted in a similar manner are plotted as a function of field, for values up to 1.1 T (starting at 0.5 T, so that the excited state is already outside the bias window). By linear fits, the g -factor for the splitting of the gap is calculated to be ~ 1.7 . This is slightly lower than $g_{Al} = 2$. This may be explained by the re-normalization of the hybrid system g -factor due to the hybridization at the interface of the thin Al film ($g_{Al} = 2$) and the InAs ($g_{InAs} = -15$)²¹. Note that the spin-up peak splits more rapidly towards zero energy than spin-down splits away; this might be explained by the effect of spin orbit interaction¹³⁸. A similar analysis was performed for the negative bias side, where an electron current flows into the device instead of a hole current, showing a similar g -factor.

In the regime described above, one is able to separately measure the spin components of the spin-split superconducting gap in the NW, with no sub-gap features involved. If V_{p3} is adjusted, the spin-resolved field dependence of the previously shown sub-gap state can be investigated. Looking back at the tunneling spectroscopy measurement of this dependence in Fig. 7.1(d), it can be observed that the bound state splits in applied parallel magnetic field, with one component moving away from zero energy and merging into the continuum just above 1 T, and the other moving towards zero energy before anti-crossing at around 1 T. By measuring via the two spin-selective QD levels, as with the gap splitting above, these different features of the state transport can be observed with spin resolution. For this purpose, it can be useful to record differential conductance as well as the dc current through the QD level. Although for sequential current measured through a weakly coupled QD level it is the dc cur-

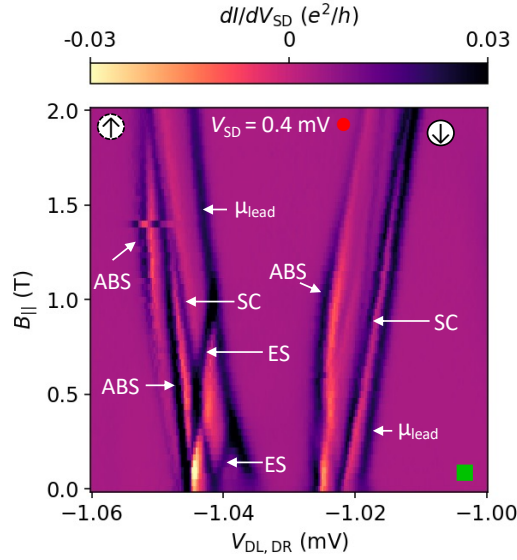


Figure 7.9: Differential conductance through two consecutive levels of the weakly coupled QD at finite V_{SD} measured as a function of $B_{||}$, with V_{P3} set so that the sub-gap state in the NW is on resonance (indicated by the green square). Features corresponding to different spin components of the state (ABS) and the spin-split gap coherence peaks (SC) are indicated, as well as resonances arising from excited states of the QD itself (ES).

rent which is proportional to the DOS in the NW, a differential conductance measurement will (by definition) show a clear signal at points where the current undergoes a change as a function of V_{SD} , so both peaks and regions of rapid change (such as the bias edge) are highlighted. Such a measurement is shown in Fig. 7.9, with V_{P3} set to the value at which the sub-gap state reaches a minimum at low field. Each bright resonance is labelled with the transport feature which it corresponds to, according to our interpretation. The rightmost resonances of both levels, labelled ' μ_{lead} ', correspond to the bias edge, where the QD level energy is on resonance with the normal lead, and the current switches on. The two resonances labelled 'SC' correspond to the coherence peaks, for spin-up and spin-down respectively. Here, as before, it is important to make the distinction between the effect of the magnetic field on the NW DOS, which is being measured through the QD levels, and the movement of the lev-

els themselves in field, which does not depend on the NW but purely on the QD. As in the analysis above, the splitting of the SC gap edges in field is not determined from the absolute movement of the ‘SC’ resonances, but from their movement relative to their respective bias edge. The spin-up ‘SC’ resonance moves away from the bias edge, towards zero energy, while the spin-down moves towards its respective bias edge, splitting away from zero energy.

Consider now the resonances caused by the NW state components, labelled ‘ABS’. At lower field ($B_{\parallel} < 0.8$ T), a bright feature labelled ‘ABS’ seen via the spin-down QD resonance moves away from the bias edge, and towards zero energy. This is in contrast to the spin-down ‘SC’ component, which moves towards the bias edge. This observation suggests that the bound state and the gap edge have g -factors of opposite sign, a property which is not observable with standard tunneling spectroscopy. The ‘ABS’ component which splits in the opposite direction, away from zero energy, is observed via the spin-up resonance. Using a lever arm $\alpha = 0.043$, the two spin components of the ABS appear to split with a $g_{\text{ABS}} \sim -2.25$ at low field. This is plausible, considering again that the g -factor of the hybrid system is re-normalized by the hybridization between the Al and InAs, and that the effective g -factor for the bound state depends on the strength of this hybridization²¹. Two resonances labelled ‘ES’ appear due to transport via the spin-down excited state of the QD. As the field approaches 1 T, the ABS feature which splits towards zero energy starts to fade in magnitude as measured via the spin-down level, and simultaneously appears via the spin-up resonance. After 1 T it appears more brightly on the spin-up side than on the spin-down. This indicates a change in the ground state of the ABS component, as it goes from transporting primarily spin-down current to spin-up. Note that this change is not abrupt, it is a gradual transition.

7.5 SPIN AND CHARGE POLARIZATION OF TUNNELING CURRENT

This gradual transition between transport of spin-up to transport of spin-down electrons via the bound state, which is resolved by measuring spin-up and spin-down current separately using the Zeeman split QD levels, can be quantified by defining a spin polarization of the transport through the state. Measuring at negative voltage bias on the lead, the electron components of the transport current are accessed, so using two consecutive levels, one accesses separately the spin-up, electron component and the spin-down, electron component of the DOS. Similarly, by measuring at positive voltage bias, a hole current flows, and the spin-down, hole and spin-up, hole components are resolved. These four separate components are labelled explicitly in Fig. 7.10(b) and (c). We define a spin polarization S by comparing the magnitude of the current into the state of interest as measured via the spin-up and spin-down components. Separate polarization quantities can be extracted for the electron and hole measurements;

$$S_u = \frac{I_{\downarrow,u} - I_{\uparrow,u}}{I_{\downarrow,u} + I_{\uparrow,u}} \quad (7.1)$$

$$S_v = \frac{I_{\downarrow,v} - I_{\uparrow,v}}{I_{\downarrow,v} + I_{\uparrow,v}}. \quad (7.2)$$

The electron and hole components can then be combined to define a total spin polarization

$$S_{total} = \frac{I_{\downarrow,u} - I_{\uparrow,u} + I_{\downarrow,v} - I_{\uparrow,v}}{I_{\downarrow,u} + I_{\uparrow,u} + I_{\downarrow,v} + I_{\uparrow,v}}. \quad (7.3)$$

In a similar manner, a particle-hole polarization Q can be defined by combining the relevant current magnitudes, yielding:

$$Q_{\downarrow} = \frac{I_{\downarrow,u} - I_{\downarrow,v}}{I_{\downarrow,u} + I_{\downarrow,v}}. \quad (7.4)$$

$$Q_{\uparrow} = \frac{I_{\uparrow,u} - I_{\uparrow,v}}{I_{\uparrow,u} + I_{\uparrow,v}}. \quad (7.5)$$

$$Q_{total} = \frac{I_{\downarrow,u} + I_{\uparrow,u} - I_{\downarrow,v} - I_{\uparrow,v}}{I_{\downarrow,u} + I_{\uparrow,u} + I_{\downarrow,v} + I_{\uparrow,v}}. \quad (7.6)$$

Using these definitions, the evolution of the spin and charge character of a bound state can be tracked with respect to a parameter like magnetic field or gate voltage. In Fig. 7.10, V_{P3} is set so that the previously investigated bound state is on resonance, and the four tunnelling current components ($I_{\downarrow,u}$, $I_{\uparrow,u}$, $I_{\downarrow,v}$ and $I_{\uparrow,v}$) are measured via two consecutive QD levels as before as B_{\parallel} is increased [Fig. 7.10(b, c)]. The spin and charge polarization are extracted from this data for the lowest energy ABS component, which is tracked using the `scipy` peak finder function. If a peak cannot be identified because it is below the noise level, the magnitude contribution is set to zero. The results of the extraction are shown in Fig. 7.10(d) for spin, including the separate electron and hole components and the total value, and in Fig. 7.10(e) for the total charge polarization. At low field, the current into the state is strongly spin-down polarized. In tunnelling spectroscopy (shown in Fig. 7.10(a) for comparison to the QD measurements) the state splits towards zero energy linearly, and in the QD measurements is observed almost exclusively through the spin-down filtering resonances. As the state approaches zero energy, an anti-crossing is observed in tunnelling spectroscopy. This point, marked with the middle dashed line in Fig. 7.10, also marks the point where the currents

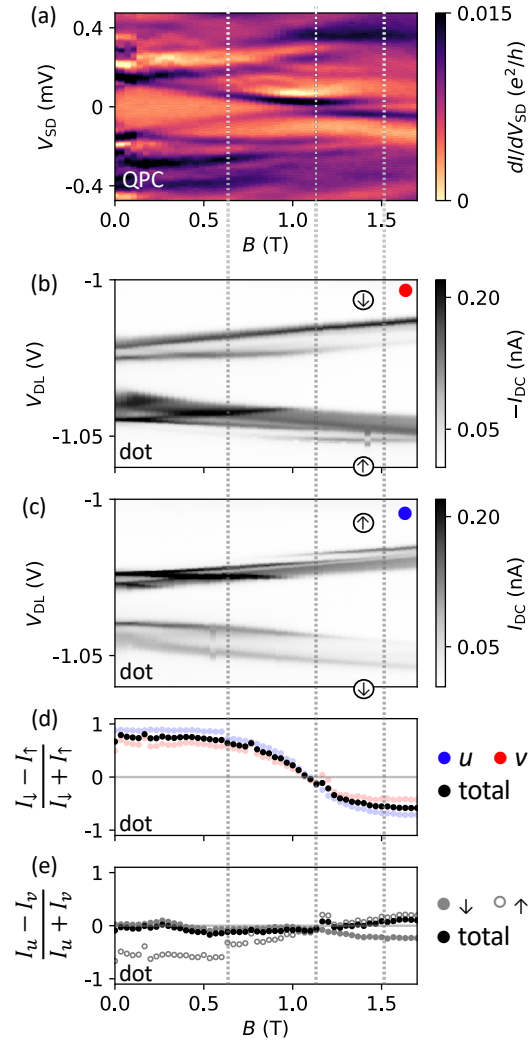


Figure 7.10: Resolving the spin and charge character of a NW state while varying B_{\parallel} . (a) Tunneling spectroscopy measurement of a localized NW state under the gate P3 for increasing B_{\parallel} . The gates which form the QD remain at 0 V during this measurement. (b, c) Sequential tunnelling spectroscopy through two consecutive levels of the QD, with V_{SD} fixed at $-400 \mu\text{V}$ and $+400 \mu\text{V}$ respectively. The current through the two QD levels is spin polarized due to the Zeeman effect, so that the spin-up and spin-down components of the NW DOS are measured separately. Comparing the magnitudes of the current through the spin-up and spin-down resonances allows for the extraction of the spin polarization S of the tunneling current (d), which crosses through zero around 1 T, the field at which an anti-crossing around zero bias is observed in the QPC measurement. (e) Comparing the magnitudes at positive and negative V_{SD} leads to a measure of electron-hole polarization of the current, which at this V_{P3} value stays close to zero for the entire field range.

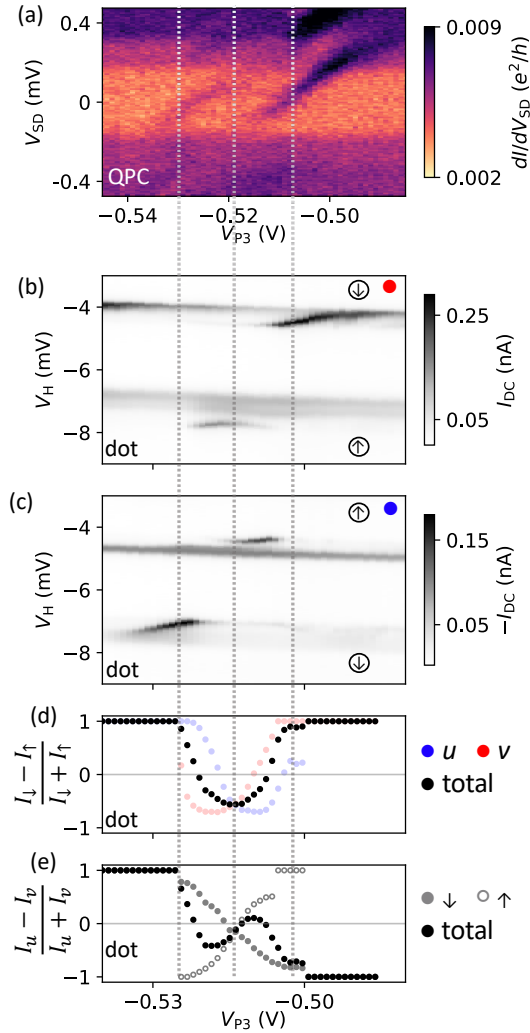


Figure 7.11: Resolving the spin and charge character of a NW state while varying gate voltage at an applied magnetic field of 1.4 T. (a) Tunneling spectroscopy measurement of a localized state under the segment of NW tuned by gate P3 for varying V_{P3} . The gates which form the QD remain at 0 V during this measurement. (b, c) The effect of the NW gate voltage variation measured instead using sequential tunnelling spectroscopy through two consecutive levels of the QD, with V_{SD} fixed at $-400 \mu V$ and $+400 \mu V$ respectively. The current through the two QD levels is spin polarized due to the Zeeman effect, so that the spin-up and spin-down components of the NW DOS are measured separately. (d) Spin polarisation S of the tunnelling current as a function of gate voltage. Comparing the magnitudes at positive and negative V_{SD} leads to a measure of charge polarization Q of the state (e).

measured through the spin-up and spin-down filtering QD levels and the lowest energy state are equal, leading to a net zero spin polarization.

Above the anti-crossing, the current measured through the spin-down filtering levels decays away, and the lowest energy state is mostly observed via the spin-up filtering level. Correspondingly, the spin polarization, having gone through zero at the point of anti-crossing, switches to negative values (spin-up polarized). We interpret that the spin polarization of the current reflects the spin polarization of the ABS. This crossing through zero is then consistent with a transition of the ABS in which the spin of the ground state switches in field^{44,45}. The charge polarization is also extracted (e); this appears to remain around zero for the entire field range, indicating that at the chosen gate voltage V_{P3} the DOS is equal parts electron and hole.

This transition is further investigated by applying a fixed $B_{||}$ of 1.4 T, above the field at which the anti-crossing is observed, and changing the chemical potential by sweeping V_{P3} . This measurement is shown for the same state as before in Fig. 7.11, with a tunnelling spectroscopy measurement shown for comparison (a) and the four spin/charge components measured through the QD levels (b, c). For these data, the spin and charge polarization of the transport through the lowest energy ABS are extracted in the same way as before, by peak-finding to track the energy of the state and taking the magnitude of the peak for each component $I_{\downarrow,u}$, $I_{\uparrow,u}$, $I_{\downarrow,v}$ and $I_{\uparrow,v}$. In the tunnelling spectroscopy measurement, the state is observed to cross twice through zero energy, undergoing a characteristic singlet to doublet transition⁴⁴. The switching of the ground state spin is directly seen from the spin polarization [Fig. 7.11 (d)]. The charge polarization dependence on the chemical potential is also nontrivial; this quantity crosses through zero three times, including once in the center of the doublet

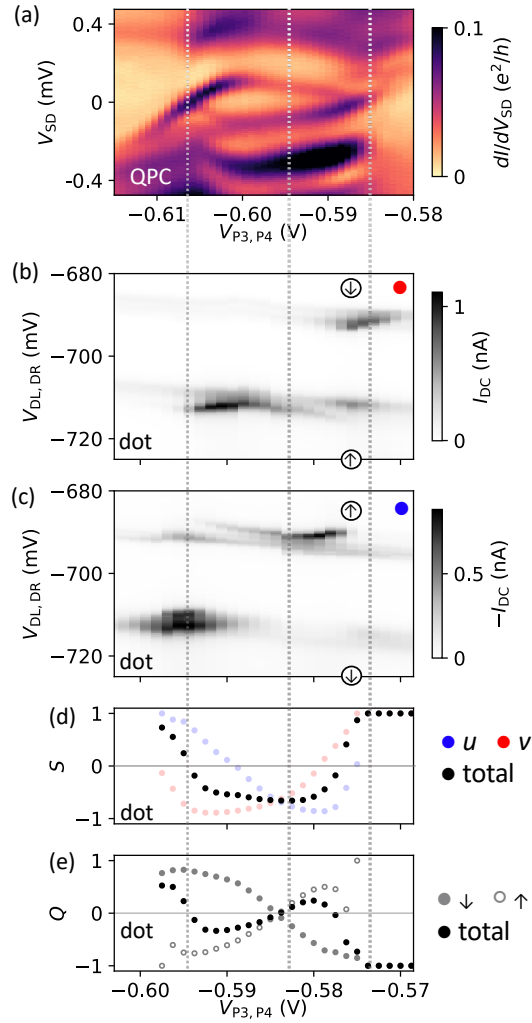


Figure 7.12: Resolving the spin and charge character of a NW state in device 4 while varying the gate voltage at an applied magnetic field of 0.6 T. (a) Tunneling spectroscopy measurement of a localized NW state under the gate P3 for varying V_{P3} . The gates which form the QD remain at 0 V during this measurement. (b, c) the effect of the NW gate voltage variation measured instead using sequential tunnelling spectroscopy through two consecutive levels of the QD, with V_{SD} fixed at $-400 \mu\text{V}$ and $+400 \mu\text{V}$ respectively. The current through the two QD levels is spin polarized due to the Zeeman effect, so that the spin-up and spin-down components of the NW DOS are measured separately. Comparing the magnitudes of the current through the spin-up and spin-down resonances allows for the extraction of a spin polarization quantity as a function of gate voltage i.e. chemical potential (d). Comparing the magnitudes at positive and negative V_{SD} leads to a measure of charge polarization of the state (e).

region. This is the chemical potential at which the magnetic field dependence was shown in Fig. 7.10. The charge polarization dependence is consistent with the Bardeen-Cooper-Schrieffer (BCS) charge quantity extracted from non-local conductance measurements of similar sub-gap states⁸⁷. A similar data set, in which gate voltage is swept and the spin and charge polarization quantities of the transport through a local bound state are extracted from dc current measured via two consecutive QD levels, is shown in Fig. 7.12. This data is taken on a different device to the data shown in the rest of the paper, device 4, which is structurally similar to device 1. While the state under investigation looks quite different, exhibiting a much higher g -factor, the core features extracted from the data show a clear similarity to the observations from device 1. This is true for the general behavior in energy, as well as the behavior of the spin and particle-hole polarization.

A more detailed look at the polarization behavior as a function of gate voltage in device 1 is provided in Fig. 7.13, where the spin and charge polarizations of the tunneling current are shown for gate voltage sweeps at three different applied magnetic fields. In Fig. 7.13 (a, b) we see the same data as in Fig. 7.11, at $B_{||} = 1.4$ T, but this can now be contrasted with the data at 1.2 T [Fig. 7.13(c, d)] and 0.8 T [Fig. 7.13(e, f)]. It is observed that as the applied field is decreased, the region in gate voltage in which the spin polarization of the current is reversed and the charge polarization oscillates becomes smaller. This is in accordance with the expected reduction of the doublet ground state region in the singlet to doubled transition⁴⁴.

7.6 DISCUSSION

We have demonstrated the use of single QD levels to directly measure the DOS of a hybrid superconductor-semiconductor NW. For a QD in which the level spacing is larger than the

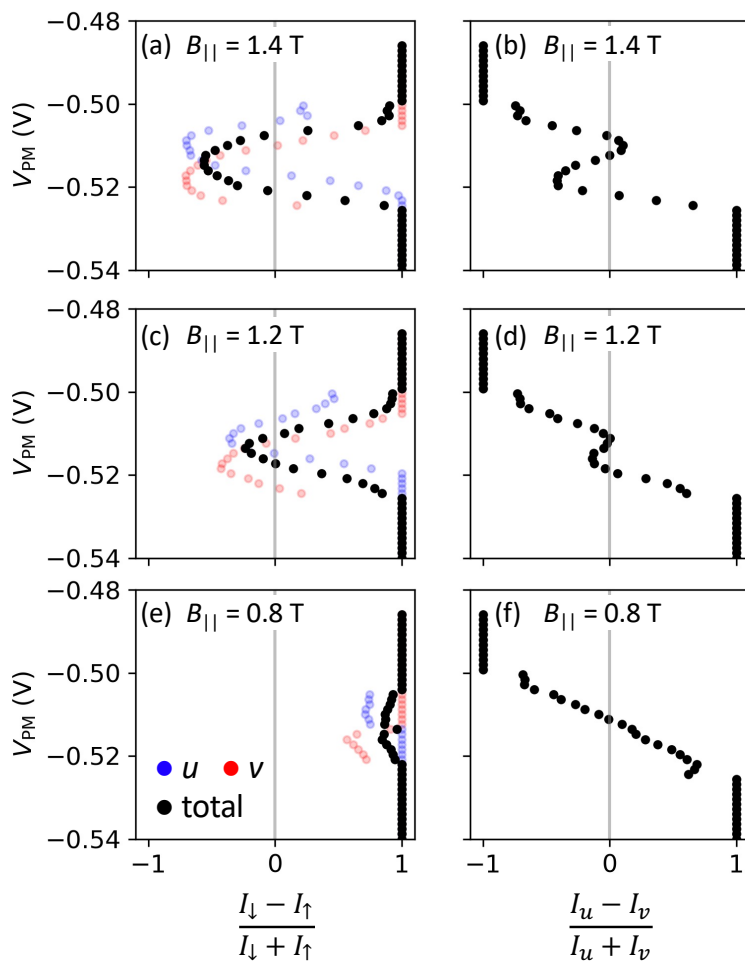


Figure 7.13: Resolving the spin and charge character of a NW state in device 1 while varying chemical potential varying parallel magnetic fields. Comparing the magnitudes of the current through the spin-up and spin-down resonances allows for the extraction of a spin polarization quantity as a function of gate voltage i.e. chemical potential (a,c,e) for fields of 0.8, 1.2 and 1.4 T respectively, while comparing the magnitudes at positive and negative V_{SD} leads to a measure of charge polarization (b, d, f) of the state for each of the field values.

superconducting gap Δ and the g -factor $|g_{\text{dot}}| > |g_{\text{SC}}|, |g_{\text{ABS}}|$, Zeeman split QD levels of opposite spin character can be used to measure the density of states with spin and charge resolution. From these measurements, relative signs of g -factors can be determined, and spin and charge polarization quantities can be extracted.

Spin filtering using a laterally defined QD level which is tuned into an appropriate bias window has been suggested¹³⁹ and demonstrated¹³⁶ before in the context of spin qubits, where the lifetime of an excited spin state was investigated. QD levels have also been used as spectrometers in the sense of reading out the numerical value of a superconducting gap¹³⁰, and capacitive coupling considerations have been used to disentangle resonances in a Coulomb diamond caused by excited states of the QD itself from those which reflect the density of states in the leads¹³⁴. However, this work is the first to our knowledge to directly measure the evolution of the density of states of a hybrid system via a QD level at constant bias, and to use Zeeman splitting of the levels to access separately the spin-up and spin-down components of the density of states, and to resolve the relative sign of the g -factors of different spectroscopic features. Our spin polarization results are consistent with the physics of a singlet to doublet transition of an ABS⁴⁴, as well as with the BCS charge predicted theoretically⁷⁰ and extracted from non-local conductance measurements^{65,87}. The QDs used in this work are not few-electron QDs, as previously used for spin resolved tunnelling in 2DEG QDs¹⁴⁰. Instead, we use carefully selected levels of a many-electron QD which exhibit the desired filtering behavior in field, including splitting away from each other at low field, and the expected excited state behavior. This allows us to loosen the requirements on device design for future spin-filter QDs; it is not necessary to be able to deplete the QD fully to zero electrons, just to the point where there is a clear even-odd structure which can be taken advantage of.

Future work on the topic of sub-gap excitations in superconductor-semiconductor structures will benefit from this tool to separate the spin and charge components of the density of states, with the filtering properties coming as a very natural consequence of embedding a QD inside a tunnel probe. The deliberate definition of the QD in the design presented here has the added flexibility of allowing the QD to be turned off by setting all QD related gates to 0 V, so a direct comparison to standard tunneling spectroscopy is possible for any measurement. The gradual evolution seen in spin and charge polarization measurements hints at the strong spin orbit coupling present in the system¹⁴¹, and a combination of further experimental work with some theory could provide a new, direct method of extracting the spin-orbit coupling strength from spin and charge polarization quantities measured through a transition induced by field or chemical potential changes. Similar measurements could also be used to probe directly the inversion of the bulk bands at a transition point^{141,142}. In the current devices, we have so far only probed very local ABS features, which were accessible to only one probe at a time. However, similar structures have shown evidence of the presence of extended bound states⁸³. Spin resolved measurements taken on both ends of a bound state simultaneously could provide even more information about the spin orbit coupling in these hybrid systems.

8

ABS and frequency control in gatemon qubits

This work is not part of the main thesis project, but is included for completeness.

This chapter contains the data and text presented in the following manuscript:

Few-mode to mesoscopic junctions in gatemon qubits, by *Alisa Danilenko*, Deividas Sabonis, Georg W. Winkler, Oscar Erlandsson, Peter Krogstrup, and Charles M. Marcus.

WE INVESTIGATE A SEMICONDUCTOR NANOWIRE-BASED GATEMON QUBIT with epitaxial Al on two facets of the nanowire, allowing gate control of wire density. Two segments have the Al removed, one forming a Josephson junction, and the other operating as a transistor providing *in-situ* switching between dc transport and qubit operation. Gating the NW changes the bulk wire potential distribution, while gating the Josephson junction changes the number of junction modes. Both effects are revealed by the dependence of qubit frequency on parallel magnetic field. A detailed model of the wire and junction yields behavior consistent with experiment. In the multi-mode regime, fluctuations in qubit frequency are smaller than the universal prediction, consistent with previous measurements of fluctuating critical current.

Recent materials advances⁴ have lead to a new approach to Josephson qubit technology based on hybrid superconductor-semiconductor nanowires (NWs)^{143,144} and comparable two-dimensional platforms¹⁴⁵. This approach allows voltage control of qubit operation and reduced sensitivity to charge noise¹⁴⁶⁻¹⁴⁸. Hybrid NWs can also form the basis of Andreev qubits¹⁴⁹⁻¹⁵², protected $0 - \pi$ qubits¹⁵³, systems to investigate the presence of topological phases¹⁵⁴, and voltage-controlled qubit couplers¹⁵⁵. Because the electron wavelength in the semiconductor is comparable to the NW diameter, electronic states under the proximitizing superconductor typically occupy a small number of transverse modes¹⁵⁶. For NWs with facets not covered by the superconductor, this mode structure can be altered by electrostatic

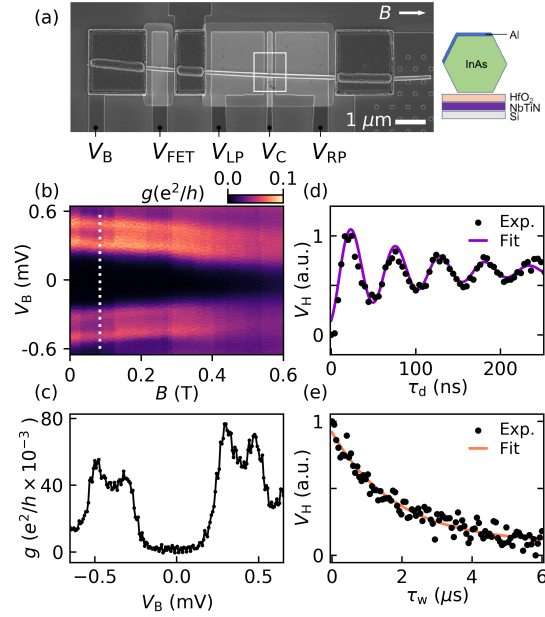


Figure 8.1: a) Scanning electron micrograph of Device 1 (cross section sketch on the right). The NW is contacted on the right to the ground plane, the capacitor island is connected in the center. The purpose of gate voltage V_C is to control the Josephson junction, while V_{LP} and V_{RP} are intended to tune the bulk wire. Direction of applied magnetic field B is shown. (b) Differential conductance $g \equiv \frac{dI_B}{dV_B}$ as a function of V_B shows the superconducting gap of the junction in applied field, with a cut (c) taken at $B = 0.08$ T. $V_{FET} = +6$ V, $V_{LP} = V_{RP} = 0$ V, $V_C = -3.6$ V. (d) Rabi oscillations at $B = 0$. Demodulated transmission V_H measured as a function of drive duration τ_d at the qubit frequency $f_Q = 4.37$ GHz. Exponentially decaying sinusoidal fit yields Rabi time $T_2^R = 119 \pm 1$ ns. (e) Qubit relaxation: V_H measured as a function of wait time τ_w between drive and readout pulses. The qubit is excited with a π pulse calibrated from (d). Exponential fit yields $T_1 = 1.81 \pm 0.13 \mu\text{s}$.

gating¹⁵⁷.

In this Letter, we compare the magnetic field and gate-voltage dependence of gatemon qubits fabricated from epitaxial InAs/Al NWs to a detailed numerical model of the wire and Andreev bound states (ABSs) in the junction¹⁵⁸. To gather parameters for the model, we take advantage of another feature of hybrid NWs by creating a local field-effect transistor (FET) that allows *in-situ* switching between dc transport and circuit quantum electrodynamics (cQED) configurations¹⁴⁶. Magnetic field and gate-voltage dependences of qubit frequency f_Q ¹⁵⁹ are in reasonable agreement with the model, and consistent with gate-voltage¹⁶⁰ and magnetic field dependences¹⁶¹ of critical currents in NW junctions, here measurable in the same qubit junction.

At gate voltages corresponding to several ABSs in the qubit junction, mesoscopic (random, repeatable) fluctuations of qubit frequency as a function of gate voltage were observed. Comparing experimental results with both numerics and theoretical universal statistics for mesoscopic critical current fluctuations¹⁶², we find that the observed qubit-frequency fluctuations, $\sigma_{f_Q} \sim 130$ MHz, corresponding to critical-current fluctuations $\sigma_{I_c} \sim 1$ nA, are smaller than theoretical values for a short junction¹⁶², though consistent with previous experimental values of critical current fluctuations¹⁶³. (Mesoscopic fluctuations of f_Q have not been reported previously, to our knowledge). We tentatively ascribed the reduced fluctuation of f_Q to non-ideal material interfaces^{163,164} or a Fermi velocity mismatch between the Al-covered region and the bare semiconductor junction¹⁶⁵ leading to normal reflection competing with Andreev reflection within the junction interfaces.

Devices were fabricated on a high-resistivity silicon substrate covered with a 20 nm NbTiN film, deposited by sputtering. Each chip contains three gatemons based on NWs, about 100

nm in diameter, with two or three of six facets covered with Al¹⁵⁹, two with FET-switched dc transport capabilities, each with individual resonator readout circuits. Resonators, transmission line, and electrostatic gates were fabricated using additional layers of sputtered NbTiN, patterned using electron beam lithography and reactive ion etching. Before placing the NW on the bottom gates, a lithographically patterned layer of HfO₂ dielectric was deposited by atomic layer deposition. A micrograph of one of the FET-switched devices is shown in Fig. 8.1(a). The right side of the NW connects to the ground plane, the left side to a dc contact through the FET, and the center to the qubit island. The Josephson junction, seen inside the white box in Fig. 8.1(a), is formed by wet etching ~ 100 nm of the Al shell. While the orientation of the shell is not discernible during manual NW placement, scanning electron micrographs taken afterwards can resolve the Al shell. Devices with the shell on the up-facing half of the NW, which allow control of carrier density in the NW by bottom gates, are then measured. Gate voltage V_C , underneath the junction, was used to tune f_Q , while voltages V_{LP} and V_{RP} were used to tune the density in the bulk NW. All measurements were performed in a dilution refrigerator with a base temperature of 20 mK using a 6-1-1 T vector magnet.

Setting the FET in the conducting state by applying +6.0 V on the FET gate, differential conductance $g \equiv dI_B/dV_B$ of the junction was measured as a function of voltage bias V_B . With the qubit junction in the tunneling regime, g can be used to measure the parent gap and ABS features in the semiconductor, as shown in Figs. 8.1(b, c). The two higher-bias peaks occur at the bias where coherence peaks from the Al gap, $\Delta \sim 250 \mu\text{eV}$, on the two sides of the junctions align, $V_B \sim \pm 2\Delta/e \sim \pm 0.5$ mV. The two lower-bias peaks reflect where the coherence peak in one lead aligns with a subgap ABS in the other lead. Extrapolating the field dependence of the gap gives a field of ~ 1.4 T where the gap closes. Following dc

transport characterization of the junction, the FET was switched to a non-conductive state (FET gate at -6 V) allowing the device to be operated in cQED mode as a qubit. Setting $V_C = -1.7$ V, $V_{LP,RP} = 0$ V gives a qubit frequency $f_Q = 4.37$ GHz, measured via two-tone spectroscopy. Rabi oscillations [Fig. 8.1(d)] were measured by applying a series of pulses of duration τ_d at f_Q and plotting the demodulated transmission V_H as a function of τ_d . Fitting to an exponentially decaying sinusoid yields a Rabi time of 119 ± 1 ns. Qubit relaxation [Fig. 8.1(e)] was measured by applying a π pulse, found using data in (d), at f_Q , then waiting τ_w before applying a readout pulse at the resonator frequency, 5.46 GHz, giving a V_H signal that decreases with increasing τ_w . An exponential fit yields a qubit lifetime of 1.81 ± 0.13 μ s. The dependence of f_Q on axial magnetic field B and gate voltage is shown in Fig. 8.2(a), for Device 2, which is similar to Device 1 in material and fabrication. For each value of $V_{LP,RP}$, V_C was compensated to keep the zero-field frequency constant, to try to minimise the effect of $V_{LP,RP}$ on the junction, since the aim was to tune the bulk wire density. This compensation had the added benefit of making sure that f_Q stayed in a measurable range at zero field. The changes made to V_C are very small compared to its full range of operation. In the measured field and frequency range, the qubit frequency decreased monotonically with increasing B . The solid lines in Fig. 8.2(a) are simple fits relating the qubit frequency to the square root of the closing of the superconducting gap in field, $f_Q(B) = f_Q(0) [1 - (B/B_c)^2]^{1/4}$, where B_c is the critical field at which the superconducting gap is projected to close¹⁰. As illustrated in Fig. 8.2(b), a trend in the dependence on $V_{LP,RP}$ was observed. The more positive the gate voltage applied to the NW, the more rapidly f_Q decays in field.

To understand the effect of the gate voltage configuration on the magnetic field dependence of qubit frequency, we perform numerical modeling of the energy spectrum and qubit

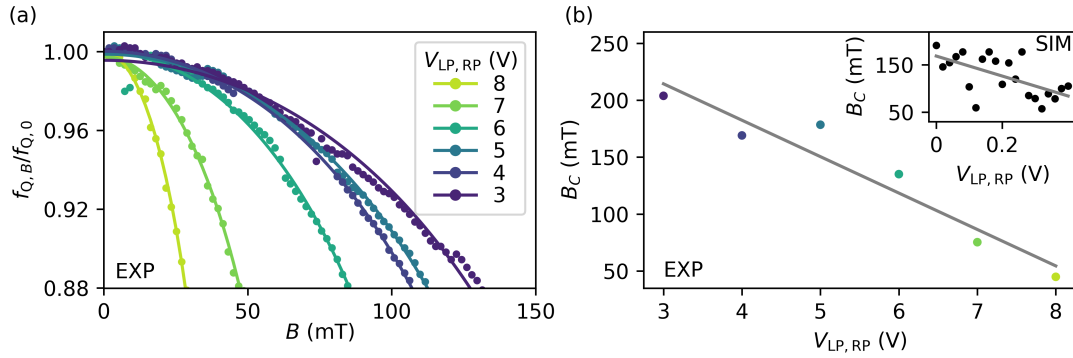


Figure 8.2: (a) Measured qubit frequency (normalized) as a function of parallel magnetic field B at a range of $V_{LP,RP}$ values. V_C was compensated to keep the zero field frequency constant for all gate configurations. (b) Critical field B_C , extracted from fitting the data for each gate configuration measured. Shown with a linear fit.

frequency using codes similar to Refs. ^{166–168} using a self-consistent Thomas-Fermi approximation, including Zeeman and orbital effects of the magnetic field, treating coupling of the superconductor to the semiconductor in terms of a self-energy boundary condition (see Supplementary Material). We find that the simulated qubit frequency follows roughly the quadratic decay of the parent gap for small fields, as observed in the experiment. Figure 8.2(b) inset shows the simulated dependence of B_C on the NW gate voltage. It should be noted that the lever arm in the simulation is much larger than in experiment, hence the significant difference in absolute gate voltage values. There is still a trend towards more rapidly decaying f_Q at more positive gate voltage in the simulation, but the numerical results are less monotonic than what we observe in the experiment. At more negative gate voltages, the wave function is pressed up away from the gates and close to the superconducting shell, and there is less wavefunction area for magnetic flux to thread through, leading to a more gradual decay of f_Q in field. We propose that the overall trend is due to the effect of gating the bulk of the NW, rather than a junction related observation.

We now examine an additional behavior observed at higher magnetic fields in Device 1. As

illustrated in Fig. 8.3(a), which shows experimental data, f_Q initially drops as in the previous data sets, leaving the experimental window at $B \sim 130$ mT. In this case however we observe a revival, such that a second local maximum of 4.3 GHz is reached at $B \sim 310$ mT, before another rapid decrease takes the frequency once more out of the experimental window.

Figures 8.3(b-d) show the simulated junction electrostatic potential, field-dependent spectrum, and qubit frequency for a gate configuration which displays a similar behavior in field. The junction is in this case fairly open, with V_C accumulating electrons. $V_{LP,RP}$ are set to a voltage that pushes electrons away towards the superconductor.

The spectrum in Fig. 8.3(c) shows several ABS in the junction, a few of which show an oscillatory behavior in field. The magnetic field where they have their minimum corresponds roughly to half a magnetic flux quantum through the cross section of the NW.

The energies and phase dependence of ABS is directly linked to the qubit frequency. To understand the effect of ABS energies on the qubit frequency, we simulate the supercurrent using the Kwant package¹⁶⁹ and the analysis developed in Refs.^{160,170}. From the simulated critical current I_c , the qubit frequency $f_s = \sqrt{8E_J E_C}/h = \sqrt{2E_C I_c}/h\pi e$ is obtained, where $E_C = 2\mu\text{eV}$ is estimated from electrostatic simulations of the qubit island¹⁷¹ and $E_J = \hbar I_c/2e$.

In the simulated qubit frequency as a function of magnetic field [Fig. 8.3(d)], one can see a lobe-like structure where the qubit frequency oscillates as a function of magnetic field. The oscillation period of the ABS spectrum is lined up with the qubit frequency. Therefore, we conclude that the oscillatory behavior of the qubit frequency in field is linked to flux modulation of ABSs which form in the junction. Based on these simulations, we propose that the additional revival observed in the experiment is due to junction-based physics, in

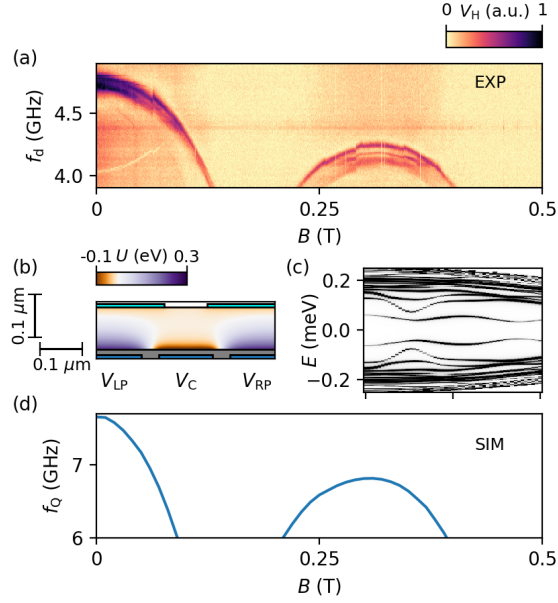


Figure 8.3: Two-tone spectroscopy as a function of drive frequency (f_d) and parallel magnetic field B , with $V_{\text{FET}} = +6.0$ V, $V_{\text{LP,RP}} = 0$ V, $V_C = -1.8$ V. At low field, f_Q decreases rapidly, disappearing from the measurement window at $B \sim 130$ mT. At higher field, f_Q recovers, re-entering the measurement window at $B \sim 220$ mT and then peaking at $B \sim 310$ mT before decreasing once more. At $B \sim 400$ mT, f_Q once again drops below the measured frequency range. (b) simulated electrostatic potential U near the junction on a vertical cut through the NW, for a revival in field configuration. The superconductor (Al) is indicated on the top (cyan), due to the positive band offset of 50 meV there is an accumulation layer towards it. The left plunger, the cutter and the right plunger gates are indicated on the bottom (dark blue). Both plungers are set to the same voltage $V_{\text{LP}} = V_{\text{RP}} = 0$ V. $V_C = 0.55$ V. (c) shows the simulated LDOS in the junction region for this gate configuration. A few low-energy ABSs showing flux-modulated oscillations can be found inside the junction. (d) shows the simulated qubit frequency for the same gate configuration. The flux-modulation of ABS results in an oscillation of the qubit frequency.

contrast to the low field f_Q decay which is dependent on the bulk wire gating.

Increasing the number of modes in the semiconductor as much as possible by setting gate voltages V_{PL} and V_{PR} to +8 V, ensuring that the junction is far into the disordered junction limit, the mesoscopic fluctuations of the dependence of f_Q on V_C were investigated. These fluctuations are closely related to previous work on mesoscopic fluctuations of critical current in Josephson junctions. In superconductor-normal-superconductor (SNS) Josephson junctions with a distance L between superconductors which is long compared to the mean free

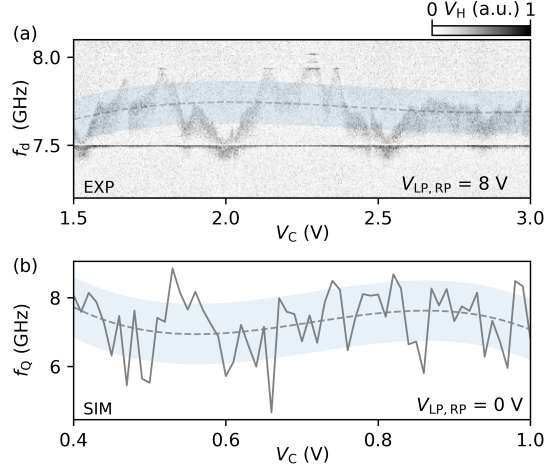


Figure 8.4: (a) Two-tone spectroscopy as a function of drive frequency (f_d) and gate voltage V_C . The qubit frequency exhibits mesoscopic fluctuations. The data is fitted with a smoothed spline (dashed line), and the light blue shading indicates the standard deviation, covering the area within $+/- \sigma$ of the fit. (b) A simulated trace of qubit frequency as a function of the gate voltage V_C , with the fluctuations analyzed in a similar manner to the experimental data.

path, l , in the N region and the superconducting coherence length, ξ , mesoscopic fluctuations of critical current I_c have a non-universal magnitude, $\sigma_{I_c} \sim ev_F l / L^2$, where v_F is the Fermi energy in the N region¹⁷². On the other hand, in short, disordered junctions $l \ll L < \xi$ fluctuations are universal, $\sigma_{I_c} \sim e\Delta_0/\hbar$ independent of junction parameters¹⁶². Our junction length is ~ 100 nm, which we can expect to be in the short junction limit, as confirmed by previous works on similar materials^{173,174}.

Experimentally, fluctuation statistics are extracted by sampling over V_C in Device 2. Figure 8.4(a) shows two-tone spectroscopy data as a function of junction gate V_C at $B = 0$. We perform these measurements at much more positive gate voltages than in the previous section, such that the number of modes in the junction is increased. The qubit frequency fluctuation is quantified by fitting a smoothed spline to the trace and extracting a standard deviation, yielding $\sigma_{f_0} \sim 130$ MHz. This corresponds to critical current fluctuation $\sigma_{I_c} \sim$

$(\pi e h f_Q / E_C) \sigma_{f_Q} \sim 1.0$ nA. This is much smaller than the theoretically predicted value¹⁶² for a short junction, which would give of order ~ 50 nA, but is in closer agreement with experiments measuring critical current oscillations^{163,175} which find fluctuations on the order of 1 nA.

Similar traces are simulated for a range of gate voltages, as shown in Fig. 8.4(b) for simulated $V_{LP,RP} = 0$. Changing the plunger gate voltages can be viewed as a variation in the simulated properties of the junction, which was not attempted in our experiment. The simulated fluctuation in f_Q are in the range 0.4–1 GHz, corresponding to critical current fluctuations in the range 3–9 nA. These values are higher than what was observed experimentally, but much lower than the universal value for a short junction.

In conclusion, we have investigated semiconductor based transmon qubits that allow both dc transport and cQED operation, controlled by a field effect transistor, and are magnetic field compatible. With the help of numerics, we observe that the rate of qubit frequency decay in field is controllable by gating of the bulk NW, while additional oscillatory behavior at higher fields may be attributed to flux modulation of ABSs in the junction. In the many-channel regime, mesoscopic fluctuations of the qubit frequency were observed. We find that the fluctuations are much smaller than expected for the universal theory, somewhat smaller than numerics, and comparable to previous corresponding results of fluctuations in critical current.

SUPPLEMENTARY MATERIAL

8.1 EXPERIMENTAL SETUP

The experimental setup used for the measurements presented in the paper is shown in Fig. 8.5. The frequency of the readout resonator was found by transmission measurements with a vector network analyzer (VNA). The qubit measurements were then carried out using two-tone spectroscopy using a heterodyne demodulation readout circuit. Using an rf switch matrix connected to both VNA and demodulation circuit, switching was possible between the two measurement configurations. The experiments were carried out in a dilution refrigerator with a base temperature of ~ 20 mK and a 6-1-1 T vector magnet.

Devices 1 and 2, for which data is shown in the main text, are illustrated in Figs. 8.6 and 8.7. An SEM image of Device 2 was not taken, to avoid detrimental effects.

8.2 SIMULATION PARAMETERS

For details of the numerical simulations see Ref. ¹⁶⁶⁻¹⁶⁸. At the InAs/Al boundary condition we use a band offset $U_0 = 50$ meV. On the bare InAs and InAs/oxide surfaces the density of interface traps is $n_{\text{dit}} = 1e^{12} \text{ eV}^{-1}\text{cm}^{-2}$ with a neutral level of $\varphi_{\text{nl}} = 0.1$ eV. The magnetic field dependence of the Al gap is given by $\Delta_0(B) = \max(0, \Delta_0(0)(1 - B^2/B_{\text{max}}^2))$ with $\Delta_0(0) = 0.25$ meV and the critical field $B_{\text{max}} = 1.4$ T. Inside the junction region, between the Al covered segments, a random uncorrelated potential disorder is placed corresponding to a mean free path of about 50 nm. The whole length of the simulated device is $2 \mu\text{m}$. The simulation does not include the spin degree of freedom, the magnetic field dependence is purely due to orbital effects.

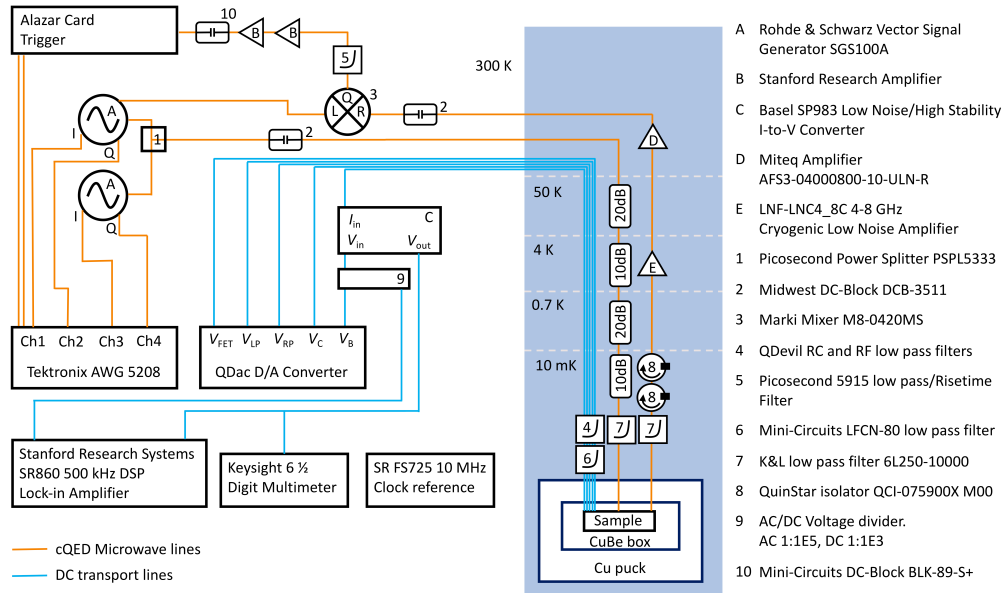


Figure 8.5: Diagram of the experimental setup used for the experiments described in the main text.

The other simulation parameters are the same literature values as used in Ref. ¹⁶⁶: $m_{\text{InAs}} = 0.026 m_0$, $m_{\text{Al}} = m_0$ and $E_{\text{F,Al}} = 11.7$ eV. Since the simulation parameters are not fine-tuned, the absolute value of qubit frequency might differ between the simulations and experiment due to differences in the electrostatic configuration, disorder or charging energy.

8.3 ADDITIONAL SIMULATIONS

In Fig. 8.8 we show the zero field simulated qubit frequency as a function of cutter and plunger voltages. The cutter is able to open and close the junction with relatively little cross-talk to the plungers. The behavior of the qubit frequency as a function of plunger is non-

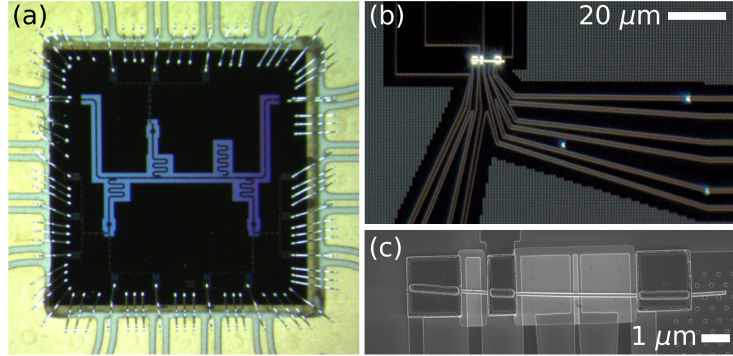


Figure 8.6: Device 1. (a) An optical micrograph of the bonded sample, containing three qubit devices. Each device is connected to a qubit island, which is capacitively coupled to a readout resonator. Device 1, from which measurements are presented in the main text, is in the bottom right corner. (b) A magnified dark field micrograph of Device 1. The qubit island, to which the nanowire is contacted, is visible at the top of the image. (c) Scanning electron micrograph of Device 1, as seen in the main text.

monotonic. For plungers below $V_p < 0.4 \text{ V}$ making the plungers more positive adds more channels and the qubit frequency increases. It reaches a maximum at around $V_p \sim 0.4 \text{ V}$. For more positive plungers the number of channels still increases, however, the induced gap collapses since the electrons are pulled away from the interface with Al. Since the added channels are only weakly proximitized, the simulated qubit frequency decreases for $V_p > 0.4 \text{ V}$.

In Fig. 8.9 we show the simulated qubit frequency as a function of magnetic field for different combinations of cutter and symmetric plunger voltages. If the junction is only barely open (i.e. $V_C = 0.2 \text{ V}$) the qubit frequency decays monotonically with magnetic field. If the junction is more open (i.e. $V_C \geq 0.3 \text{ V}$) an oscillatory behavior is generally observed. Since the wire is in a multi-mode regime and different modes have different wavefunction cross-sections, the oscillations are not in every case completely regular. Furthermore, the qubit frequency never seems to crash completely before the revival but only reduces in magnitude (possibly below the limited window for which the qubit frequency is experimentally observ-

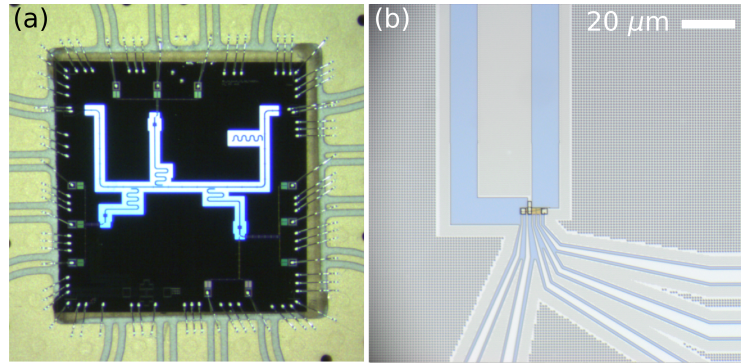


Figure 8.7: Device 2. (a) An optical micrograph of the bonded sample, containing three qubit devices. Each device is connected to a qubit island, which is capacitively coupled to a readout resonator. Device 2, from which measurements are presented in the main text, is in the bottom right corner. (b) A magnified micrograph of Device 2. The qubit island, to which the nanowire is contacted, is visible at the top of the image, and the gate lines can be seen at the bottom.

able).

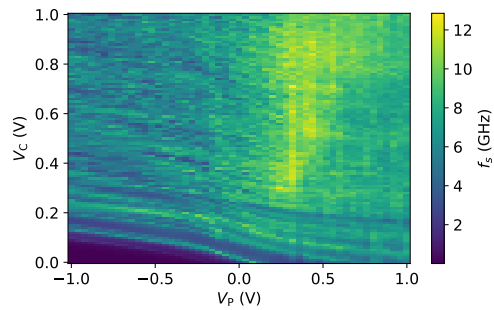


Figure 8.8: Map of the zero field simulated qubit frequency as a function of cutter and symmetric plunger voltages ($V_p = V_{LP} = V_{RP}$).

8.4 ADDITIONAL DATA

In Fig. 8.10, we show two-tone spectroscopy measurements as a function of parallel magnetic field B at a range of $V_{LP,RP}$ voltages. An average was subtracted from each column in the measured V_H signal to improve the qubit frequency visibility, the Q and I components of

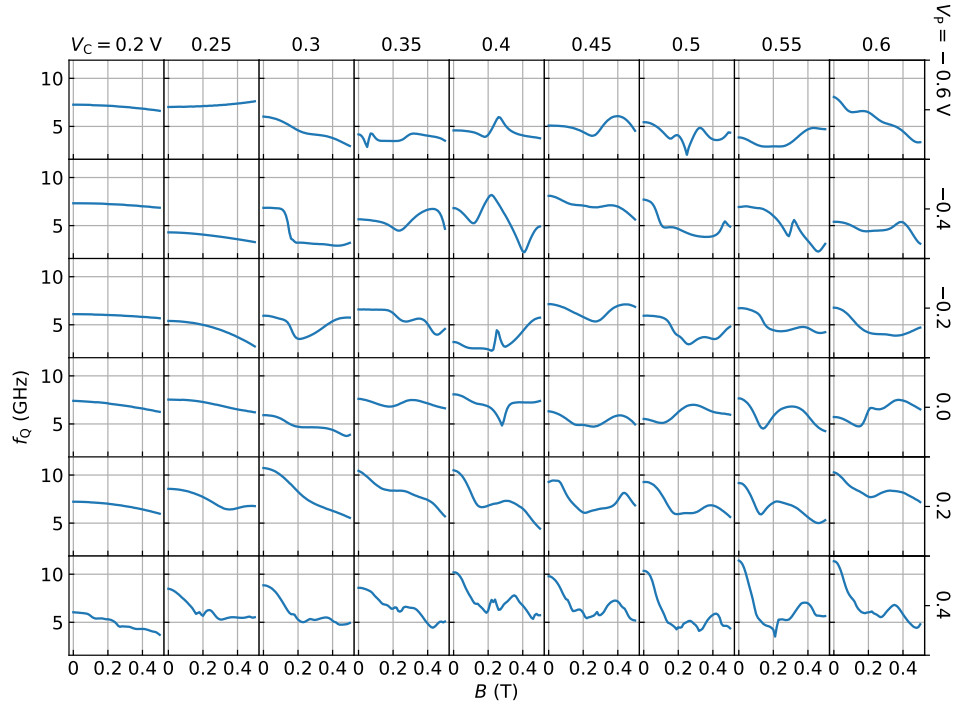


Figure 8.9: Simulated qubit frequency as a function of magnetic field for a variety of cutter and symmetric plunger voltages ($V_P = V_{LP} = V_{RP}$).

V_H were added in quadrature, and finally the data was normalized. From these data, the values of f_Q shown in Fig. 2 of the main text were extracted via peak-finding. As mentioned in the main text, the voltage V_C applied to the junction gate was adjusted to keep the zero field frequency close to constant as the NW gate voltages $V_{LP,RP}$ were varied. For completeness, we show the corresponding V_C values in Fig. 8.11.

To extract the magnitude of the qubit frequency fluctuations in the many-modes section of the experiment, a two-tone spectroscopy map is taken as a function of drive frequency (f_d) and gate voltage V_C . The I and Q components of the signal are measured. The mean is subtracted from each line of measurement, and the components are then added in quadra-

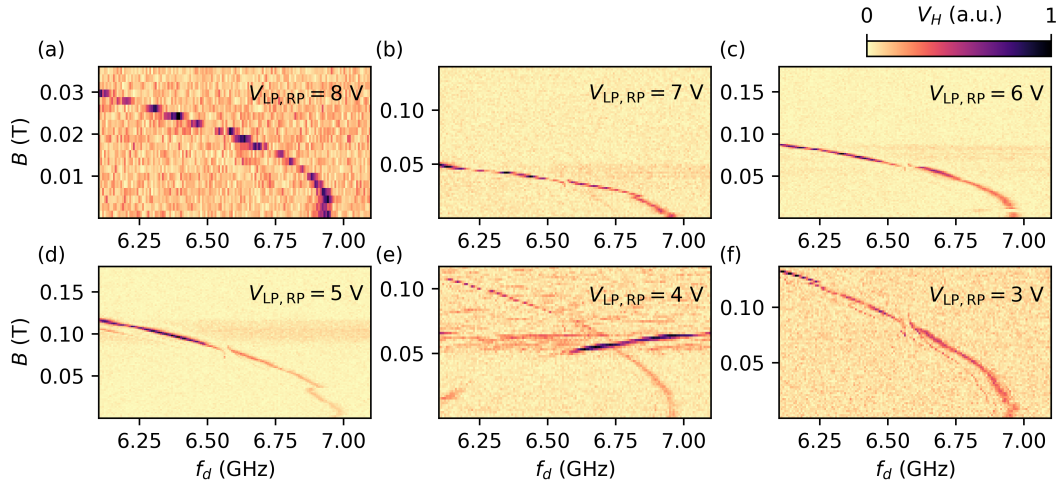


Figure 8.10: (a) Two-tone spectroscopy of the qubit as a function of parallel magnetic field B at a range of plunger gate voltages. This data was used to extract the qubit frequencies discussed in Fig. 2 of the main text. The cutter gate was compensated slightly to keep the zero field frequency constant for all gate configurations.

ture. There is an accidental resonance at around 7.5 GHz, visible in Fig. 8.12 and also in the main text. The values of the three lines which contain the resonance are temporarily set to 0 during the peak extraction procedure, as otherwise the resonance would interfere with peak extraction. After this, the most prominent peak for every gate voltage is extracted. The extracted peak positions are shown as yellow and dark blue crosses in Fig. 8.12. We exclude from the analysis the section of the measurement where the qubit frequency starts to leave the measurement window. The peaks used for the analysis are shown as dark blue crosses. From this point, the analysis is identical for the experimental data shown in Fig. 8.12 and the simulated data sets presented in the main text.

The data points in the area of interest are fitted using a smoothed spline curve, with a smoothing factor 100. This number is arbitrarily selected, and does not influence the result significantly. The average frequency for the trace is then calculated by finding the mean of the data

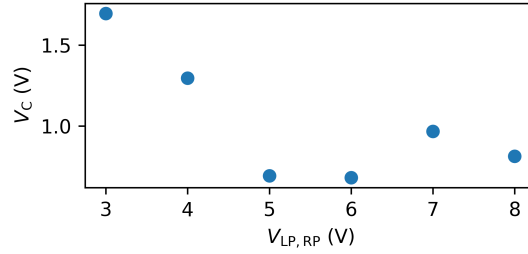


Figure 8.11: Values of V_C which were adjusted to compensate the zero-field frequency for the measurements of qubit frequency in parallel field, plotted as a function of the corresponding values of $V_{LP,RP}$

points along the smoothed interpolated trace. The fluctuation σ_f is quantified by taking a standard deviation of the measured (or simulated) data points from the interpolated curve,

$$\sigma_{f_Q} = \sqrt{\frac{\sum (f_{\text{interp}} - f_{\text{measured}})^2}{N}} \quad (8.1)$$

where f_{interp} are the interpolated frequency values taken from the spline fit, f_{measured} are the frequency values extracted from the peak finding procedure, and N is the total number of frequency data points.

Figure 8.12 (b) shows the results of the completed fitting and extraction procedure for the experimental data. The extracted peaks from the region of interest are shown as dark blue crosses. The light blue line indicates the smoothed interpolated spline fit. The standard deviation of the data from the smoothed fit is shown as blue shading either side of the line fit.

In Fig. 8.13 we show a similar measurement to the ones described in Fig. 3. (a) in the main text. This data is taken on a device identical in materials and fabrication to Devices 1 and 2, and shows a non-monotonic behavior of the qubit frequency in parallel magnetic field. Unfortunately, this device was less stable than the one presented in the main text, so we observe a sudden loss of signal just below 0.4 T. It is still clear to see however that in this configuration,

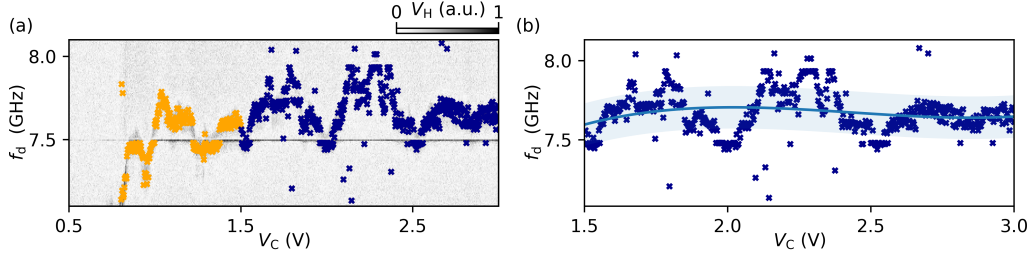


Figure 8.12: Illustration of peak finding and fitting procedure for extraction of the mesoscopic fluctuations of the qubit frequency. (a) Shows two-tone spectroscopy as a function of drive frequency (f_d) and gate voltage V_C , the same data as shown in Fig. 4. (a) in the main text. Peaks extracted and used for the fitting procedure (dark blue crosses) and those extracted but unused (yellow crosses) are shown. (b) Shows the peaks used for the fluctuation extraction. These are fitted with a smoothed spline (solid blue line), and the standard deviation is indicated (light blue shading), covering the area within $\pm \sigma$ of the fit.

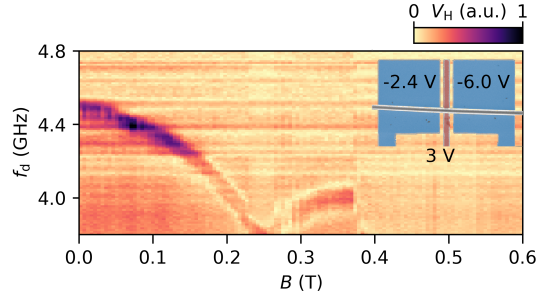


Figure 8.13: (a) Two-tone spectroscopy as a function of drive frequency (f_d) and parallel magnetic field B , with $V_{\text{FET}} = 6$ V and the other gate voltages displayed in the inset. The qubit frequency decreases monotonically at first, then at ~ 0.25 T a revival in the frequency is observed. There appears to be a charge switch just below 0.4 T.

with a very positive junction gate, a similar modulation of the qubit frequency takes place in field. We attribute this to the same physical mechanism as described in the main text: a flux modulation in field of a few Andreev bound states in the qubit junction.

9

Conclusion and outlook

THROUGHOUT THIS THESIS, several device configurations and measurement techniques were discussed, all with the aim of reducing the ambiguity which is faced by experimentalists when studying quantum states in superconductor-semiconductor hybrid structures.

We started by discussing local tunnelling spectroscopy measurements, which give a de-

tailed insight into the local density of states of a hybrid nanowire, and tried to convey why this information is not enough if one wishes to make claims about a nonlocal or extended phase or quantum state. However, by adding more local probes, we are able to extract more information. In the case of our experiments, the system remained topologically trivial, but we were able to explore the extension of Andreev bound states by probing the same extended object from both sides. Still using local spectroscopy at two ends of a proximitized segment, we introduced some checks that can be performed to confirm whether one is really looking at an extended quantum state, or just at two objects which are totally separate but appear similar.

Next, we considered more sophisticated methods of probing the bound states forming in our devices, including nonlocal conductance, which allows not only for the measurement of a state from both sides as before, but also for the extraction of information about the level of disorder in the system, and the calculation of the BCS charge of the extended states. We also introduced the use of quantum dots, formed accidentally in the tunnel barriers of our devices, as probes of the nonlocality of the bound states, via their hybridization.

Finally, we introduced a device configuration in which lateral quantum dots are deliberately formed at multiple probe locations along a nanowire. This deliberate dot formation allows for more control over properties like the coupling between the dot and the superconductor, which are explored for various device designs. Finally, we discussed the use of a weakly coupled quantum dot level as a spin and charge resolved spectrometer, allowing for spin resolved spectroscopy of both the splitting of the superconducting gap in magnetic field, and the evolution of bound states in both magnetic field and gate voltage.

These methods, developed here to study the states in hybrid materials with as little am-

biguity as possible, can be utilized in future work on superconductor-semiconductor hybrid materials. This could possibly include confirmation of the observation of a topological phase, as cleaner materials become available. The spin-resolved spectroscopy technique may also be used in a wider context, and possibly carried over to other platforms.

To me, these experiments performed over the last few years highlight that we still have a distance to go in understanding the layers of physics which come together to give the effects which we observe, but by devising creative experimental techniques and critically evaluating our expectations, we can stride forwards.



Fabrication protocols

A.1 SIDE-PROBE DEVICES WITH SUPERCONDUCTING LEADS

Cleaving

- Begin with wafer coated with post-baked A₄ PMMA resist
- Using manual scribe, scribe and cleave into chips ~ 3 by 5 mm

Alignment marks

- **Clean** the chip: 5 minutes in dioxolane, acetone squirt, IPA squirt, blowdry.
- **Spin coat** resist: A4 @ 4000 RPM, 45 sec. Bake at 185 °C for 2 min. *Optionally, skip the cleaning and re-spin coating and use the resist which is already on the chip when it is cleaved. This avoids beating at the edges.*
- **Expose** alignment marks and numbers: 500 pA, 300 μm field, 60000 dots, dose of 0.34 $\mu\text{s}/\text{dot}$, area dose: 640 $\mu\text{C}/\text{cm}^2$ with proximity effect correction for InAs substrate, 200 nm PMMA, 100 kV, optimal contrast.
- **Expose** outer pads: 20 nA, 600 μm field, 20000 dots, dose of 0.306 $\mu\text{s}/\text{dot}$, area dose: 640 $\mu\text{C}/\text{cm}^2$ with proximity effect correction for InAs substrate, 200 nm PMMA, 100 kV, optimal contrast.
- **Develop** 45 s in MIBK:IPA, then 5s IPA, blowdry. Ash 45 s.
- **Metal deposition** with AJA, use rotation at 50 rpm, no tilt angle. Evaporate 10 nm of Ti, 40 nm of Au.
- **Liftoff** in 1,3 dioxolane, with sonication for 5 min @ 80 kHz, 70% pwr. Hard acetone squirt 10 s, IPA squirt 10 s, blow dry.

Mesa etch

- **Spin coat** resist: A4 @ 4000 RPM, 45 sec. Bake at 185 °C for 2 min.

- **Expose** inner mesa 500 pA, 150 μm field, 60000 dots, dose of 0.085 $\mu\text{s}/\text{dot}$, area dose: 680 $\mu\text{C}/\text{cm}^2$ with proximity effect correction for InAs substrate, 200 nm PMMA, 100 kV, optimal contrast.
- **Expose** outer mesa 20 nA, 600 μm field, 20000 dots, dose of 0.34 $\mu\text{s}/\text{dot}$, area dose: 640 $\mu\text{C}/\text{cm}^2$ with proximity effect correction for InAs substrate, 200 nm PMMA, 100 kV, optimal contrast.
- **Develop** 60 s MIBK:IPA, then 5 s IPA, blowdry.
- **Ash** 1 min.
- **Post bake** 2 min at 120 $^{\circ}\text{C}$.
- **Etch the Al**; prepare 3 cups: one medium with transene Al etch D in a hot bath, aiming for 50 $^{\circ}\text{C}$. The level of the liquids inside and outside the beakers must match. Another medium with MQ water in the hot bath, and a big one with MQ outside the hot bath.

Etching procedure: 5 s dip in hot Al Etchant D, 20 s in hot MQ, 40s in room temperature MQ. In all steps swirl rigorously, then blow dry.

- **Etch the mesa**; our standard etch mixture is $\text{H}_2\text{O} : \text{citric acid} : \text{H}_3\text{PO}_4 : \text{H}_2\text{O}_2$ in the ratios 220 : 55 : 3 : 3.

First water, add citric acid, start stirring, add H_3PO_4 . H_2O_2 is added just before starting the Al etching step.

Etch for 9 mins. Every 30 s, rotate the chip by $\pi/2$ inside the beaker. Immediately after etching dip in MQ water for ~ 60 s with rigorous swirling. Blow dry.

- **Strip** for 15 min in dioxolane, acetone dip 10 s, IPA dip 10 s, blow dry. Measure the mesa height with profilometer.

Aluminum etch

- **Spin coat resist:** A4 @ 4000 RPM, 45 sec. Bake at 185 °C for 2 min.
- **Expose** 100 pA, 150 μm field, 60000 dots, dose of 0.42 μs/dot, area dose: 672 μC/cm² with proximity effect correction for InAs substrate, 200 nm PMMA, 100 kV, optimal contrast.
- **Develop** 45 s MIBK:IPA, then 5 s IPA, blowdry.
- **Ash** 45 s.
- **Post bake** 2 min at 120 °C.
- **Etch the Al;** prepare 3 cups: one medium with transene Al etch D in a hot bath, aiming for 50 °C. The level of the liquids inside and outside the beakers must match. Another medium with MQ water in the hot bath, and a big one with MQ outside the hot bath.

Etching procedure: 5 s dip in hot Al Etchant D, 20 s in hot MQ, 40s in room temperature MQ. In all steps swirl rigorously, then blow dry. Optical inspection to check for etch run.

- **Strip** for 30 min in dioxolane, acetone dip 10 s, IPA dip 10 s, blow dry.

Dielectric deposition

- ALD - 150 cycles for 15 nm HfO₂. 10 hours of pumping with hot stages at 95 °C. Set stage temperatures to 90 °C.

150 times: Hf pulse, 0.5 s, wait 180 sec, H₂O pulse, 0.02 s, wait 180 sec

Inner gates, first round

- Spin coat resist: A4 @ 4000 RPM, 45 sec. Bake at 185 °C for 2 min.
- **Expose** 100 pA, 150 μm field, 60000 dots, dose of 0.38 μs/dot, area dose: 608 μC/cm² with proximity effect correction for InAs substrate, 200 nm PMMA, 100 kV, optimal contrast.
- **Develop** 45 s MIBK:IPA, then 5 s IPA, blowdry.
- **Ash** 60 s.
- **Metal deposition** with AJA, no rotation, no tilt angle. Evaporate 5 nm of Ti, 20 nm of Au.
- **Liftoff** overnight in dioxolane, acetone dip 10 s, IPA dip 10 s, blow dry.

Outer gates, first round

- Spin coat resist: EL9 @ 4000 RPM, 45 sec. Bake at 185 °C for 2 min. EL9 @ 4000 RPM, 45 sec. Bake at 185 °C for 2 min. A4 @ 4000 RPM, 45 sec. Bake at 185 °C for 2 min.
- **Expose** inner part; 500 pA, 300 μm field, 60000 dots, dose of 0.32 μs/dot, area dose: 640 μC/cm² with proximity effect correction for InAs substrate, 200 nm PMMA, 100 kV, optimal contrast.

- **Expose** outer part; 20 nA, 600 μm field, 20000 dots, dose of 0.3 $\mu\text{s}/\text{dot}$, area dose: 640 $\mu\text{C}/\text{cm}^2$ with proximity effect correction for InAs substrate, 200 nm PMMA, 100 kV, optimal contrast.
- **Develop** 45 s MIBK:IPA, then 5 s IPA, blowdry.
- **Ash** 60 s.
- **Metal deposition** with AJA, rotation at 50 rpm. Tilt 5 deg, evaporate 10 nm of Ti, 30 nm of Au. Tilt 0 deg, evaporate 300 nm of Au. Tilt 10 deg, evaporate 50 nm of Au. *Adjust height according to mesa profilometer reading.*
- **Liftoff** overnight in dioxolane, acetone dip 10 s, IPA dip 10 s, blow dry.

Second dielectric deposition

- ALD - 120 cycles for 12 nm HfO_2 . 10 hours of pumping with hot stages at 95 $^\circ\text{C}$. Set stage temperatures to 90 $^\circ\text{C}$.
120 times: Hf pulse, 0.5 s, wait 180 sec, H_2O pulse, 0.02 s, wait 180 sec

Inner gates, second round

- Spin coat resist: A4 @ 4000 RPM, 45 sec. Bake at 185 $^\circ\text{C}$ for 2 min.
- **Expose** 100 pA, 150 μm field, 60000 dots, dose of 0.38 $\mu\text{s}/\text{dot}$, area dose: 608 $\mu\text{C}/\text{cm}^2$ with proximity effect correction for InAs substrate, 200 nm PMMA, 100 kV, optimal contrast.
- **Develop** 45 s MIBK:IPA, then 5 s IPA, blowdry.

- **Ash** 60 s.
- **Metal deposition** with AJA, no rotation, no tilt angle. Evaporate 5 nm of Ti, 20 nm of Au.
- **Liftoff** overnight in dioxolane, acetone dip 10 s, IPA dip 10 s, blow dry.

Outer gates, second round

- Spin coat resist: EL9 @ 4000 RPM, 45 sec. Bake at 185 °C for 2 min. EL9 @ 4000 RPM, 45 sec. Bake at 185 °C for 2 min. A4 @ 4000 RPM, 45 sec. Bake at 185 °C for 2 min.
- **Expose** inner part; 500 pA, 300 μm field, 60000 dots, dose of 0.32 $\mu\text{s}/\text{dot}$, area dose: 640 $\mu\text{C}/\text{cm}^2$ with proximity effect correction for InAs substrate, 200 nm PMMA, 100 kV, optimal contrast.
- **Expose** outer part; 20 nA, 600 μm field, 20000 dots, dose of 0.3 $\mu\text{s}/\text{dot}$, area dose: 640 $\mu\text{C}/\text{cm}^2$ with proximity effect correction for InAs substrate, 200 nm PMMA, 100 kV, optimal contrast.
- **Develop** 45 s MIBK:IPA, then 5 s IPA, blowdry.
- **Ash** 60 s.
- **Metal deposition** with AJA, rotation at 50 rpm. Tilt 5 deg, evaporate 10 nm of Ti, 30 nm of Au. Tilt 0 deg, evaporate 300 nm of Au. Tilt 10 deg, evaporate 50 nm of Au. *Adjust height according to mesa profilometer reading.*
- **Liftoff** overnight in dioxolane, acetone dip 10 s, IPA dip 10 s, blow dry.

- **Ash** 120 s.

A.2 SIDE-PROBE DEVICES WITH SEMICONDUCTING LEADS

Cleaving

- Begin with wafer coated with post-baked A4 PMMA resist
- Using manual scribe, scribe and cleave into chips \sim 3 by 5 mm

Alignment marks

- **Clean** the chip: 5 minutes in dioxolane, acetone squirt, IPA squirt, blowdry.
- **Spin coat** resist: A4 @ 4000 RPM, 45 sec. Bake at 185 °C for 2 min. *Optionally, skip the cleaning and re-spin coating and use the resist which is already on the chip when it is cleaved. This avoids beating at the edges.*
- **Expose** alignment marks and numbers: 500 pA, 300 μ m field, 60000 dots, dose of 0.34 μ s/dot, area dose: 640 μ C/cm² with proximity effect correction for InAs substrate, 200 nm PMMA, 100 kV, optimal contrast.
- **Expose** outer pads: 20 nA, 600 μ m field, 20000 dots, dose of 0.306 μ s/dot, area dose: 640 μ C/cm² with proximity effect correction for InAs substrate, 200 nm PMMA, 100 kV, optimal contrast.
- **Develop** 45 s in MIBK:IPA, then 5s IPA, blowdry. Ash 45 s.
- **Metal deposition** with AJA, use rotation at 50 rpm, no tilt angle. Evaporate 10 nm of Ti, 40 nm of Au.

- **Liftoff** in 1,3 dioxolane, with sonication for 5 min @ 80 kHz, 70% pwr. Hard acetone squirt 10 s, IPA squirt 10 s, blow dry.

Mesa etch

- **Spin coat** resist: A4 @ 4000 RPM, 45 sec. Bake at 185 °C for 2 min.
- **Expose** inner mesa 500 pA, 150 μm field, 60000 dots, dose of 0.085 μs/dot, area dose: 680 μC/cm² with proximity effect correction for InAs substrate, 200 nm PMMA, 100 kV, optimal contrast.
- **Expose** outer mesa 20 nA, 600 μm field, 20000 dots, dose of 0.34 μs/dot, area dose: 640 μC/cm² with proximity effect correction for InAs substrate, 200 nm PMMA, 100 kV, optimal contrast.
- **Develop** 60 s MIBK:IPA, then 5 s IPA, blowdry.
- **Ash** 1 min.
- **Post bake** 2 min at 120 °C.
- **Etch the Al**; prepare 3 cups: one medium with transene Al etch D in a hot bath, aiming for 50 °C. The level of the liquids inside and outside the beakers must match. Another medium with MQ water in the hot bath, and a big one with MQ outside the hot bath.

Etching procedure: 5 s dip in hot Al Etchant D, 20 s in hot MQ, 40s in room temperature MQ. In all steps swirl rigorously, then blow dry.

- **Etch the mesa;** our standard etch mixture is $\text{H}_2\text{O} : \text{citric acid} : \text{H}_3\text{PO}_4 : \text{H}_2\text{O}_2$ in the ratios 220 : 55 : 3 : 3.

First water, add citric acid, start stirring, add H_3PO_4 . H_2O_2 is added just before starting the Al etching step.

Etch for 9 mins. Every 30 s, rotate the chip by $\pi/2$ inside the beaker. Immediately after etching dip in MQ water for ~ 60 s with rigorous swirling. Blow dry.

- **Strip** for 15 min in dioxolane, acetone dip 10 s, IPA dip 10 s, blow dry. Measure the mesa height with profilometer.

Aluminum etch

- Spin coat resist: A4 @ 4000 RPM, 45 sec. Bake at 185 °C for 2 min.
- **Expose** 100 pA, 150 μm field, 60000 dots, dose of 0.42 $\mu\text{s}/\text{dot}$, area dose: 672 $\mu\text{C}/\text{cm}^2$ with proximity effect correction for InAs substrate, 200 nm PMMA, 100 kV, optimal contrast.
- **Develop** 45 s MIBK:IPA, then 5 s IPA, blowdry.
- **Ash** 45 s.
- **Post bake** 2 min at 120 °C.
- **Etch the Al;** prepare 3 cups: one medium with transene Al etch D in a hot bath, aiming for 50 °C. The level of the liquids inside and outside the beakers must match. Another medium with MQ water in the hot bath, and a big one with MQ outside the hot bath.

Etching procedure: 5 s dip in hot Al Etchant D, 20 s in hot MQ, 40s in room temperature MQ. In all steps swirl rigorously, then blow dry. Optical inspection to check for etch run.

- **Strip** for 30 min in dioxolane, acetone dip 10 s, IPA dip 10 s, blow dry.

Dielectric deposition

- ALD - 150 cycles for 15 nm HfO₂. 10 hours of pumping with hot stages at 95 °C. Set stage temperatures to 90 °C.

150 times: Hf pulse, 0.5 s, wait 180 sec, H₂O pulse, 0.02 s, wait 180 sec

Inner gates

- Spin coat resist: A4 @ 4000 RPM, 45 sec. Bake at 185 °C for 2 min.
- **Expose** 100 pA, 150 μm field, 60000 dots, dose of 0.38 μs/dot, area dose: 608 μC/cm² with proximity effect correction for InAs substrate, 200 nm PMMA, 100 kV, optimal contrast.
- **Develop** 45 s MIBK:IPA, then 5 s IPA, blowdry.
- **Ash** 60 s.
- **Metal deposition** with AJA, no rotation, no tilt angle. Evaporate 5 nm of Ti, 20 nm of Au.
- **Liftoff** overnight in dioxolane, acetone dip 10 s, IPA dip 10 s, blow dry.

Outer gates

- Spin coat resist: EL9 @ 4000 RPM, 45 sec. Bake at 185 °C for 2 min. EL9 @ 4000 RPM, 45 sec. Bake at 185 °C for 2 min. A4 @ 4000 RPM, 45 sec. Bake at 185 °C for 2 min.
- **Expose** inner part; 500 pA, 300 μm field, 60000 dots, dose of 0.32 $\mu\text{s}/\text{dot}$, area dose: 640 $\mu\text{C}/\text{cm}^2$ with proximity effect correction for InAs substrate, 200 nm PMMA, 100 kV, optimal contrast.
- **Expose** outer part; 20 nA, 600 μm field, 20000 dots, dose of 0.3 $\mu\text{s}/\text{dot}$, area dose: 640 $\mu\text{C}/\text{cm}^2$ with proximity effect correction for InAs substrate, 200 nm PMMA, 100 kV, optimal contrast.
- **Develop** 45 s MIBK:IPA, then 5 s IPA, blowdry.
- **Ash** 60 s.
- **Metal deposition** with AJA, rotation at 50 rpm. Tilt 5 deg, evaporate 10 nm of Ti, 30 nm of Au. Tilt 0 deg, evaporate 300 nm of Au. Tilt 10 deg, evaporate 50 nm of Au. *Adjust height according to mesa profilometer reading.*
- **Liftoff** overnight in dioxolane, acetone dip 10 s, IPA dip 10 s, blow dry.
- **Ash** 120 s.

References

- [1] A. Yu Kitaev. Unpaired Majorana fermions in quantum wires. *Physics-Uspekhi*, 44(10S), 2001.
- [2] R. M. Lutchyn, J. D. Sau, and S. Das Sarma. Majorana Fermions and a Topological Phase Transition in Semiconductor-Superconductor Heterostructures. *Phys. Rev. Lett.*, 105(7):077001, 2010.
- [3] Y. Oreg, G. Refael, and F. von Oppen. Helical Liquids and Majorana Bound States in Quantum Wires. *Phys. Rev. Lett.*, 105(17):177002, 2010.
- [4] P. Krogstrup, N. L. B. Ziino, W. Chang, S. M. Albrecht, M. H. Madsen, E. Johnson, J. Nygård, C. M. Marcus, and T. S. Jespersen. Epitaxy of semiconductor-superconductor nanowires. *Nature Materials*, 14(4):400–406, 2015.
- [5] J. Shabani, M. Kjaergaard, H. J. Suominen, Younghyun Kim, F. Nichele, K. Pakrouski, T. Stankevic, R. M. Lutchyn, P. Krogstrup, R. Feidenhans'l, S. Kraemer, C. Nayak, M. Troyer, C. M. Marcus, and C. J. Palmstrøm. Two-dimensional epitaxial superconductor-semiconductor heterostructures: A platform for topological superconducting networks. *Phys. Rev. B*, 93(15):155402, 2016.
- [6] A. M. Whiticar. *Flux dependence of topological superconductivity in two-dimensional heterostructures*. Phd thesis, University of Copenhagen, 2020.
- [7] M. Chapman and C. S. de Melo. Atoms playing dress-up. *Nature*, 471(7336):41–42, 2011.
- [8] C. Harmans. *Mesoscopic Physics: An Introduction: TN385*. 1997. TU Delft.
- [9] R. Winkler. *Spin—Orbit Coupling Effects in Two-Dimensional Electron and Hole Systems*, volume 191 of *Springer Tracts in Modern Physics*. Springer, Berlin, Heidelberg, 2003.

- [10] M. Tinkham. *Introduction to Superconductivity: Second Edition*. Dover Publications, Mineola, NY, 2004.
- [11] N. B. Kopnin. Introduction to The Theory of Superconductivity Cryocourse 2009 Helsinki, Finland, 2009.
- [12] J. F. Cochran and D. E. Mapother. Superconducting Transition in Aluminum. *Physical Review*, 111:132–142, 1958.
- [13] J. Bardeen, L. N. Cooper, and J. R. Schrieffer. Theory of Superconductivity. *Phys. Rev.*, 108(5):1175–1204, 1957.
- [14] D. J. Thouless. Strong-Coupling Limit in the Theory of Superconductivity. *Phys. Rev.*, 117(5):1256–1260, 1960.
- [15] R. J. Donnelly. *Cryogenics*. 1981.
- [16] C. W. J. Beenakker. Why Does a Metal—Superconductor Junction Have a Resistance? In *Quantum Mesoscopic Phenomena and Mesoscopic Devices in Microelectronics*, NATO Science Series, pages 51–60. Springer Netherlands, Dordrecht, 2000.
- [17] A. F. Andreev. THERMAL CONDUCTIVITY OF THE INTERMEDIATE STATE OF SUPERCONDUCTORS. *Zh. Eksperim. i Teor. Fiz.*, Vol: 46, 1964.
- [18] G. E. Blonder, M. Tinkham, and T. M. Klapwijk. Transition from metallic to tunneling regimes in superconducting microconstrictions: Excess current, charge imbalance, and supercurrent conversion. *Phys. Rev. B*, 25(7):4515–4532, 1982.
- [19] B. Pannetier and H. Courtois. Andreev Reflection and Proximity effect. *Journal of Low Temperature Physics*, 118(5):599–615, 2000.
- [20] T. M. Klapwijk. Proximity Effect From an Andreev Perspective. *Journal of Superconductivity*, 17(5):593–611, 2004.
- [21] A. E. Antipov, A. Bargerbos, G. W. Winkler, B. Bauer, E. Rossi, and R. M. Lutchyn. Effects of Gate-Induced Electric Fields on Semiconductor Majorana Nanowires. *Phys. Rev. X*, 8(3):031041, 2018.
- [22] G. O. Steffensen, J. C. Estrada Saldaña, A. Vekris, P. Krogstrup, K. Grove-Rasmussen, J. Nygård, A. L. Yeyati, and J. Paaske. Direct transport between superconducting subgap states in a double quantum dot. *Phys. Rev. B*, 105(16):L161302, 2022.

- [23] Y. Luh. BOUND STATE IN SUPERCONDUCTORS WITH PARAMAGNETIC IMPURITIES. *Acta Physica Sinica*, 21(1):75–91, 2005.
- [24] H. Shiba. Classical Spins in Superconductors. *Progress of Theoretical Physics*, 40(3):435–451, 1968.
- [25] A. I. Rusinov. SUPERCONDUCTIVITY NEAR A PARAMAGNETIC IMPURITY. *JETP Lett. (USSR) (Engl. Transl.)*, 9: 85-7, 1969.
- [26] C. Jünger, R. Delagrangé, D. Chevallier, S. Lehmann, K. A. Dick, C. Thelander, J. Klinovaja, D. Loss, A. Baumgartner, and C. Schönenberger. Magnetic-Field-Independent Subgap States in Hybrid Rashba Nanowires. *Phys. Rev. Lett.*, 125(1):017701, 2020.
- [27] E. Majorana. Teoria simmetrica dell’elettrone e del positrone. *Il Nuovo Cimento (1924-1942)*, 14(4):171, 1937.
- [28] C. Beenakker and L. Kouwenhoven. A road to reality with topological superconductors. *Nature Physics*, 12(7):618–621, 2016.
- [29] L. Fu and C. L. Kane. Superconducting Proximity Effect and Majorana Fermions at the Surface of a Topological Insulator. *Phys. Rev. Lett.*, 100(9):096407, 2008.
- [30] H. Bruus and K. Flensberg. *Many-Body Quantum Theory in Condensed Matter Physics: An Introduction*. Oxford Graduate Texts. Oxford University Press, Oxford, New York, 2004.
- [31] M. Leijnse and K. Flensberg. Introduction to topological superconductivity and Majorana fermions. *Semiconductor Science and Technology*, 27(12):124003, 2012.
- [32] F. Wilczek. Quantum Mechanics of Fractional-Spin Particles. *Phys. Rev. Lett.*, 49(14):957–959, 1982.
- [33] S. Das Sarma, M. Freedman, and C. Nayak. Majorana zero modes and topological quantum computation. *npj Quantum Information*, 1(1):1–13, October 2015.
- [34] D. Aasen, M. Hell, R. V. Mishmash, A. Higginbotham, J. Danon, M. Leijnse, Thomas S. Jespersen, J. A. Folk, C. M. Marcus, K. Flensberg, and J. Alicea. Milestones Toward Majorana-Based Quantum Computing. *Phys. Rev. X*, 6(3):031016, 2016.

- [35] E. Prada, P. San-Jose, M. W. A. de Moor, A. Geresdi, E. J. H. Lee, J. Klinovaja, D. Loss, J. Nygård, R. Aguado, and L. P. Kouwenhoven. From Andreev to Majorana bound states in hybrid superconductor–semiconductor nanowires. *Nature Reviews Physics*, 2(10):575–594, 2020.
- [36] R. C. Ashoori. Electrons in artificial atoms. *Nature*, 379:413–419, 1996.
- [37] L. P. Kouwenhoven, C. M. Marcus, P. L. Mceuen, S. Tarucha, and N. S. Wingreen. ELECTRON TRANSPORT IN QUANTUM DOTS. *QUANTUM DOTS*, page 110, 1997.
- [38] T. Ihn. *Semiconductor Nanostructures: Quantum States and Electronic Transport*. Oxford University Press, 2010.
- [39] S. De Franceschi, L. Kouwenhoven, C. Schönenberger, and W. Wernsdorfer. Hybrid superconductor–quantum dot devices. *Nature Nanotechnology*, 5(10):703–711, 2010.
- [40] A. Eichler, M. Weiss, S. Oberholzer, C. Schönenberger, A. Levy Yeyati, J. C. Cuevas, and A. Martín-Rodero. Even-Odd Effect in Andreev Transport through a Carbon Nanotube Quantum Dot. *Phys. Rev. Lett.*, 99(12):126602, 2007.
- [41] T. Sand-Jespersen, J. Paaske, B. M. Andersen, K. Grove-Rasmussen, H. I. Jørgensen, M. Aagesen, C. B. Sørensen, P. E. Lindelof, K. Flensberg, and J. Nygård. Kondo-Enhanced Andreev Tunneling in InAs Nanowire Quantum Dots. *Phys. Rev. Lett.*, 99(12):126603, 2007.
- [42] G. Kiršanskas, M. Goldstein, K. Flensberg, L. I. Glazman, and J. Paaske. Yu-Shiba-Rusinov states in phase-biased superconductor–quantum dot–superconductor junctions. *Phys. Rev. B*, 92(23):235422, 2015.
- [43] J. He, D. Pan, G. Yang, M. Liu, J. Ying, Z. Lyu, J. Fan, X. Jing, G. Liu, B. Lu, D. E. Liu, J. Zhao, L. Lu, and F. Qu. Nonequilibrium interplay between Andreev bound states and Kondo effect. *Phys. Rev. B*, 102(7):075121, 2020.
- [44] E. J. H. Lee, X. Jiang, M. Houzet, R. Aguado, C. M. Lieber, and S. De Franceschi. Spin-resolved Andreev levels and parity crossings in hybrid superconductor–semiconductor nanostructures. *Nature Nanotechnology*, 9(1):79–84, 2014.
- [45] A. M. Whiticar, A. Fornieri, A. Banerjee, A. C. C. Drachmann, S. Gronin, G. C. Gardner, T. Lindemann, M. J. Manfra, and C. M. Marcus. Zeeman-driven parity transitions in an Andreev quantum dot. *Phys. Rev. B*, 103(24):245308, 2021.

- [46] A. V. Rozhkov and D. P. Arovas. Josephson Coupling through a Magnetic Impurity. *Phys. Rev. Lett.*, 82(13):2788–2791, 1999.
- [47] E. Vecino, A. Martín-Rodero, and A. Levy Yeyati. Josephson current through a correlated quantum level: Andreev states and π junction behavior. *Phys. Rev. B*, 68(3):035105, 2003.
- [48] T. Meng, S. Florens, and P. Simon. Self-consistent description of Andreev bound states in Josephson quantum dot devices. *Phys. Rev. B*, 79(22):224521, 2009.
- [49] L. I. Glazman and K. A. Matveev. Resonant Josephson current through Kondo impurities in a tunnel barrier. *Soviet Journal of Experimental and Theoretical Physics Letters*, 49:659, 1989.
- [50] A. Oguri, Y. Tanaka, and A. C. Hewson. Quantum Phase Transition in a Minimal Model for the Kondo Effect in a Josephson Junction. *Journal of the Physical Society of Japan*, 73(9):2494–2504, 2004.
- [51] J. Bauer, A. Oguri, and A. C. Hewson. Spectral properties of locally correlated electrons in a Bardeen–Cooper–Schrieffer superconductor. *Journal of Physics: Condensed Matter*, 19(48):486211, 2007.
- [52] M.-S. Choi, M. Lee, K. Kang, and W. Belzig. Kondo effect and Josephson current through a quantum dot between two superconductors. *Phys. Rev. B*, 70(2):020502, 2004.
- [53] T. Domański, A. Donabidowicz, and K. I. Wysokiński. Meservey-Tedrow-Fulde effect in a quantum dot embedded between metallic and superconducting electrodes. *Phys. Rev. B*, 78(14):144515, 2008.
- [54] D. Futterer, J. Swiebodzinski, M. Governale, and J. König. Renormalization effects in interacting quantum dots coupled to superconducting leads. *Phys. Rev. B*, 87(1):014509, 2013.
- [55] B. A. Joyce. Molecular beam epitaxy. *Reports on Progress in Physics*, 48(12):1637–1697, 1985.
- [56] I. Vurgaftman, J. R. Meyer, and L. R. Ram-Mohan. Band parameters for III–V compound semiconductors and their alloys. *J. Appl. Phys.*, 89(11):5815–5875, 2001.

- [57] F. K. de Vries, T. Timmerman, V. P. Ostroukh, J. van Veen, A. J. A. Beukman, F. Qu, M. Wimmer, B.-M. Nguyen, A. A. Kiselev, W. Yi, M. Sokolich, M. J. Manfra, C. M. Marcus, and L. P. Kouwenhoven. h/e Superconducting Quantum Interference through Trivial Edge States in InAs. *Phys. Rev. Lett.*, 120(4):047702, 2018.
- [58] S. Mueller, C. Mittag, T. Tschirky, C. Charpentier, W. Wegscheider, K. Ensslin, and T. Ihn. Edge transport in InAs and InAs/GaSb quantum wells. *Phys. Rev. B*, 96(7):075406, 2017.
- [59] F. Nichele, H. J. Suominen, M. Kjaergaard, C. M. Marcus, E. Sajadi, J. A. Folk, F. Qu, A. J. A. Beukman, F. K. de Vries, J. van Veen, S. Nadj-Perge, L. P. Kouwenhoven, B.-M. Nguyen, A. A. Kiselev, W. Yi, M. Sokolich, M. J. Manfra, E. M. Spanton, and K. A. Moler. Edge transport in the trivial phase of InAs/GaSb. *New Journal of Physics*, 18(8):083005, 2016.
- [60] C. Thomas, A. T. Hatke, A. Tuaz, R. Kallaher, T. Wu, T. Wang, R. E. Diaz, G. C. Gardner, M. A. Capano, and M. J. Manfra. High-mobility InAs 2DEGs on GaSb substrates: A platform for mesoscopic quantum transport. *Physical Review Materials*, 2(10):104602, 2018.
- [61] S. Cabrini and S. Kawata, editors. *Nanofabrication Handbook*. CRC Press, Boca Raton, 2012.
- [62] L. Ren and B. Chen. Proximity effect in electron beam lithography. pages 579–582 vol.1, 2004.
- [63] M. A. Stevens-Kalceff and K. J. Levick. The assessment of microscopic charging effects induced by focused electron and ion beam irradiation of dielectrics. *Microscopy Research and Technique*, 70(3):195–204, 2007.
- [64] G. C. Ménard, G. L. R. Anselmetti, E. A. Martinez, D Puglia, F. K. Malinowski, J. S. Lee, S Choi, M. Pendharkar, C. J. Palmstrøm, K Flensberg, C. M. Marcus, L Casparis, and A. P. Higginbotham. Conductance-Matrix Symmetries of a Three-Terminal Hybrid Device. *Phys. Rev. Lett.*, 124(3):036802, 2020.
- [65] D. Puglia, E. A. Martinez, G. C. Ménard, A. Pöschl, S. Gronin, G. C. Gardner, R. Kallaher, M. J. Manfra, C. M. Marcus, A. P. Higginbotham, and L. Casparis. Closing of the induced gap in a hybrid superconductor-semiconductor nanowire. *Phys. Rev. B*, 103(23):235201, 2021.

- [66] H. J. Suominen, M. Kjaergaard, A. R. Hamilton, J. Shabani, C. J. Palmstrøm, C. M. Marcus, and F. Nichele. Zero-Energy Modes from Coalescing Andreev States in a Two-Dimensional Semiconductor-Superconductor Hybrid Platform. *Phys. Rev. Lett.*, 119(17):176805, 2017.
- [67] A. M. Lobos and S. Das Sarma. Tunneling transport in NSN Majorana junctions across the topological quantum phase transition. *New J. Phys.*, 17(6):065010, 2015.
- [68] T. Ö. Rosdahl, A. Vuik, M. Kjaergaard, and A. R. Akhmerov. Andreev rectifier: A nonlocal conductance signature of topological phase transitions. *Phys. Rev. B*, 97(4):045421, 2018.
- [69] Y. Takane and H. Ebisawa. Conductance Formula for Mesoscopic Systems with a Superconducting Segment. *J. Phys. Soc. Jpn.*, 61(5):1685–1690, 1992.
- [70] J. Danon, A. B. Hellenes, E. B. Hansen, L. Casparis, A. P. Higginbotham, and K. Flensberg. Nonlocal Conductance Spectroscopy of Andreev Bound States: Symmetry Relations and BCS Charges. *Phys. Rev. Lett.*, 124(3):036801, 2020.
- [71] R. Hess, H. F. Legg, D. Loss, and J. Klinovaja. Local and nonlocal quantum transport due to Andreev bound states in finite Rashba nanowires with superconducting and normal sections. *Phys. Rev. B*, 104(7):075405, 2021.
- [72] H. Pan, J. D. Sau, and S. Das Sarma. Three-terminal nonlocal conductance in Majorana nanowires: Distinguishing topological and trivial in realistic systems with disorder and inhomogeneous potential. *Phys. Rev. B*, 103(1):014513, 2021.
- [73] D. I. Pikulin, B. van Heck, T. Karzig, E. A. Martinez, B. Nijholt, T. Laeven, G. W. Winkler, J. D. Watson, S. Heedt, M. Temurhan, V. Svidenko, R. M. Lutchyn, M. Thomas, G. de Lange, L. Casparis, and C. Nayak. Protocol to identify a topological superconducting phase in a three-terminal device. [arXiv:2103.12217](https://arxiv.org/abs/2103.12217).
- [74] H. Zhang, D. E. Liu, M. Wimmer, and L. P. Kouwenhoven. Next steps of quantum transport in Majorana nanowire devices. *Nat. Commun.*, 10(1):5128, 2019.
- [75] L. Hofstetter, S. Csonka, A. Baumgartner, G. Fülöp, S. D’Hollosy, J. Nygård, and C. Schönenberger. Finite-Bias Cooper Pair Splitting. *Phys. Rev. Lett.*, 107(13):136801, 2011.
- [76] L. Hofstetter, S. Csonka, J. Nygård, and C. Schönenberger. Cooper pair splitter realized in a two-quantum-dot Y-junction. *Nature*, 461(7266):960–963, 2009.

- [77] Z. Scherübl, G. Fülöp, J. Gramich, A. Pályi, C. Schönenberger, J. Nygård, and S. Csonka. From Cooper pair splitting to the non-local spectroscopy of a Shiba state. 2021. arXiv:2108.12155 [cond-mat].
- [78] J. Schindele, A. Baumgartner, and C. Schönenberger. Near-Unity Cooper Pair Splitting Efficiency. *Phys. Rev. Lett.*, 109(15):157002, 2012.
- [79] J. Gramich, A. Baumgartner, and C. Schönenberger. Andreev bound states probed in three-terminal quantum dots. *Phys. Rev. B*, 96(19):195418, 2017.
- [80] A. Maiani, M. Geier, and K. Flensberg. Conductance matrix symmetries of multiterminal semiconductor-superconductor devices. *Phys. Rev. B*, 106(10):104516, 2022.
- [81] G. C. Ménard, F. K. Malinowski, D. Puglia, D. I. Pikulin, T. Karzig, B. Bauer, P. Krogstrup, and C. M. Marcus. Suppressing quasiparticle poisoning with a voltage-controlled filter. *Phys. Rev. B*, 100(16):165307, 2019.
- [82] W. Uilhoorn, J. G. Kroll, A. Bargerbos, S. D. Nabi, C.-K. Yang, P. Krogstrup, L. P. Kouwenhoven, A. Kou, and G. de Lange. Quasiparticle trapping by orbital effect in a hybrid superconducting-semiconducting circuit. arXiv: 2105.11038.
- [83] A. Pöschl, A. Danilenko, D. Sabonis, K. Kristjuhan, T. Lindemann, C. Thomas, M. J. Manfra, and C. M. Marcus. Nonlocal signatures of hybridization between quantum dot and Andreev bound states. *Phys. Rev. B*, 106(16):L161301, 2022.
- [84] R. V Mishmash, D. Aasen, A. P Higginbotham, and J. Alicea. Approaching a topological phase transition in Majorana nanowires. *Phys. Rev. B*, 93(24):245404, 2016.
- [85] A R Akhmerov, J P Dahlhaus, F Hassler, M. Wimmer, and C W J Beenakker. Quantized Conductance at the Majorana Phase Transition in a Disordered Superconducting Wire. *Phys. Rev. Lett.*, 106(5):057001, 2011.
- [86] M. P. Anantram and S. Datta. Current fluctuations in mesoscopic systems with Andreev scattering. *Phys. Rev. B*, 53(24):16390–16402, 1996.
- [87] A. Pöschl, A. Danilenko, D. Sabonis, K. Kristjuhan, T. Lindemann, C. Thomas, M. J. Manfra, and C. M. Marcus. Nonlocal conductance spectroscopy of Andreev bound states in gate-defined InAs/Al nanowires, 2022. arXiv:2204.02430 [cond-mat].
- [88] A. Melo, C.-X. Liu, P. Rožek, T. Ö. Rosdahl, and M. Wimmer. Conductance asymmetries in mesoscopic superconducting devices due to finite bias. *SciPost Phys.*, 10(2):037, 2021.

- [89] A. B. Hellenes. *Local and nonlocal differential conductance spectroscopy of Andreev bound states in three-terminal superconducting devices*. Master's thesis, University of Copenhagen, 2019.
- [90] Y. Liu, S. Vaitiekėnas, S. Martí-Sánchez, C. Koch, S. Hart, Z. Cui, T. Kanne, S. A. Khan, R. Tanta, S. Upadhyay, M. Espiñeira Cachaza, C. M. Marcus, J. Arbiol, K. A. Moler, and P. Krogstrup. Semiconductor–Ferromagnetic Insulator–Superconductor Nanowires: Stray Field and Exchange Field. *Nano Lett.*, 20(1):456–462, 2020.
- [91] F. Krizek, J. E. Sestoft, P. Aseev, S. Marti-Sanchez, S. Vaitiekėnas, L. Casparis, S. A. Khan, Y. Liu, T. Stankevič, A. M. Whiticar, A. Fursina, F. Boekhout, R. Koops, E. Uccelli, L. P. Kouwenhoven, C. M. Marcus, J. Arbiol, and P. Krogstrup. Field effect enhancement in buffered quantum nanowire networks. *Phys. Rev. Mater.*, 2(9):093401, 2018.
- [92] V. M. Pereira, C.-N. Wu, K. Höfer, A. Choa, C.-A. Knight, J. Swanson, C. Becker, A. C. Komarek, A. D. Rata, S. Rößler, S. Wirth, M. Guo, M. Hong, J. Kwo, L. H. Tjeng, and S. G. Altendorf. Challenges of Topological Insulator Research: Bi₂Te₃ Thin Films and Magnetic Heterostructures. *Phys. Status Solidi B*, 258(1):2000346, 2021.
- [93] L. Fu and C. L. Kane. Josephson current and noise at a superconductor/quantum-spin-Hall-insulator/superconductor junction. *Phys. Rev. B*, 79(16):161408, 2009.
- [94] X.-L. Qi, T. L. Hughes, and S.-C. Zhang. Chiral topological superconductor from the quantum Hall state. *Phys. Rev. B*, 82(18):184516, 2010.
- [95] R. S.K. Mong, D. J. Clarke, J. Alicea, N. H. Lindner, P. Fendley, C. Nayak, Y. Oreg, A. Stern, E. Berg, K. Shtengel, and M. P.A. Fisher. Universal Topological Quantum Computation from a Superconductor-Abelian Quantum Hall Heterostructure. *Phys. Rev. X*, 4(1):011036, 2014.
- [96] O. Lesser, G. Shavit, and Y. Oreg. Topological superconductivity in carbon nanotubes with a small magnetic flux. *Phys. Rev. Res.*, 2(2):023254, 2020.
- [97] J. D. Sau, R. M. Lutchyn, S. Tewari, and S. Das Sarma. Generic New Platform for Topological Quantum Computation Using Semiconductor Heterostructures. *Phys. Rev. Lett.*, 104(4):040502, 2010.
- [98] A. Cook and M. Franz. Majorana fermions in a topological-insulator nanowire proximity-coupled to an *s*-wave superconductor. *Phys. Rev. B*, 84(20):201105, 2011.

- [99] R. M. Lutchyn, E. P. A. M. Bakkers, L. P. Kouwenhoven, P. Krogstrup, C. M. Marcus, and Y. Oreg. Majorana zero modes in superconductor-semiconductor heterostructures. *Nat. Rev. Mat.*, 3(5):52–68, 2018.
- [100] D. J. Carrad, M. Bjergfelt, T. Kanne, M. Aagesen, F. Krizek, E. M. Fiordaliso, E. Johnson, J. Nygård, and T. Sand Jespersen. Shadow Epitaxy for In Situ Growth of Generic Semiconductor/Superconductor Hybrids. *Advanced Materials*, 32(23):1908411, 2020.
- [101] M. Kjaergaard, H. J. Suominen, M. P. Nowak, A. R. Akhmerov, J. Shabani, C. J. Palmstrøm, F. Nichele, and C. M. Marcus. Transparent Semiconductor-Superconductor Interface and Induced Gap in an Epitaxial Heterostructure Josephson Junction. *Phys. Rev. Appl.*, 7(3):034029, 2017.
- [102] E. C. T. O’Farrell, A. C. C. Drachmann, M. Hell, A. Fornieri, A. M. Whiticar, E. B. Hansen, S. Gronin, G. C. Gardner, C. Thomas, M. J. Manfra, K. Flensberg, C. M. Marcus, and F. Nichele. Hybridization of Subgap States in One-Dimensional Superconductor-Semiconductor Coulomb Islands. *Phys. Rev. Lett.*, 121(25):256803, 2018.
- [103] F. Nichele, A. C. C. Drachmann, A. M. Whiticar, E. C. T. O’Farrell, H. J. Suominen, A. Fornieri, T. Wang, G. C. Gardner, C. Thomas, A. T. Hatke, P. Krogstrup, M. J. Manfra, K. Flensberg, and C. M. Marcus. Scaling of Majorana Zero-Bias Conductance Peaks. *Phys. Rev. Lett.*, 119(13):136803, 2017.
- [104] A. M. Whiticar, A. Fornieri, E. C. T. O’Farrell, A. C. C. Drachmann, T. Wang, C. Thomas, S. Gronin, R. Kallaher, G. C. Gardner, M. J. Manfra, C. M. Marcus, and F. Nichele. Coherent transport through a Majorana island in an Aharonov–Bohm interferometer. *Nat. Commun.*, 11(1):3212, 2020.
- [105] W. Chang, V. E. Manucharyan, T. S. Jespersen, J. Nygård, and C. M. Marcus. Tunneling Spectroscopy of Quasiparticle Bound States in a Spinful Josephson Junction. *Phys. Rev. Lett.*, 110(21):217005, 2013.
- [106] A. Jellinggaard, K. Grove-Rasmussen, M. H. Madsen, and J. Nygård. Tuning Yu-Shiba-Rusinov states in a quantum dot. *Phys. Rev. B*, 94(6):064520, 2016.
- [107] E. J. H. Lee, X. Jiang, R. Žitko, R. Aguado, C. M. Lieber, and S. De Franceschi. Scaling of subgap excitations in a superconductor-semiconductor nanowire quantum dot. *Phys. Rev. B*, 95(18):180502, 2017.

- [108] J-D. Pillet, C. H. L. Quay, P. Morfin, C. Bena, A. Levy Yeyati, and P. Joyez. Andreev bound states in supercurrent-carrying carbon nanotubes revealed. *Nat. Phys.*, 6(12):965–969, 2010.
- [109] F. Nichele, E. Portolés, A. Fornieri, A. M. Whiticar, A. C. C. Drachmann, S. Gronin, T. Wang, G. C. Gardner, C. Thomas, A. T. Hatke, M. J. Manfra, and C. M. Marcus. Relating Andreev Bound States and Supercurrents in Hybrid Josephson Junctions. *Phys. Rev. Lett.*, 124(22):226801, 2020.
- [110] Y. Huang, H. Pan, C.-X. Liu, J. D. Sau, T. D. Stanescu, and S. Das Sarma. Metamorphosis of Andreev bound states into Majorana bound states in pristine nanowires. *Phys. Rev. B*, 98(14):144511, 2018.
- [111] M. Leijnse and K. Flensberg. Scheme to measure Majorana fermion lifetimes using a quantum dot. *Phys. Rev. B*, 84(14):140501, 2011.
- [112] K. Gharavi, D. Hoving, and J. Baugh. Readout of Majorana parity states using a quantum dot. *Phys. Rev. B*, 94(15):155417, 2016.
- [113] S. Hoffman, C. Schrade, J. Klinovaja, and D. Loss. Universal quantum computation with hybrid spin-Majorana qubits. *Phys. Rev. B*, 94(4):045316, 2016.
- [114] K. Flensberg. Non-Abelian Operations on Majorana Fermions via Single-Charge Control. *Phys. Rev. Lett.*, 106(9):090503, 2011.
- [115] S. Plugge, A. Rasmussen, R. Egger, and K. Flensberg. Majorana box qubits. *New Journal of Physics*, 19(1):012001, 2017.
- [116] D. J. Clarke. Experimentally accessible topological quality factor for wires with zero energy modes. *Phys. Rev. B*, 96(20):201109, 2017.
- [117] E. Prada, R. Aguado, and P. San-Jose. Measuring Majorana nonlocality and spin structure with a quantum dot. *Phys. Rev. B*, 96(8):085418, 2017.
- [118] M.-T. Deng, S. Vaitiekėnas, E. Prada, P. San-Jose, J. Nygård, P. Krogstrup, R. Aguado, and C. M. Marcus. Nonlocality of Majorana modes in hybrid nanowires. *Phys. Rev. B*, 98(8):085125, 2018.
- [119] F. Peñaranda, R. Aguado, P. San-Jose, and E. Prada. Quantifying wave-function overlaps in inhomogeneous Majorana nanowires. *Phys. Rev. B*, 98(23):235406, 2018.
- [120] A. Ptok, A. Kobińska, and T. Domański. Controlling the bound states in a quantum-dot hybrid nanowire. *Phys. Rev. B*, 96(19):195430, 2017.

- [121] T. D. Stanescu and S. Das Sarma. Building topological quantum circuits: Majorana nanowire junctions. *Phys. Rev. B*, 97(4):045410, 2018.
- [122] A. Grivnin, E. Bor, M. Heiblum, Y. Oreg, and H. Shtrikman. Concomitant opening of a bulk-gap with an emerging possible Majorana zero mode. *Nat. Commun.*, 10(1):1940, 2019.
- [123] G. L. R. Anselmetti, E. A. Martinez, G. C. Ménard, D. Puglia, F. K. Malinowski, J. S. Lee, S. Choi, M. Pendharkar, C. J. Palmstrøm, C. M. Marcus, L. Casparis, and A. P. Higginbotham. End-to-end correlated subgap states in hybrid nanowires. *Phys. Rev. B*, 100(20):205412, 2019.
- [124] P. Yu, J. Chen, M. Gomanko, G. Badawy, E. P. A. M. Bakkers, K. Zuo, V. Mourik, and S. M. Frolov. Non-Majorana states yield nearly quantized conductance in proximatized nanowires. *Nat. Phys.*, 17(4):482–488, 2021.
- [125] A. Vuik, B. Nijholt, A. Akhmerov, and M. Wimmer. Reproducing topological properties with quasi-Majorana states. *SciPost Phys.*, 7(5):061, 2019.
- [126] C.-X. Liu, J. D. Sau, T. D. Stanescu, and S. Das Sarma. Andreev bound states versus Majorana bound states in quantum dot-nanowire-superconductor hybrid structures: Trivial versus topological zero-bias conductance peaks. *Phys. Rev. B*, 96(7):075161, 2017.
- [127] M. Valentini, F. Peñaranda, A. Hofmann, M. Brauns, R. Hauschild, P. Krogstrup, P. San-Jose, E. Prada, R. Aguado, and G. Katsaros. Nontopological zero-bias peaks in full-shell nanowires induced by flux-tunable Andreev states. *Science*, 373(6550):82–88, 2021.
- [128] J. D. Liu, C.-X. and Sau and S. Das Sarma. Distinguishing topological Majorana bound states from trivial Andreev bound states: Proposed tests through differential tunneling conductance spectroscopy. *Phys. Rev. B*, 97(21):214502, 2018.
- [129] H. Pan and S. Das Sarma. Physical mechanisms for zero-bias conductance peaks in Majorana nanowires. *Phys. Rev. Res.*, 2(1):013377, 2020.
- [130] C. Jünger, A. Baumgartner, R. Delagrè, D. Chevallier, S. Lehmann, Malin Nilsson, K. A. Dick, C. Thelander, and C. Schönenberger. Spectroscopy of the superconducting proximity effect in nanowires using integrated quantum dots. *Commun. Phys.*, 2(1):76, 2019.

- [131] J. O'Connell Yuan, K. S. Wickramasinghe, W. M. Strickland, M. C. Dartailh, K. Sardashti, M. Hatefipour, and J. Shabani. Epitaxial superconductor-semiconductor two-dimensional systems for superconducting quantum circuits. *Journal of Vacuum Science & Technology A*, 39(3):033407, 2021.
- [132] A. Jellinggaard, K. Grove-Rasmussen, M. Hannibal Madsen, and J. Nygård. Tuning Yu-Shiba-Rusinov states in a quantum dot. *Phys. Rev. B*, 94(6):064520, 2016.
- [133] O. Kürtössy, Z. Scherübl, G. Fülöp, I. Endre Lukács, T. Kanne, J. Nygård, P. Makk, and S. Csonka. Andreev Molecule in Parallel InAs Nanowires. *Nano Lett.*, 21(19):7929–7937, 2021.
- [134] F. S. Thomas, M. Nilsson, C. Ciaccia, C. Jünger, F. Rossi, V. Zannier, L. Sorba, A. Baumgartner, and C. Schönenberger. Spectroscopy of the local density of states in nanowires using integrated quantum dots. *Phys. Rev. B*, 104:115415, 2021.
- [135] J. Gramich, A. Baumgartner, and C. Schönenberger. Subgap resonant quasiparticle transport in normal-superconductor quantum dot devices. *Appl. Phys. Lett.*, 108(17):172604, 2016.
- [136] R. Hanson, B. Witkamp, L. M. K. Vandersypen, L. H. Willems van Beveren, J. M. Elzerman, and L. P. Kouwenhoven. Zeeman energy and spin relaxation in a one-electron quantum dot. *Phys. Rev. Lett.*, 91:196802, 2003.
- [137] G. Wang, T. Dvir, N. van Loo, G. P. Mazur, S. Gazibegovic, G. Badawy, E. P. A. M. Bakkers, L. P. Kouwenhoven, and G. de Lange. Nonlocal measurement of quasiparticle charge and energy relaxation in proximitized semiconductor nanowires using quantum dots. *Phys. Rev. B*, 106(6):064503, 2022.
- [138] R. Meservey and P. M. Tedrow. Spin-polarized electron tunneling. *Physics Reports*, 238(4):173–243, 1994.
- [139] P. Recher, E. V. Sukhorukov, and D. Loss. Quantum dot as spin filter and spin memory. *Phys. Rev. Lett.*, 85:1962–1965, 2000.
- [140] R. Hanson, L. M. K. Vandersypen, L. H. Willems van Beveren, J. M. Elzerman, I. T. Vink, and L. P. Kouwenhoven. Semiconductor few-electron quantum dot operated as a bipolar spin filter. *Phys. Rev. B*, 70(24):241304, 2004.
- [141] P. Szumniak, D. Chevallier, D. Loss, and J. Klinovaja. Spin and charge signatures of topological superconductivity in Rashba nanowires. *Phys. Rev. B*, 96(4):041401, 2017.

- [142] D. Chevallier, P. Szumniak, S. Hoffman, D. Loss, and J. Klinovaja. Topological phase detection in Rashba nanowires with a quantum dot. *Phys. Rev. B*, 97(4):045404, 2018.
- [143] G. de Lange, B. van Heck, A. Bruno, D. J. van Woerkom, A. Geresdi, S. R. Plissard, E. P. A. M. Bakkers, A. R. Akhmerov, and L. DiC. Realization of microwave quantum circuits using hybrid superconducting-semiconducting nanowire josephson elements. *Phys. Rev. Lett.*, 115:127002, 2015.
- [144] T. W. Larsen, K. D. Petersson, F. Kuemmeth, T. S. Jespersen, P. Krogstrup, J. Nygård, and C. M. Marcus. Semiconductor-nanowire-based superconducting qubit. *Phys. Rev. Lett.*, 115:127001, 2015.
- [145] L. Casparis, M. R. Connolly, M. Kjaergaard, N. J. Pearson, A. Kringhøj, T. W. Larsen, F. Kuemmeth, T. Wang, C. Thomas, S. Gronin, G. C. Gardner, M. J. Manfra, C. M. Marcus, and K. D. Petersson. Superconducting gatemon qubit based on a proximitized two-dimensional electron gas. *Nature Nanotechnology*, 13(10):915–919, 2018.
- [146] A. Kringhøj, T. W. Larsen, B. van Heck, D. Sabonis, O. Erlandsson, I. Petkovic, D. I. Pikulin, P. Krogstrup, K. D. Petersson, and C. M. Marcus. Controlled dc monitoring of a superconducting qubit. *Phys. Rev. Lett.*, 124:056801, 2020.
- [147] A. Kringhøj, B. van Heck, T. W. Larsen, O. Erlandsson, D. Sabonis, P. Krogstrup, L. Casparis, K. D. Petersson, and C. M. Marcus. Suppressed charge dispersion via resonant tunneling in a single-channel transmon. *Phys. Rev. Lett.*, 124:246803, 2020.
- [148] A. Bargerbos, W. Uilhoorn, C.-K. Yang, P. Krogstrup, L. P. Kouwenhoven, G. de Lange, B. van Heck, and A. Kou. Observation of vanishing charge dispersion of a nearly open superconducting island. *Phys. Rev. Lett.*, 124:246802, 2020.
- [149] M. Hays, G. de Lange, K. Serniak, D. J. van Woerkom, D. Bouman, P. Krogstrup, J. Nygård, A. Geresdi, and M. H. Devoret. Direct microwave measurement of andreev-bound-state dynamics in a semiconductor-nanowire josephson junction. *Phys. Rev. Lett.*, 121:047001, 2018.
- [150] L. Tosi, C. Metzger, M. F. Goffman, C. Urbina, H. Pothier, Sunghun Park, A. Levy Yeyati, J. Nygård, and P. Krogstrup. Spin-orbit splitting of andreev states revealed by microwave spectroscopy. *Phys. Rev. X*, 9:011010, 2019.
- [151] M. Hays, V. Fatemi, D. Bouman, J. Cerrillo, S. Diamond, K. Serniak, T. Connolly, P. Krogstrup, J. Nygård, A. Levy Yeyati, A. Geresdi, and M. H. Devoret. Coherent manipulation of an andreev spin qubit. *Science*, 373(6553):430–433, 2021.

- [152] F. J. Matute-Cañadas, C. Metzger, Sunghun Park, L. Tosi, P. Krogstrup, J. Nygård, M. F. Goffman, C. Urbina, H. Pothier, and A. Levy Yeyati. Signatures of interactions in the andreev spectrum of nanowire josephson junctions. *Phys. Rev. Lett.*, 128:197702, 2022.
- [153] T. W. Larsen, M. E. Gershenson, L. Casparis, A. Kringhøj, N. J. Pearson, R. P. G. McNeil, F. Kuemmeth, P. Krogstrup, K. D. Petersson, and C. M. Marcus. Parity-Protected Superconductor-Semiconductor Qubit. *Phys. Rev. Lett.*, 125(5):056801, 2020.
- [154] D. Sabonis, O. Erlandsson, A. Kringhøj, B. van Heck, T. W. Larsen, I. Petkovic, P. Krogstrup, K. D. Petersson, and C. M. Marcus. Destructive little-parks effect in a full-shell nanowire-based transmon. *Phys. Rev. Lett.*, 125:156804, 2020.
- [155] L. Casparis, N. J. Pearson, A. Kringhøj, T. W. Larsen, F. Kuemmeth, J. Nygård, P. Krogstrup, K. D. Petersson, and C. M. Marcus. Voltage-controlled superconducting quantum bus. *Phys. Rev. B*, 99:085434, 2019.
- [156] A. Kringhøj, L. Casparis, M. Hell, T. W. Larsen, F. Kuemmeth, M. Leijnse, K. Flensberg, P. Krogstrup, J. Nygård, K. D. Petersson, and C. M. Marcus. Anharmonicity of a superconducting qubit with a few-mode Josephson junction. *Phys. Rev. B*, 97(6):060508, 2018.
- [157] L. J. Splitthoff, A. Bargerbos, L. Grünhaupt, M. Pita-Vidal, J. J. Wesdorp, Y. Liu, An. Kou, C. Kraglund Andersen, and B. van Heck. Gate-tunable kinetic inductance in proximitized nanowires. 2022. arXiv: 2202.08729.
- [158] G. W. Winkler, A. E. Antipov, B. van Heck, A. A. Soluyanov, L. I. Glazman, M. Wimmer, and R. M. Lutchyn. Unified numerical approach to topological semiconductor-superconductor heterostructures. *Phys. Rev. B*, 99:245408, 2019.
- [159] A. Kringhøj, T. W. Larsen, O. Erlandsson, W. Uilhoorn, J.G. Kroll, M. Hesselberg, R.P.G. McNeil, P. Krogstrup, L. Casparis, C.M. Marcus, and K.D. Petersson. Magnetic-field-compatible superconducting transmon qubit. *Phys. Rev. Appl.*, 15:054001, 2021.
- [160] K. Zuo, V. Mourik, D. B. Szombati, B. Nijholt, D. J. van Woerkom, A. Geresdi, J. Chen, V. P. Ostroukh, A. R. Akhmerov, S. R. Plissard, D. Car, E. P. A. M. Bakkers, D. I. Pikulin, L. P. Kouwenhoven, and S. M. Frolov. Supercurrent interference in few-mode nanowire josephson junctions. *Phys. Rev. Lett.*, 119:187704, 2017.

- [161] Ö Gül, H. Y. Günel, H. Lüth, T. Rieger, T. Wenz, F. Haas, M. Lepsa, G. Panaitov, D. Grützmacher, and Th. Schäpers. Giant magnetoconductance oscillations in hybrid superconductor–semiconductor core/shell nanowire devices. *Nano Letters*, 14(11):6269–6274, 2014.
- [162] C. W. J. Beenakker. Universal limit of critical-current fluctuations in mesoscopic josephson junctions. *Phys. Rev. Lett.*, 67:3836–3839, 1991.
- [163] H. Takayanagi, J. B. Hansen, and J. Nitta. Mesoscopic fluctuations of the critical current in a superconductor—normal-conductor—superconductor. *Phys. Rev. Lett.*, 74:166–169, 1995.
- [164] Y.-J. Doh, J. Dam, A. Roest, E. Bakkers, L. Kouwenhoven, and S. Franceschi. Tunable supercurrent through semiconductor nws. *Science (New York, N.Y.)*, 309:272–5, 2005.
- [165] Th Schäpers, A. Kaluza, K. Neurohr, J. Malindretos, G. Crecelius, A. Hart, Hilde Hardtdegen, and Hans Lüth. Josephson effect in nb/two-dimensional electron gas structures using a pseudomorphic $\text{In}_x\text{Ga}_{1-x}\text{As}/\text{InP}$ heterostructure. *Appl. Phys. Lett.*, 71:3575–3577, 1997.
- [166] S. Vaitiekėnas, G. W. Winkler, B. van Heck, T. Karzig, M.-T. Deng, K. Flensberg, L. I. Glazman, C. Nayak, P. Krogstrup, R. M. Lutchyn, and C. M. Marcus. Flux-induced topological superconductivity in full-shell nanowires. *Science*, 367(6485), 2020.
- [167] A. Kringhøj, G. W. Winkler, T. W. Larsen, D. Sabonis, O. Erlandsson, P. Krogstrup, B. van Heck, K. D. Petersson, and C. M. Marcus. Andreev modes from phase winding in a full-shell nanowire-based transmon. *Phys. Rev. Lett.*, 126:047701, 2021.
- [168] J. Shen, G. W. Winkler, F. Borsoi, S. Heedt, V. Levajac, J.-Y. Wang, D. van Driel, D. Bouman, S. Gazibegovic, R. L. M. Op Het Veld, D. Car, J. A. Logan, M. Pendharkar, C. J. Palmstrøm, E. P. A. M. Bakkers, L. P. Kouwenhoven, and B. van Heck. Full parity phase diagram of a proximitized nanowire island. *Phys. Rev. B*, 104:045422, 2021.
- [169] C. W. Groth, M. Wimmer, A. R. Akhmerov, and X. Waintal. Kwant: a software package for quantum transport. *New J. Phys.*, 16(6):063065, 2014. The code is publicly available at <https://kwant-project.org/>.
- [170] V. P. Ostroukh, B. Baxevanis, A. R. Akhmerov, and C. W. J. Beenakker. Two-dimensional josephson vortex lattice and anomalously slow decay of the fraunhofer

oscillations in a ballistic sns junction with a warped fermi surface. *Phys. Rev. B*, 94:094514, 2016.

- [171] COMSOL, Inc. [www.comsol.com].
- [172] B.L. Altshuler and B. Spivak. Mesoscopic fluctuations in a superconductor-normal metal-superconductor junction. *Zh. Eksp. Teor. Fiz.*, 92, 1987.
- [173] D. van Woerkom, A. Proutski, B. van Heck, D. Bouman, J. Väyrynen, L. Glazman, P. Krogstrup, J. Nygård, L. Kouwenhoven, and A. Geresdi. Microwave spectroscopy of spinful andreev bound states in ballistic semiconductor josephson junctions. *Nat. Phys.*, 13, 2016.
- [174] E. Spanton, M. Deng, S. Vaitiekenas, P. Krogstrup, J. Nygård, C. Marcus, and K. Moler. Current-phase relations of few-mode inas nanowire josephson junctions. *Nat. Phys.*, 13, 2017.
- [175] Y. Gunel, I. Batov, H. Hardtdegen, K. Sladek, A. Winden, K. Weis, G. Panaitov, D. Gruetzmacher, and Th Schaebers. Supercurrent in nb/inas-nanowire/nb josephson junctions. *J. Appl. Phys.*, 112, 2012.